SURFACE-PENETRATING RADAR FOR MARS EXPLORATION

by

Carl Leuschen

B. Sc. (With Highest Distinction) Electrical Engineering, 1995

M. Sc. (With Honors) Electrical Engineering, 1997

The University of Kansas, 2001

Submitted to the Department of Electrical Engineering and Computer Science and the Faculty of the Graduate School of the University of Kansas in partial fulfillment of the requirements for the degree of Doctor of Philosophy.

Dissertation Committee:

_____
Prasad Gogineni: Chairperson

_____
Chris Allen

_____
Glenn Prescott

_____
Soon Sam Kim

_____
Steve Clifford

Date of Defense: November 13, 2001

ACKNOWLEDGEMENTS

I would like to thank my Ph.D. advisor, Dr. Prasad Gogineni, for his guidance throughout these past few years. He has always been willing to take the time to help me and offer advise when needed. He has been instrumental in helping me choose a path though my research and future career. I would also like to thank my undergraduate and M.S. advisor, Dr. Richard Plumb, for sparking an interest in remote sensing and convincing me to continue with my Ph.D.

I would like to thank Nathan Goodman and Pannir Kanagaratnam for their friendship. Nathan has been a good friend through undergraduate and graduate school, and he has made working at The Radar Systems and Remote Sensing Laboratory an enjoyable experience. Pannir has always gone out of his way to help, especially with the experiments in Alaska.

I thank my parents for their love and support throughout my life. The have taught me about life and have always encouraged my on my endeavors.

Finally, I would like to thank my wife, Marci, who has helped to ease some of the burdens and pressures of the Ph.D. She has always been there to offer reassurance during the difficult times and to celebrate my successes. I appreciate the sacrifices she has made so I could attain this degree.

TABLE OF CONTENTS

LIST OF FIGURES

LIST OF TABLES

LIST OF SYMBOLS

ϕ: porosity (% volume)

K: porosity decay rate

h: surface height

σ_h: r.m.s. surface height

ρ: distance between two surface points

l: correlation length

C_s: correlation coefficient

σ_s: r.m.s. surface slope

α_s: surface slope in the x direction

β_s: surface slope in the y direction

ε: permittivity

ε_m: relative permittivity of a soil mixture

ε_a: relative permittivity of air

ε_w: relative permittivity of water phase

ε_s: relative permittivity of solid soil

μ: permeability

s: saturation (% volume)

C: iron concentration

δ: loss angle

ε_{st}: static, low-frequency permittivity

ε_∞: infinite, high-frequency permittivity

ω: angular frequency

τ_r: relaxation time

σ_e: electrical conductivity

ε_d: permittivity of scattering debris

ε_b: background permittivity

ε_{eff}: effective scattering permittivity

f_v: volume fraction

k: wavenumber

a: radius of scattering debris

λ: wavelength

f: frequency

P_r: receive power

P_t: transmit power

G: antenna gain

σ_{cs}: target cross section

R: range

σ^0: scattering coefficient

Γ: reflection coefficient

R_0: height of the radar

E: electric field vector

H: magnetic field vector

η: intrinsic impedance

Z: characteristic impedance

T: transmit waveform

U: receive waveform

α: attenuation constant

v: velocity of propagation

ϑ: incident angle

c: velocity of free space

t: time

t_0: propagation delay of the surface reflection

t_p: time referenced to the surface reflection

A: illuminated area

x: radius of illuminated area ring

Δx: width of illuminated area ring

Δz: spatial pulse width

s_t: transmit signal

s_r: receive signal

f_0: start frequency

κ: sweep rate

f_T: transmit frequency

p: reflection profile

A_n: amplitude of the nth reflection

τ_n: time delay of the nth reflection

φ_n: phase of the nth reflection

S_w: windowed spectrum

f_c: center frequency

BW: bandwidth

ABSTRACT

Over the past few years, the interest in exploring Mars has grown, with several missions in the planning stages for the next decade. One motivating theme is the potential of discovering substantial subsurface aqueous reservoirs. This discussion outlines the development of a lightweight, low-power surface-penetrating radar system intended for the subsurface exploration of Mars. The objective addressed is to probe the Martian subsurface up to a depth of a several hundreds of meters with a resolution on the order of tens of meters. The primary use of the system would be on a lander-/rover-based mission in which a lateral traverse could be made; however, we are also considering an orbital system.

To accurately asses the performance of a ground-penetrating radar system on Mars, a first-order model of the subsurface composition and stratigraphy was developed. This model includes simulation parameters governing signal attenuation and scattering coefficients. From these parameters, further investigation and simulations help to offer a broader understanding of what properties can and cannot be detected by a specific radar system, help to redefine the project objectives to match what is physically possible, and set a performance baseline for the system.

In addition to the simulation results, a prototype system was constructed using connectorized components and evaluation boards. The prototype system serves as a test bed to investigate antenna subsystems, modulation schemes, and radar responses over segregated bodies of ice and water. Results from experiments conducted in Lawrence, Kansas, and Fairbanks, Alaska, will be presented. Based on these results, an optimal system for the exploration of Mars' subsurface is proposed.

CHAPTER 1

WATER ON MARS

1-1 INTRODUCTION

Over the past few years, the interest in exploring Mars has grown and, with the recent success of the Mars Pathfinder mission and the Sojourner Rover, the notion of continued exploration has become more exciting. Over the next decade, NASA plans on sending several orbiters/landers to Mars for supporting scientific investigations. A variety of instrumentation including surface-penetrating radars are being considered for in situ exploration with landers and rovers. This work outlines the simulation and development of a lightweight, low-power, surface-penetrating radar (SPR) intended for Mars subsurface exploration.

Radars operating in the high-frequency (HF) and very-high-frequency (VHF) regions of the electromagnetic spectrum may be useful in acquiring information on the surface and subsurface of Mars. Radar provides a means of probing into the subsurface without digging and also allows measurements to be made along the surface for detecting

lateral variations. Due to these benefits, orbital- and lander/rover-based radars could provide valuable information for the exploration of Mars. In conjunction with other geological information, radar reflectivity measurements could be used to detect and distinguish between subsurface deposits of ice or water.

The main objective of this dissertation is to simulate and design a prototype radar that is capable of probing the Martian subsurface to a maximum depth of a kilometer with tens-of-meters resolution. The information acquired by the system could be used to characterize the subsurface with an ultimate goal of detecting water either in liquid or frozen form. The primary usage of the system would be on a lander/rover-based mission in which a lateral traverse could be made. Additional geologic applications include subsurface characterization, determining soil properties at radio frequencies, and three-dimensional stratigraphy mapping. Also, from a signal-processing standpoint, the research is aimed at developing algorithms for reducing both internal and surface clutter of swept/stepped-frequency surface-penetrating radars appearing as sidelobes. Reducing the range sidelobes of these strong clutter signals is an essential prerequisite for improving swept/stepped-frequency radar performance in the characterization of subsurface layers.

The dissertation is divided into six chapters. This first chapter includes the introduction and provides a basic background study of the exploration of Mars with an emphasis on the existence of water. Next, radar simulations are presented in Chapter 2. In this chapter, extensive simulations are performed using a wide range of possible scenarios of the planet's stratigraphy, and radar configurations. The purpose of these simulations is to provide some insight into what a SPR system is capable of detecting and help optimize radar parameters for subsurface sounding of Mars. This section will also identify any limitations of a radar system and help modify the stated goals. Based on the results of these simulations, a prototype system is presented in Chapter 3. The system is constructed using off-the-shelf components and evaluation boards to demonstrate the theory of operation and test its performance. The system also serves as a testbed to verify the simulations and evaluate different antenna configurations for the lander/rover.

Chapter 4 discusses a signal processing algorithm and how SPR data can be interpreted. This chapter focuses on reducing sidelobe interference and extracting reflectivity information from band-limited signals. Chapter 5 outlines the experiments that were conducted in Lawrence, Kansas, and in Fairbanks, Alaska. Data from these experiments are used to recommend an optimal radar configuration including its mode of operation, frequency range, transmit power, and signal processing algorithms. Finally, conclusions and future modification are presented in Chapter 6.

1-2 EXPLORATION OF MARS

Over the last few centuries humans have been exploring Mars. The first historical study of Mars is credited to two sketches by Francisco Fontana that were rendered from his telescopic observations in 1638 [1]. From then on, others have gathered information on this planet using telescopes, orbiting satellites, and more recently instrumented landers. Mars exploration can be broken down into three commonly accepted periods. The "First Period of Exploration" continued until about 1830 when the "Geographic Period" began. During this period, the main concern was to produce quality maps of Mars. The next "Modern Era" of exploration started around 1877 with a map by Giovanni Virginio Schiaparelli in which he described the popular "canali" or channels and consequently reinforced the idea that Mars may contain a significant amount of water. In 1964, NASA began exploring Mars with Mariner 4 and continued with missions as shown in Table 1-1. Several missions dedicated to Mars observation are scheduled to be launched over the next few years.

Table 1-1. NASA History of Mars Exploration

Year	Mission
1999	Mars Polar Lander: attempt
1999	Deep Space 2: attempt
1998	Mars Climate Orbiter: attempt
1996	Mars Global Surveyor
1996	Mars Pathfinder
1992	Mars Observer
1975	Viking I and II
1971	Mariner 9
1969	Mariner 7
1969	Mariner 6
1964	Mariner 4

1-3 IMPORTANCE OF WATER ON MARS

An area of particular interest to the scientific community is the existence of water or ice on Mars. Mars is reported to have undergone considerable geological changes over its history, and water could have played an important role in these changes [2,3]. "Some researchers suggest that early Mars was warm and wet, and conditions changed early to the frigid conditions of today [3]." The presence of water is important because of three major reasons. First, it could provide a better understanding of the geological history of the planet. Second, water is the key to life on Earth; on Mars, it could indicate the possibility of past life. Finally, any accessible reservoirs could provide crucial resources for future manned exploration.

According to the Mars Exploration Program Analysis Group (MEPAG) [4], the major goals associated with Mars exploration include determining "if life ever arose on Mars, the climate on Mars, and the evolution of the surface and interior of Mars." Many of the objectives and investigations associated with these goals focus on the detection of water in any form within the planet's subsurface. More specifically, this includes mapping the three-dimensional distribution of water in all its forms at depths up to 5 km at resolutions of about 10 m for the near surface (<100m) and 100 m at greater depth (<5km). Radar systems will play an important role in the completion of these objectives,

and both orbital- and lander/rover-based systems will need to be used in conjunction to obtain both global coverage along with high-resolution stratigraphy mapping.

1-4 INDICATORS AND LOCATIONS OF WATER ON MARS

Observations of Mars' surface indicate features similar to those created by ice and water erosion, leading to a belief that at one point in time Mars may have had rivers, lakes, glaciers, and possibly even an atmosphere comparable to that found on the Earth. There is strong evidence that Mars had and still may contain a significant amount of water within its surface in the form of permafrost, ice, or liquid water. A few of these indicators are listed below.

1-4-1 CHANNELS

The most obvious indicator for the past existence of water on Mars' surface are channels. Figure 1-1 shows one of these channels that exists in the Nanedi Valles system imaged by the Mars Orbiter Camera (MOC) aboard the Mars Global Surveyor (MGS) [5]. Using the scale in the lower right, the width of the valley is approximately 2.5 km. Upon closer inspection, there is a small channel shown by the arrow in the upper right of the image. These formations indicate erosion that may have been caused by a sustained flow of water. Water that once flowed in this channel may have carved out this canyon over many years.

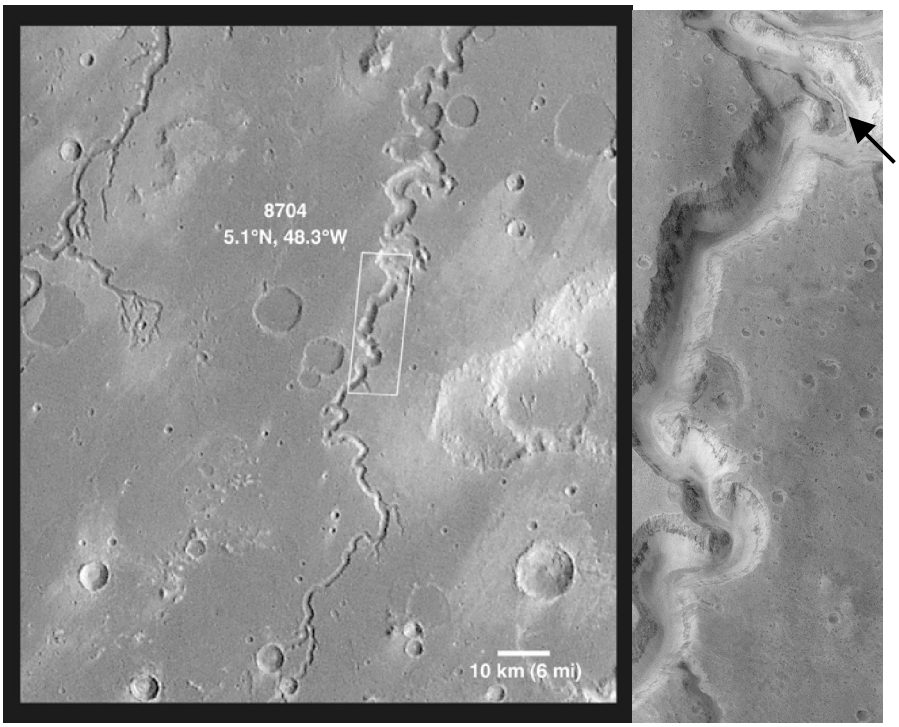

Figure 1-1. Valley with a small channel shown by the arrow in the upper right.

1-4-2 RAMPART CRATERS

From observation of rampart craters on Mars, both the presence and depth of water can be inferred from the size and features of the crater ejecta. More specifically, these ejecta show a redistribution of fluid or mud rather than solid rock as shown in Figure 1-2. A reason for this type of ejecta is the existence of water in the subsurface. Not all craters on Mars display this type of fluidized ejecta. In fact, only craters exceeding a certain diameter at a given location will show these characteristics. This crater size, called the onset diameter, is in some sense an indicator of the depth to which an impact event must excavate soil to reach significant quantities of ice [6]. By analyzing this onset diameter, the depth of ice on Mars can be estimated to range from a 100 m at around 50° latitude to 300 - 400 m at the equator.

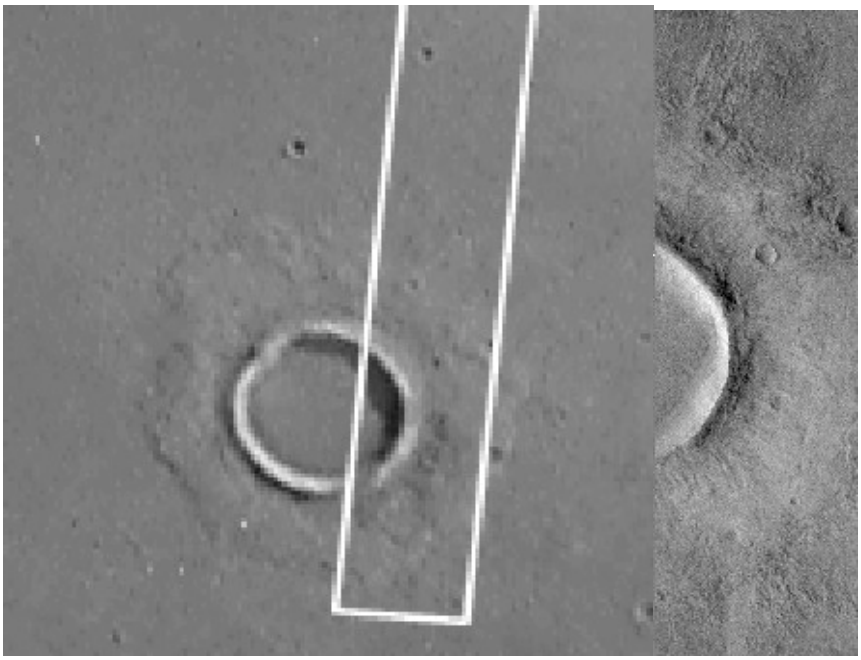

Figure 1-2. Example of a rampart crater showing fluidized ejecta.

1-4-3 Debris Flows (Aprons), Terrain Softening and Other Indicators

Other geological indicators for the existence of water on Mars are debris flows and terrain softening. Soil cemented by ice is a viscous material and experiences a slow creep over time. The result of this motion becomes apparent in areas having steep terrain such as valleys, craters, and mountains. Several locations on Mars show debris aprons as a result of soil flows where normally jagged terrain becomes "soft." These geological indicators strongly support the notion that ice exists within the subsurface of the planet. Other indicators for water on Mars include chaotic terrain, thermokarst, patterned ground, pseudocraters, pingos, table mountains, and curvilinear ridges [5].

1-5 Possibilities for Carbon Dioxide

There are other arguments that the formation of these geological feature may not be caused by water at all. One particular "White Mars" [7] model suggests that these

features are a result of carbon dioxide (CO_2). Liquid CO_2 is speculated to exist within the subsurface of the planet, and gas outbursts generated by this CO_2 are responsible for the features present today. If correct, the channels, rampart craters, and gullies thought to have been caused by water and ice flows are actually a result of debris flows supported by rapid expansion of liquid CO_2 into a gas state. This point is presented as a reminder that the existence of water within the subsurface of Mars has not been proven and reinforces the importance of a radar or other remote sensing technique both to detect and distinguish water from the surrounding materials.

1-6 SURFACE-PENETRATING RADAR ON MARS

For the development of a surface-penetrating radar for Mars, new technologies and concepts must be explored to reduce system size, mass, and power, while still providing adequate loop sensitivity, dynamic range, and range resolution. Innovations in antenna design, frequency modulation, and signal processing are essential for implementing a compact and power-efficient system. Radar performance is controlled by a number of factors including geophysical properties and system characteristics such as frequency, bandwidth, modulation, and antenna geometry. To help identify important trade-offs, the specific benefits and disadvantages of possible configurations will need to be evaluated in conjunction with the stated goals and possible scientific return of a SPR mission.

Of all the system parameters, probably the most important is the choice of the operating frequency and system bandwidth, which are related to the depth of penetration and resolution. In turn, the operating frequency will determine the antenna size and geometry. In general, a low-frequency system will provide deeper penetration at the cost of system bandwidth and range resolution, whereas a high-frequency system will provide increased bandwidth and finer resolution with shallower penetration. A wideband system that includes both low and high frequencies is desirable to sound the upper part of the subsurface with fine resolution and the lower part with coarse resolution. However,

implementation of such a system is difficult because of limitations on timing and modulation schemes and the size of antenna that can be accommodated on lander/rover.

1-6-1 LOW-FREQUENCY SYSTEM

The geological features detectable by a low-frequency system with a frequency range extending from a few megahertz to tens of megahertz will include large segregated formations found at locations ranging from the surface to a depth of a few hundred of meters to a kilometer. Smaller scale stratigraphy will not be sufficiently resolved for detection due to the coarse resolution associated with the low bandwidth of the system. This type of system is most likely to provide a means of acquiring a direct reflection of a body of ice or water. However, unambiguous detection of water using the reflectivity data alone may not be possible. In other words, even though a formation could generate a reflection that is detected by the system, showing that the reflection is due to water or ice may not be feasible. Radar reflectivity data in conjunction with other geophysical information, such as seismic or low-frequency EM methods, could provide a strong indication for the presence or absence of water and ice. A low-frequency radar will show the large scale stratigraphy and provide an indication of past geological events.

Due to the increased antenna size, a very-low-frequency system, on the order of a few megahertz, will likely be restricted to an orbital mission. This type of radar would provide low resolution and global coverage. A radar operating from a few tens of megahertz to a few hundreds of megahertz would be possible on a lander- or rover-based mission although the antenna size would still be large and may hinder the motion of the rover.

1-6-2 HIGH-FREQUENCY SYSTEM

The geological features detectable by a high-frequency system operating from hundreds of megahertz to a few gigahertz will be those found within a few tens of meters of the near surface. These features include fine-scale resurfacing from more recent geological events and subsurface structures such as buried debris or even a near-surface ice lens, which is unlikely to exist. Additionally, through data collection over a lateral traverse, a high-frequency system may be able to detect formations indicating the possibility of ice or water at greater depth, although direct detection of a deeper formation of ice or water is unlikely. Due to the small antenna size, a high-frequency system is well suited for a rover with which a long traverse could be made.

CHAPTER 2

RADAR SIMULATIONS

2-1 INTRODUCTION

The primary objective of the research described in this dissertation is the design and development of a surface-penetrating radar for characterization and discrimination of various types of ice and soils. The system is intended for incorporation into a future mission to Mars. The results could provide valuable information on areas favorable for the existence of water and help narrow the possible locations for further exploration. The first step in designing such a system is simulating responses expected from geophysical models based on data from previous missions to Mars and Earth analogues.

Figure 2-1 shows a block-level implementation of a simulator developed as a part of this work. The two boxes on the left-hand side of the simulation flow chart

represent all the inputs including the geophysical model and system parameters. The geophysical model describes the properties of the surface and subsurface stratigraphy units including thickness, lithology, interface roughness, and volume debris (rocks). The radar parameters describe the frequency of operation, bandwidth, pulse shape, modulation, transmit power, and antenna properties. The electrical properties, complex permittivity and permeability, of the stratigraphical layers are calculated from the lithology, frequency band, and volume debris using empirical formulas. Next, the SPR profile, wavenumber as a function of depth and frequency, is generated from the electrical properties appropriate to the modeled stratigraphy. Finally, the profile along with additional system and surface information are input to the simulator and a radar response is generated.

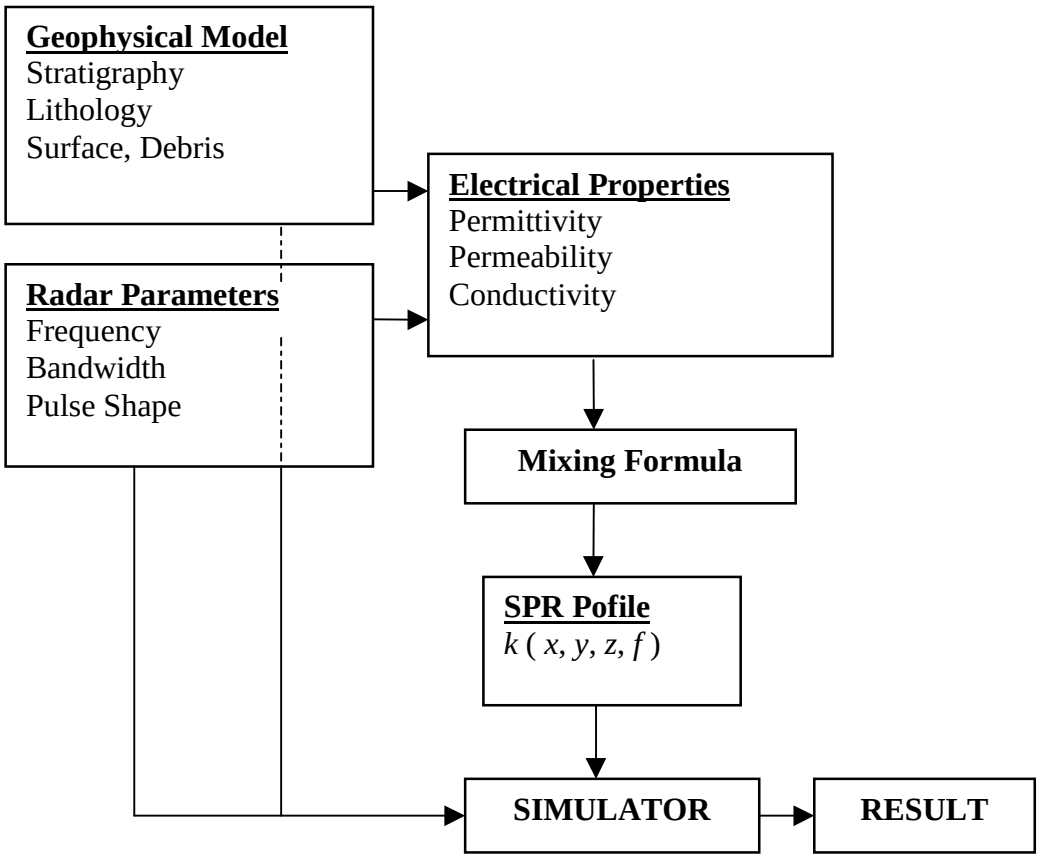

Figure 2-1. Simulation flow chart.

There are a variety of simulation algorithms that are appropriate for generating a surface-penetrating radar response, and the specific method of choice depends on the geophysical model, radar parameters, and degree of accuracy desired. For a basic first-order simulation, a simple plane-wave specular response is adequate. For more accurate results, random surfaces with scattering at off-nadir angles of incidence should be included. Even more accurate simulations can be obtained using more complicated methods, such as the finite-difference time-domain (FDTD) method, at the cost of computation time. Presented later in Chapter 5, the FDTD method will be used to simulate responses for a near-surface experiment when spherical wave propagation is a concern. However, since the main goal of the simulations presented in this chapter is to investigate the basic properties that influence the radar response, using a plane-wave model with the incorporation of rough surface effects will be sufficient.

The next few sections of this chapter describe the geophysical model, electrical properties, and mixing formulas. Finally, the simulators are described and specific models of different geological areas are considered.

2-2 GEOPHYSICAL MODEL

To accurately simulate the response of a surface-penetrating radar on Mars, a geophysical model of the subsurface composition and stratigraphy must be developed to obtain electrical parameters such as signal attenuation, wave velocity, and reflection coefficients. From these parameters, further investigation and simulations will provide a broader understanding of what properties can and cannot be detected by a specific radar system. This will help to define the baseline performance of a radar and its limitations.

2-2-1 GENERAL STRATIGRAPHY

"Stratigraphy forms the framework of historical geology [8]." It is the relationship of the rocks and soils of the terrain and the subsurface. From a radar perspective, the idea of stratigraphy changes from the distributions of the physical rocks and soils to the distribution of their electrical properties, both permittivity and permeability. The upper surface of Mars is largely a result of resurfacing by volcanic, fluvial, aeolian, periglacial, and impact processes. It is estimated that this layer of displaced materials covers the planet with a 2 km blanket [6]. On a large scale, the stratigraphy of Mars can be interpreted as a weathered soil with an exponentially decaying porosity given by the equation

$$\Phi(z) = \Phi(0)e^{-z/K} \tag{2-1}$$

where $\Phi(0)$ is the porosity at the surface and K is the rate of decay.

Using lunar data as reference, values for the porosity at the surface range from 20 to 50 %, and the decay constant is about 2.8. Within the pores of this soil could lie a significant amount of water as ice near the surface and as liquid water at greater depths. On a smaller scale, "it is likely that this ejecta (resurfaced) layer is discontinuously interbedded with volcanic flows, weathering products, and sedimentary deposits, all overlying a heavily fractured basement [6]." Figure 2-2 shows a model for the Martian stratigraphy including the global distributions of water and ice along with a more detailed local representation of subsurface layering.

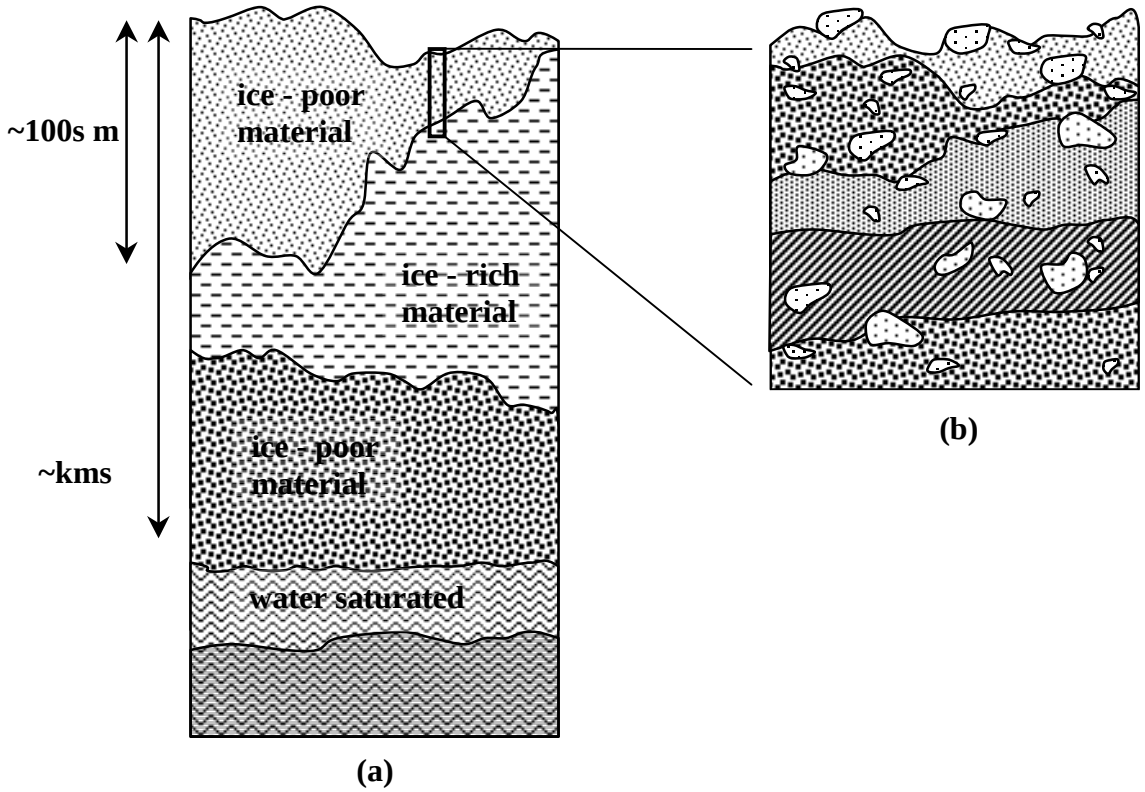

Figure 2-2. A model for the Martian stratigraphy: (a) global and (b) local showing fine-scale layering.

2-2-1-1 IONOSPHERE

In addition to the subsurface layering, the atmosphere of Mars can also be included as a simulation layer for an orbital system. At lower frequencies, below 1 MHz during the night and below 3.5 MHz during the day, radio waves may experience significant loss and dispersion as they propagate through the ionosphere. In fact, these frequency indicate a lower bound for orbital-based surface-penetrating radar. At frequencies above these limits, the effects should be less significant but may still be present. The impact of dispersion though the ionosphere will increase the sidelobes and ringing of an otherwise low-sidelobe system. The simulations presented in this chapter do not include ionosphere effects, but the simulator is capable of modeling its dispersive properties.

2-2-2 SURFACE ROUGHNESS

The surface and subsurface layers of Mars will exhibit both large and small scales of roughness. Several types of models are available to describe rough surface scattering [9,10]. The Kirchhoff approximation and geometric optics solutions are generally used for the large-scale roughness, and the Small Perturbation Method (SPM) is used for the overlying small-scale roughness. There is also a combined model that assumes the small-scale roughness is modulated by the large-scale roughness. Integral Equation Methods (IEM) can also be used to compute scattering from surfaces with wide range of roughness scales [11].

For scattering computations, the surface and subsurface layers are generally approximated by a randomly varying height profile. The probability density function of the height at a given location is expressed as a zero mean Gaussian random variable of the form

$$f_H(h) = \frac{1}{\sqrt{2\pi}\sigma_h} \exp\left\{-h^2 / 2\sigma_h{}^2\right\}, \tag{2-2}$$

where σ_h is standard deviation of the surface height. The height probability for two surface locations is expressed as a joint Gaussian distribution in which the correlation coefficient is dependent on the distance, ρ, between the two locations.

$$C_s(\rho) = \exp\left(-\rho^2 / l^2\right) \tag{2-3}$$

Shown in (2-3), the correlation length, l, is also used to describe a random rough surface and can be related to the root mean square of the surface slope, σ_s, by the relation

$$\sigma_s^2 = \sigma_h^2 \left| C_s''(0) \right| = 2\frac{\sigma_h^2}{l^2}. \tag{2-4}$$

For large-scale roughness, the scattered fields are dominated by the specular reflections off surface facets. The direction of the scattered fields is determined by the slopes, both $\alpha_s = \partial h/\partial x$ and $\beta_s = \partial h/\partial y$, of the surface height. The probability density function for these slopes is expressed by a joint probability function for two independent Gaussian variables with standard deviation, σ_s. Table 2-1 gives approximate values for both the large and small scales of roughness for the Martian surface [12], while Figure 2-3 shows the large-scale global surface roughness along with the height profile from the northern pole to the southern pole. The data shown in Figure 2-3 were collected by the Mars Orbiter Laser Altimeter (MOLA) over 35 km windows using 300 m baselines [13].

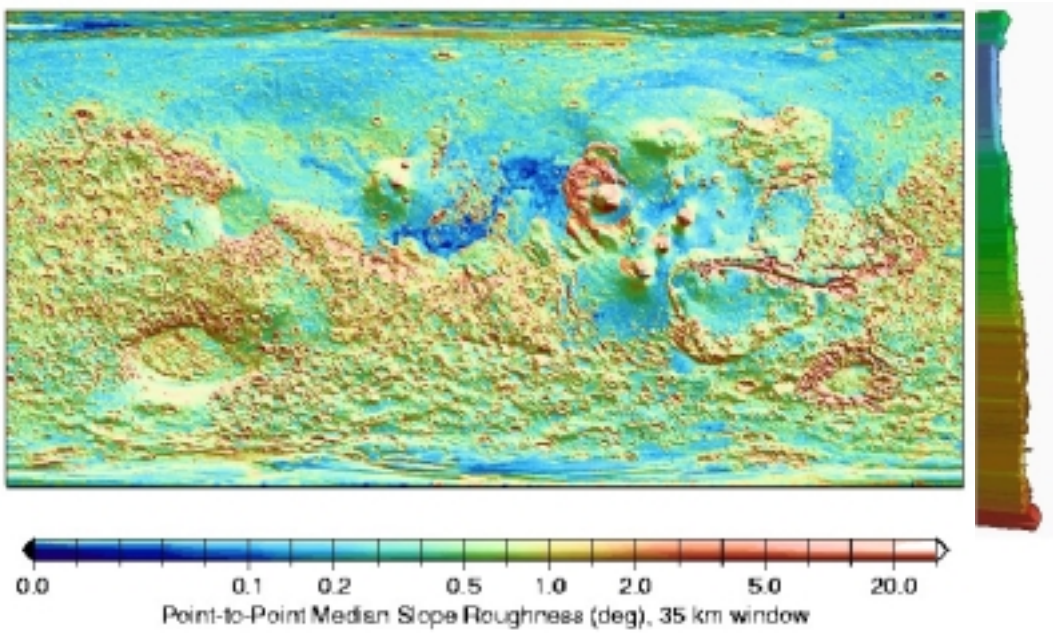

Figure 2-3. Global surface roughness and height profile.

Table 2-1. Estimated Roughness for Large and Small Scales

	Large Scale	Small Scale
σ: r.m.s. height	–	0.1m - 1m
l: correlation length	200m - 10km	–
σ_s: r.m.s. slope	<0.02 rad	0.1 - 0.5 rad

2-3 SOIL COMPOSITION

The primary resources for estimating the electrical properties, complex permittivity and permeability, of the Martian subsurface include surface measurements from the Viking Landers and Pathfinder Mission, analogies to lunar samples, SNC (Shergotty, Nakhla, Chassigny) meteorites, and interpretations from visible images. The dielectric constant, real part of the relative permittivity, is estimated to vary within the range of 2.5 to 9 depending on the porosity of the medium [14-16]. However, there is little information on the permeability and electrical loss of the soil. For example, due to its red color, Mars may contain a large amount of iron in the soil, which would translate into an increase in the electrical loss, but there have been no direct measurements of the electrical loss at the frequencies of interest for a surface-penetrating radar.

2-3-1 MAGNETIC PROPERTIES

Both Viking Landers and the Pathfinder Lander/Sojourner Rover contained magnets to measure the magnetic properties of the soil and atmospheric dust. Results from the Viking experiments estimated a 1 to 7 % weight of magnetic minerals. The Pathfinder magnetic experiment used an array of magnets, each with different strengths, to help determine the specific phase of the magnetic component of the soil. These experiments concluded that "Many of the particles currently suspended in the Martian atmosphere are magnetic, with an average saturation magnetization of about 4 Am^2/kg [17]." Also, for both Viking and Pathfinder, the phase of the magnetic component was estimated (speculated) to be maghemite, a mineral very similar to magnetite.

At low frequencies, the permeability of a basalt with 2 to 5 % magnetite has been shown to vary between 1.08 and 1.18 [18]. At these low frequencies (less than 30 kHz) the imaginary part of the permeability for a liquid-maghemite mixture was small, below 0.1, and showed no frequency dependencies [19]. Little information is given concerning higher frequency magnetic losses for soils containing magnetite or maghemite and care should be taken when extrapolating these values to SPR frequencies. However, since the main reason for examining the electrical properties is to investigate the basic factors influencing electromagnetic reflection and attenuation, incorporating both magnetic and electrical losses into the imaginary part of the permittivity will be sufficient, keeping in mind that magnetic properties may drastically increase the overall loss.

2-3-2 ELECTRICAL PROPERTIES

Table 2-2 shows the estimated dielectric constants for varying surface materials of Mars measured by the Viking Landers. The materials range from drift (sand) to cloddy (soil) to solid rock, which shows the highest dielectric constant value due to the low porosity. These values agree with Mars' average visible reflectivity of 6.4% corresponding to a dielectric constant of 2.8 [20].

For a sample of soil, the composition can be broken down into four parts including dry solid soil, iron oxide or other conductive materials, air, and water as shown in Figure 2-4. Additionally, water can exist as pure liquid water, salt water, or ice. The electrical properties of the mixture are determined by first calculating the electrical properties of the individual parts and then applying empirical mixing formulas.

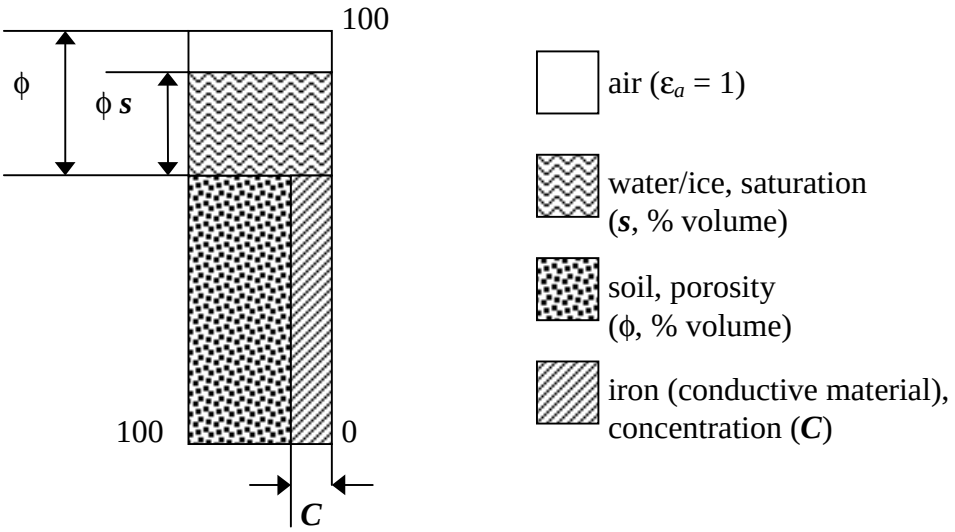

Figure 2-4. Soil model containing of air, water, soil, and iron.

Table 2-2. Estimated Dielectric Constants of Mars' Surface Materials

Surface Material	Dielectric Constant	Size
Drift (Sand)	2.4	0.1-10 um
Crusty-Cloddy (Soil)	2.4-3.8	0.1-10 um
Blocky (Soil)	2.4-4.5	–
Rock	8	0.035-0.45 m

A common analog for the soil properties of Mars is the Moon. "The observed Martian surface pressures, temperatures, and water contents are consistent with a model of the planetary surface which is electrically similar to that of the Moon [15]." For frequencies above 100 kHz, the equation governing the electrical properties of a mixture follows a geometric mean mixing formula [16],

$$\varepsilon_m = \varepsilon_a^{\phi(1-s)} \varepsilon_w^{\phi s} \varepsilon_s^{(1-\phi)}, \qquad (2\text{-}5)$$

where ε_a is the permittivity of air, ε_w is the permittivity of the water phase, ε_s is the permittivity of solid soil, and ε_m is the permittivity of the mixture. For lunar samples, the permittivity and loss tangent of a solid soil can be expressed as

$$\varepsilon_s' \cong 9.0 \text{ and} \tag{2-6}$$

$$\tan\delta_s = \varepsilon_s''/\varepsilon_s' \cong (1.75 + 82.5C)\cdot 10^{-3} \text{, where} \tag{2-7}$$

$$\varepsilon_s = \varepsilon_s' - j\varepsilon_s'' \tag{2-8}$$

and C is the concentration of iron oxide in the soil. Equations (2-6) and (2-7) show an interesting relationship between the electrical properties of soil and the chemical composition. The dielectric constant is only a function of the density and is not dependent on chemistry, while the loss tangent is dependent on the chemical composition. This is the main reason why the real part of the permittivity of the Martian soil can be estimated to a higher degree of certainty than the permeability and electrical losses. The factors that influence the real permittivity are more easily measured or inferred from visible images and lunar analogs, while factors that influence the losses must be directly measured.

The permittivity of water follows a simple Deybe equation as

$$\varepsilon_w = \varepsilon_\infty + \frac{\varepsilon_{st} - \varepsilon_\infty}{1 - j\omega\tau_r} \tag{2-9}$$

where ε_∞ is the "infinity" or high-frequency permittivity, ε_{st} is the "static" or low-frequency permittivity, τ_r is a relaxation time, and ε_w is the permittivity of the water phase. The relaxation time indicates the frequency, approximately $1/\tau$, at which there is a transition in the permittivity from the static value to the high frequency value. Table 2-3 shows the values for both liquid water and ice at 25°C and -10°C, respectively. For a surface-penetrating radar operating anywhere from a few megahertz to a gigahertz, the permittivity of ice will be around the high-frequency value of 3.2 and the permittivity of water will be around the low-frequency value of 78. Furthermore, if there are any salts or impurities present within the water, an additional conductivity term must be included.

$$\varepsilon_w = \varepsilon_\infty + \frac{\varepsilon_{st} - \varepsilon_\infty}{1 - j\omega\tau_r} - j\frac{\sigma_e}{\varepsilon_0 \omega} \tag{2-10}$$

Figure 2-5 shows the permittivity of an air/soil/ice mixture with the porosity and saturation varying between 0 to 50 % and 0 to 100 %, respectively. The results show that the permittivity of a soil with 50 % porosity and 100 % ice saturation is practically indistinguishable from an unsaturated dry soil with 30 % porosity. This result reinforces the notion that unambiguous detection of ice using radar reflectivity alone is almost impossible.

Table 2-3. Water and Ice Parameters

	Water at 25°C	Ice at -10°C
ε_∞	4.2	3.2
ε_{st}	78.3	95.3
τ_r	8.5×10^{-12} [s]	5.4×10^{-5} [s]

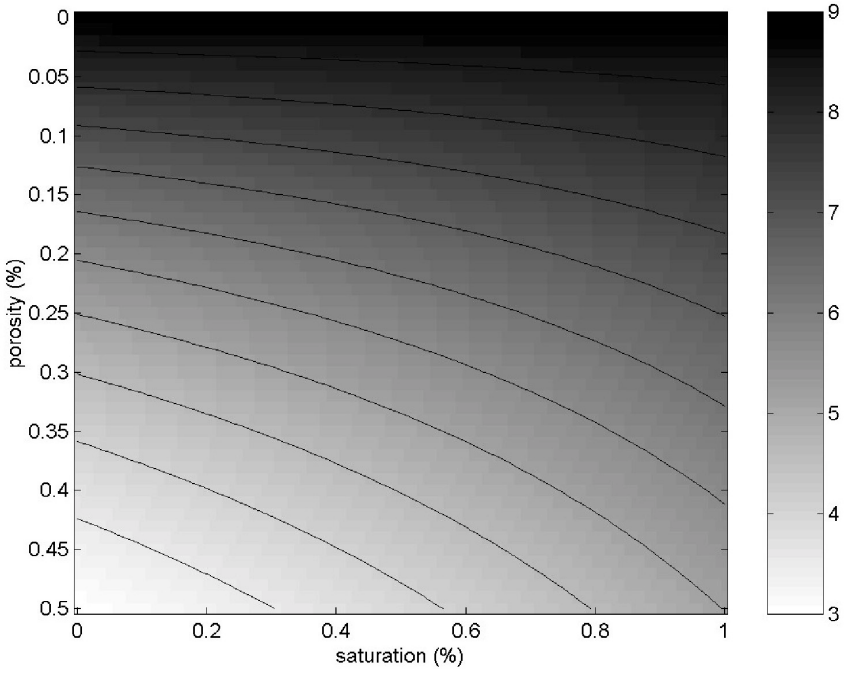

Figure 2-5. Permittivity of an air/soil/ice mixture.

2-3-3 JSC-1 SOIL SIMULANT

In addition to using the properties defined from the equations listed above, a sample of a Martian soil simulant, Mars JSC-1, was obtained from the Johnson Space Center in Houston, Texas. The simulant, which is an ash collected from a volcano in Hawaii, is sifted to better resemble a fine soil and then baked to remove any moisture. "It is claimed to approximate the reflectance spectrum, mineralogy, chemical composition, grain size, density, porosity, and magnetic properties of the oxidized soil on Mars [21]." Measurements of the soil's transmission and reflection coefficients were made over the frequency range of 4 MHz to 100 MHz using an air-dielectric coaxial cable and network analyzer. The electrical properties of the soil are then calculated from these measurements using iterative minimum mean square (MMS) and gradient methods [22-24]. Figure 2-6 shows the experimental setup and a detailed view of the coaxial cable. The complex permittivity and permeability determined using the gradient method are shown in Figure 2-7. Results for the MMS are shown in [25].

The real part of the relative permittivity ranges from 4.5 at the lower frequencies down to 3 at the higher frequencies. This decrease is consistent with a single relaxation time. The imaginary part of the relative permittivity shows decreasing values inversely proportional to frequency. This behavior is consistent with a conductivity term. The high loss associated with this imaginary part of the relative permittivity also points to some conductivity, which could exist either as bound water moisture or metals. The real part of the permeability varies between 1 and 1.12, consistent with the values shown in section 2-3-1. The imaginary part of the permeability does not show any consistent trend, and the fluctuations could be due to measurement errors.

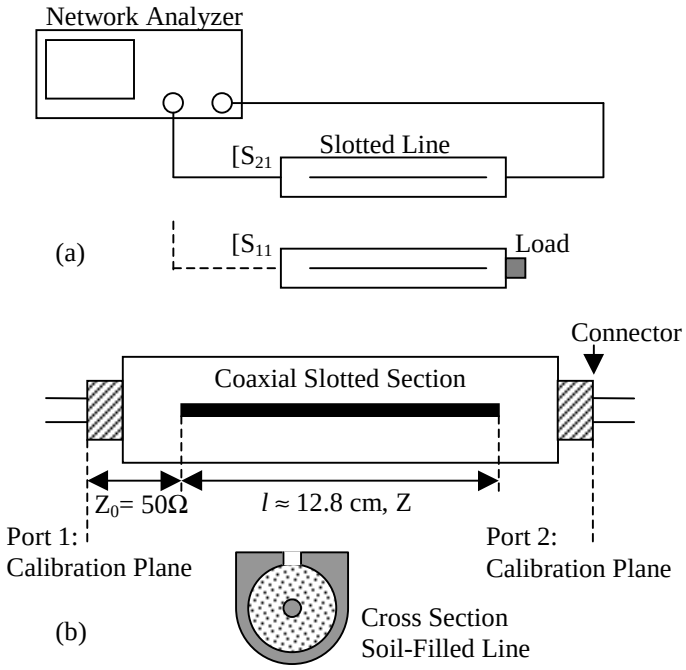

Figure 2-6. (a) Experimental setup for measuring soil parameters. (b) Air-dielectric coaxial cable.

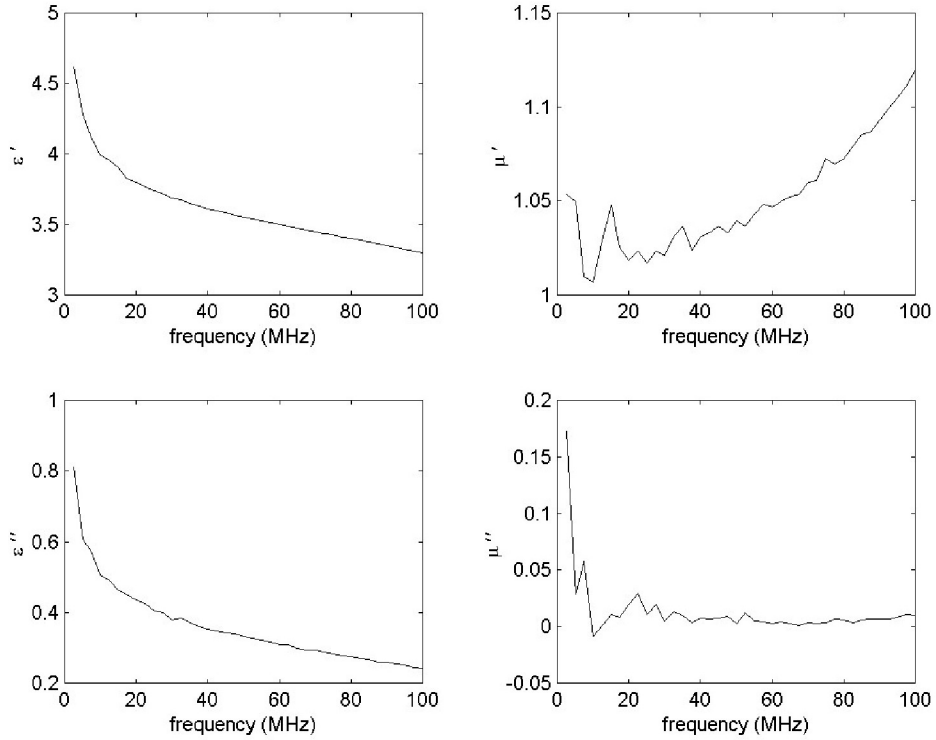

Figure 2-7. Permittivity and permeability results from dielectric measurements.

2-3-4 VOLUME DEBRIS: MIXING FORMULA

Mars may contain a considerable amount of debris buried within the near surface. This debris could be the result of volcanic flows, crater ejecta, or other resurfacing events. From surface observations, the size of rocks are estimated to vary between 1 cm to 7 m with a distribution as high as 30 % [26,27]. Electromagnetic waves propagating through the host medium are both attenuated and scattered by these rocks. This scattering is represented by a volumetric scattering coefficient, while the attenuation is included in the imaginary part of the permittivity using an effective medium approach [28]. For debris sizes much less than a wavelength, a simple Rayleigh approximation can be used to describe the scattering off of a single object, whereas for larger size inclusions the Mie approximation must be used. Also, as the volume fraction of particle inclusions increases, the Percus-Yevick pair distribution function can be included into the mixing formula to account for mutual coupling and multiple reflections between particles.

The effective permittivity of a background medium with spherical inclusions is given by [28]

$$\varepsilon_{eff} = \frac{1+2f_v(\varepsilon_d-\varepsilon_b)/(\varepsilon_d+2\varepsilon_b)}{1-f_v(\varepsilon_d-\varepsilon_b)/(\varepsilon_d+2\varepsilon_b)} - j2f_v k^3 a^3 \left|\frac{(\varepsilon_d-\varepsilon_b)/(\varepsilon_d+2\varepsilon_b)}{1-f_v(\varepsilon_d-\varepsilon_b)/(\varepsilon_d+2\varepsilon_b)}\right|^2 \frac{(1-f_v)^4}{(1+2f_v)^2} \tag{2-11}$$

where ε_b is the background permittivity, ε_d is the permittivity of the scattering debris, a is the radius of the debris, f_v is the volumetric fraction of the debris, and ε_{eff} is the effective permittivity. From (2-11) the amount of scattering loss experienced by an electromagnetic wave as it propagates through a random media will be dependent on a number of factors including the permittivity contrast between the background medium and scattering debris, the volume fraction of the debris, and the electrical size of the debris.

Also shown by (2-11), the imaginary part of the permittivity increases as a function of $(a/\lambda)^3$. Therefore, the loss increases as the third power of frequency and particle size. Figure 2-8a shows the attenuation (dB/km) versus frequency for 10 cm (solid), 20 cm (dashed), and 40 cm (dotted) inclusions with dielectric constants of 8 and volume fractions of 20 within a background media with a dielectric constant of 4. Figure 2-8b shows the attenuation constant for the 20 cm inclusions with volume fractions of 2.5 % (solid), 5 % (dashed), and 10 % (dotted). These plots show that the attenuation due to volume debris is much more sensitive to the size of the inclusion and not as sensitive to the volume fraction. In fact, the curve for the 10 % case (bottom dotted) is almost identical to that of the 20 % case (top dashed). The implications of this for a surface-penetrating radar is that, even if there is a small volume fraction of large objects, there will be significant attenuation, even at lower frequencies. From the Percus-Yevick pair distribution, the maximum attenuation occurs at a volume fraction of about 13 %.

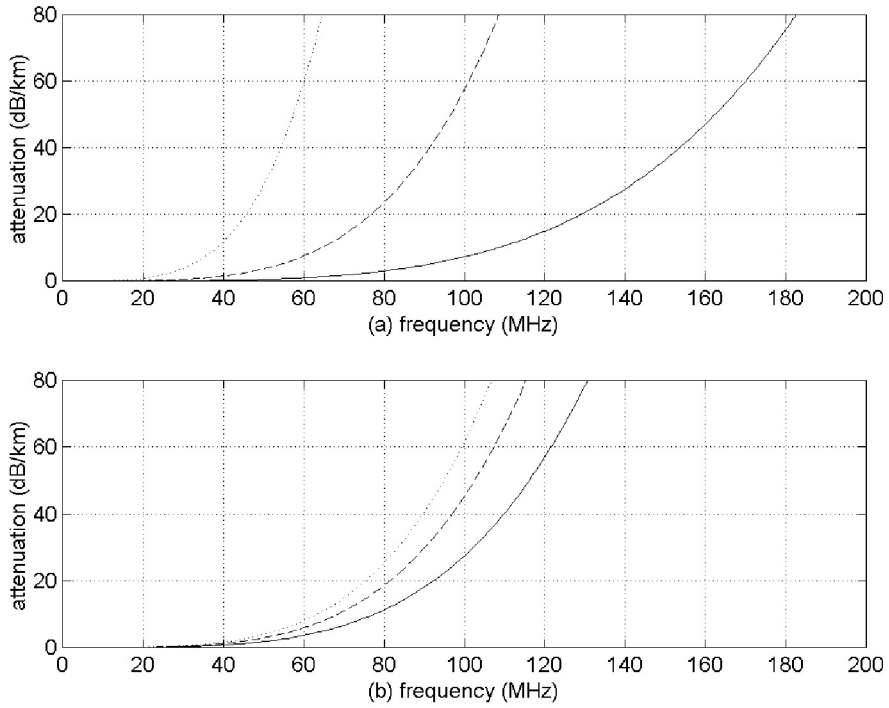

Figure 2-8. Attenuation constant versus frequency. (a) Object size: 10 cm (solid), 20 cm (dashed), 40 cm (dotted). (b) Volume fraction: 2.5 % (solid), 5 % (dashed), and 10 % (dotted).

2-4 RADAR SIMULATOR

In general, the received power from a radar target is expressed using the radar range equation,

$$P_r = \frac{P_t \lambda^2 G^2 \sigma_{cs}}{(4\pi)^3 R^4}, \tag{2-12}$$

where P_t is the transmit power, G is the antenna gain in the direction of the target, σ_{cs} is the target cross section, and R is the range of the target from the radar. For a distributed target, such as the surface or subsurface interface, the radar cross section is replace by a backscattering coefficient, σ^0, and the received power is determined by integrating over the illuminated area as

$$P_r = \frac{P_t \lambda^2}{(4\pi)^3} \int_A \frac{G(\theta,\phi)^2 \sigma^0(\theta,\phi)}{R(\theta,\phi)} da \tag{2-13}$$

Often, evaluation of this integral is difficult and approximations are made regarding the dependencies of the gain, range, and backscattering coefficient with respect to angle. The simulators described in following sections look at generating a radar response for the two cases of a perfectly flat layered media and a more complicated rough-surface model.

2-4-1 FIRST-ORDER SIMULATION: (PERFECTLY-FLAT LAYERED MEDIUM)

For the first-order simulations, a perfectly flat N-layered medium is considered using plane wave propagation. The backscattering coefficient for a flat surface is purely coherent and the radar range equation is modified using image theory resulting in the Friss transmission formula.

$$P_r = \frac{P_t \lambda^2 G^2 |\Gamma|^2}{4\pi (2R)^2} \tag{2-14}$$

Since the transmit power, wavelength, and antenna gain are characteristics of the radar system, the only factors that need to be determined are the reflection coefficient, the time delay corresponding to each subsurface layer including multiple bounces, and the spherical spreading loss. The reflection amplitudes and corresponding time delays can be obtained by determining the complex reflection coefficient as a function of frequency and performing an inverse Fourier transform. Additionally, for an orbital-based system where the height of the radar is much greater than the depth of investigation, spherical spreading can be approximated directly from the height of the radar above the surface, R_0.

The reflection coefficient as a function of frequency for a layered medium can be determined by considering plane-wave propagation. The fields in each layer, denoted by an x-polarized electric field and y-polarized magnetic field, are represented as the sum of a positive and negative z-directed plane wave,

$$\mathbf{E}_n(z) = \mathbf{E}_n^+ e^{-jk_n z} + \mathbf{E}_n^- e^{jk_n z} \text{ and} \tag{2-15a}$$

$$\mathbf{H}_n(z) = \mathbf{H}_n^+ e^{-jk_n z} + \mathbf{H}_n^- e^{jk_n z}, \tag{2-15b}$$

where k_n is the wave number in the n^{th} layer determined from the permittivity and permeability. The values for **E** and **H** can be expressed in terms of the incident wave by first setting the electric and magnetic fields in the last layer to contain only a negative directed wave,

$$\mathbf{E}_N(z) = e^{jk_N z} \text{ and} \tag{2-16a}$$

$$\mathbf{H}_N(z) = \frac{1}{\eta_N} e^{jk_N z}, \tag{2-16b}$$

where η is the impedance of the medium. Next, an iterative algorithm is used to calculate the fields at subsequent layers by ensuring that the fields are continuous across each boundary.

$$\mathbf{E}_n^+ e^{-jk_n d_n} + \mathbf{E}_n^- e^{jk_n d_n} = \mathbf{E}_{n+1}^+ e^{-jk_{n+1} d_n} + \mathbf{E}_{n+1}^- e^{jk_{n+1} d_n} \tag{2-17a}$$

$$\mathbf{H}_n^+ e^{-jk_n d_n} + \mathbf{H}_n^- e^{jk_n d_n} = \mathbf{H}_{n+1}^+ e^{-jk_{n+1} d_n} + \mathbf{H}_{n+1}^- e^{jk_{n+1} d_n} \tag{2-17b}$$

$$\frac{1}{\eta_n}\left[\mathbf{E}_n^+ e^{-jk_n d_n} - \mathbf{E}_n^- e^{jk_n d_n}\right] = \frac{1}{\eta_{n+1}}\left[\mathbf{E}_{n+1}^+ e^{-jk_{n+1} d_n} - \mathbf{E}_{n+1}^- e^{jk_{n+1} d_n}\right] \tag{2-17c}$$

Solving the system of equations, the fields in the nth layer can be expressed in terms of the fields in the nth+1 layer as

$$\begin{bmatrix}\mathbf{E}_n^+ \\ \mathbf{E}_n^-\end{bmatrix} = \frac{1}{2\eta_{n+1}}\begin{bmatrix}(\eta_{n+1}+\eta_n)e^{j(k_{n+1}-k_n)d_n} & (\eta_{n+1}-\eta_n)e^{j(-k_{n+1}-k_n)d_n} \\ (\eta_{n+1}-\eta_n)e^{j(k_{n+1}+k_n)d_n} & (\eta_{n+1}+\eta_n)e^{j(-k_{n+1}+k_n)d_n}\end{bmatrix}\begin{bmatrix}\mathbf{E}_{n+1}^+ \\ \mathbf{E}_{n+1}^-\end{bmatrix} \tag{2-18}$$

Working up to the first layer, the reflection coefficient at the surface is expressed as the ratio of the positive directed field divided by the negative directed field or, alternatively, the ratio of the reflected wave divided by the incident wave.

$$\Gamma = \frac{\mathbf{E}_0^+}{\mathbf{E}_0^-} \tag{2-19}$$

The result of such a simulation is analogous to the reflection from N transmission lines, each with different characteristic impedance and propagation coefficient, as shown in Figure 2-9. The amplitude response is shown as

$$U(f) = \frac{T(f)\sqrt{4\pi}\lambda G\Gamma(f)}{8\pi R_0}, \tag{2-20}$$

where $T(f)$ is the transmit waveform. A frequency modulated Gaussian waveform is used as the transmit waveform for all the simulations presented in this dissertation. This waveform is considered ideal and contains no sidelobes. In practice, the

waveforms produced by actual radar systems are less ideal and will contain sidelobes. These sidelobes will vary in both amplitude and duration depending on the type of radar system, bandwidth, and windowing functions.

2-4-1-1 EXAMPLE OF A TWO-LAYER MODEL

For an initial experiment, a simple two-layer model is used to test the simulator and compare the amplitude responses from layers with air, ice, or water. The model consists of an orbiting system at an altitude of 400 km, an upper surface layer consisting of dry eolian sediment with a porosity of 50 %, and a deeper layer consisting of a layered basalt with a porosity of 25 %. Additionally, the deep basalt layer is saturated with either air, water, or ice. The parameters of the simulation model are shown in Table 2-4 along with the dielectric constant for each layer. The incident waveform is a frequency-modulated Gaussian pulse with a 20 MHz center frequency and 5 MHz bandwidth.

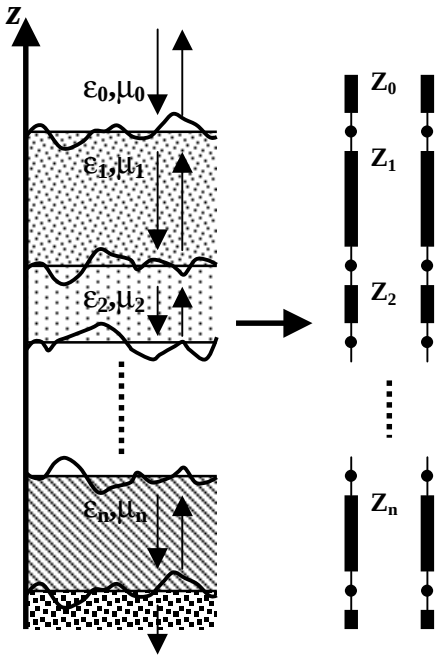

Figure 2-9. Representation of a flat N-layered medium.

Table 2-4. Two-Layer Simulation Model

Depth	Lithology	ϕ%	s%	fill	ε_r
400km	Air	100	-	-	1.0
100m	eolian sediment	50	0	air	2.8
-	layered basalt	25	0	air	4.8
			90	ice	6.2
			90	water	13.3

The link budget for the radar response is shown in Table 2-5. The total response for the surface normalized by the transmit power is calculated to be -117.5 dB. The response for the subsurface layer is calculated to be -124 dB, -120 dB, and -114 dB for the cases where the layer is filled with air, ice, or water. These reflections are consistent with the differences in dielectric contrasts for each fill material. Figure 2-10 shows the return signals generated by the simulator for the three cases. One additional simulation was conducted in which the basalt was filled with water, and the eolian sediment had a loss tangent of 0.025. The attenuation caused by the ohmic loss of this layer can be calculated by considering the attenuation constant of a low-loss dielectric,

$$\alpha \cong \frac{\omega\varepsilon''}{2}\sqrt{\frac{\mu}{\varepsilon'}} = \frac{\omega\tan\delta}{2}\sqrt{\mu\varepsilon'} = \frac{\pi f}{v}\tan\delta \text{ (Np/m)}, \qquad (2\text{-}21)$$

where δ is the loss angle. For a loss tangent of 0.025 and a two-way distance of 200 m, the additional loss for the subsurface interface is about 15 dB. Looking back at the original simulation, the difference between the radar response for the cases where the basalt is filled with air versus ice is only about 10 dB. This clearly shows that even a small change in loss tangent of an overlying layer could make the reflection off a water-saturated layer resemble that of a dry layer. This reinforces the notion that unambiguous detection of a subsurface layer of water or ice from reflectivity alone is unlikely, or even impossible.

Table 2-5. Link Budget for the Two-Layer Model

Transmit Power		Normalized	0 dB
Antenna Effective Area		$4\pi\lambda$	34.5 dB
Antenna Gain		dipole	0 dB
Spherical Spreading		$1/(8\pi R_0)^2$	-140 dB
Reflection (Surface)		Γ_0^2	-12 dB
Total	**(Surface)**		**-117.5 dB**
Transmission	(Surface)	$(1-\Gamma_0^2)^2$	-0.5 dB
Reflection	(air)	Γ_1^2	-18 dB
	(ice)		-14 dB
	(water)		-8.5 dB
Total	**(air)**		**-124 dB**
	(ice)		**-120 dB**
	(water)		**-114.5 dB**

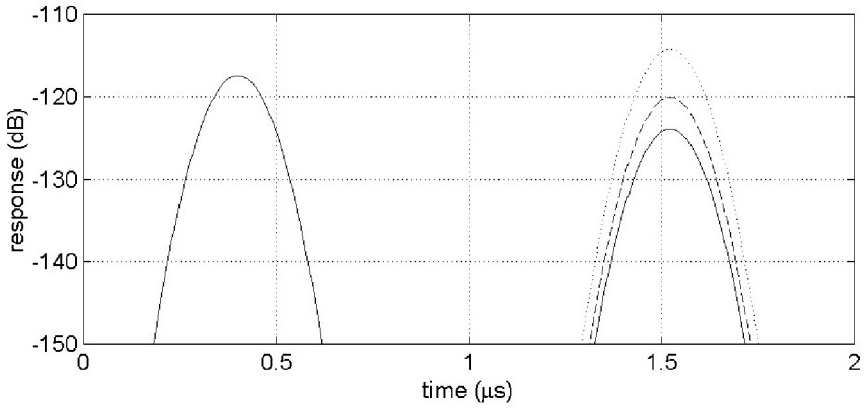

Figure 2-10. Simulation results for the two-layer model. First peak is the surface response and the second peak is the response of the subsurface layer: (solid) dry basalt, (dashed) ice-saturated basalt, and (dotted) water-saturated basalt.

2-4-2 SECOND-ORDER SIMULATION: (ROUGH SURFACE - GEOMETRIC OPTICS APPROXIMATION)

The plane-wave simulator shown in the previous section assumes perfectly flat surfaces. Incorporating clutter from rough surfaces is essential for realistic assessment of radar performance. In the next few sections, the basic equations

governing the scattering effects of rough surfaces will be reviewed for inclusion into the simulations.

For a surface with a large standard deviation of surface heights, the geometric optics approximation of the backscattering coefficient can be used. This approximation expresses the reflected field as a function of the surface slope, and since the entire surface never resembles a level plane, there is no coherent or specular reflection. The backscattering coefficient is simply a superposition of the specular reflections off surface facets that are oriented perpendicular to the incident wave. The probability that a specific location will be perpendicular to the incident wave is taken directly from the probability density function of the surface slope.

$$f_{A,B}(\alpha_s, \beta_s) = \frac{1}{2\pi\sigma_s^2} \exp\left\{-\left(\alpha_s^2 + \beta_s^2\right)/2\sigma_s^2\right\} \tag{2-22}$$

For an incident angle θ, the probability that the surface will be perpendicular is given by

$$f_{\Theta}(\theta) = \frac{1}{2\pi\sigma_s^2} \exp\left\{-\tan^2\theta/2\sigma_s^2\right\} \tag{2-23}$$

Normalizing by the illuminated area and including spherical spreading results in the non-coherent part of the backscattering cross section [14,15].

$$\sigma^0 = \frac{|\Gamma_0|^2 \exp\left\{-\tan^2\theta/2\sigma_s^2\right\}}{2\sigma_s^2 \cos^4\theta}. \tag{2-24}$$

The relationship of (2-24) to θ shows a fast drop off with incidence angle for angles greater than about 15°. This value depends on the rms slope. Using Figure 2-11, equation (2-24) can be rewritten in terms of the geometry.

$$\sigma^0 = \frac{\left|\Gamma_0\right|^2 \exp\left\{\dfrac{R_0^2 - R^2}{2R_0^2 {\sigma_s}^2}\right\}}{2{\sigma_s}^2 R_0^4 / R^4} \tag{2-25}$$

Defining $t_p = t - t_0$ as time referenced to the surface reflection, where $t = 2R/c$ and $t_0 = 2R_0/c$, the numerator of the exponent is expressed as

$$R_0^2 - R^2 = \left(\frac{1}{2}c\right)^2 \left[t_0^2 - \left(t_p^2 + 2t_0 t_p + t_0^2\right)\right] \cong \left(\frac{1}{2}ct_0\right) ct_p = R_0 ct_p, \tag{2-26}$$

and the backscattering coefficient as a function of time delay is approximated as

$$\sigma^0 = \frac{\left|\Gamma_0\right|^2 \exp\left\{-\dfrac{ct_p}{2R_0 {\sigma_s}^2}\right\}}{2{\sigma_s}^2}. \tag{2-27}$$

Equation (2-27) shows that the response of a rough surface will exhibit an exponential decay versus time. The rate of decay is inversely proportional to both the height of the radar and the rms slope of the interface.

The total backscattered power depends directly on the illuminated area, which for a nadir looking system will be a circular ring. This area is expressed as

$$A = 2\pi x \cdot \Delta x \tag{2-28}$$

where x is the radius, Δx is the width of the ring, and A is the area as shown in Figure 2-11. This figure also demonstrates the clutter problem associated with an orbiting surface-penetrating radar system. For an interface at depth, z, the reflection off of this interface needs to be greater than the backscattered power from the shaded area on the surface. The radius of the ring is expressed as

$$x = \sqrt{R^2 - R_0^2} \tag{2-29}$$

and the width is approximated using an expansion

$$\Delta x \cong \frac{R\Delta z}{\sqrt{R^2 - R_0^2 + \left(\Delta z/2\right)^2}} \cong \frac{R_0 \Delta z}{x}. \tag{2-30}$$

The final area of the circular ring is determined by substituting (2-30) into (2-28).

$$A = 2\pi x \cdot \frac{R_0 \Delta z}{x} = 2\pi R_0 \Delta z \tag{2-31}$$

When the backscatter is calculated from an illuminated area, that backscatter is then used to describe a random variable for the reflected signal. Assuming the illuminated area is a collection of many scattering surfaces (that may add coherently or non-coherently), and if the phases are uniformly distributed between 0 and 2π, then from the central limit theorem the complex voltage response from that area will be a zero mean Gaussian random variable, the magnitude response will be a Rayleigh random variable, and the power will be an exponential random variable.

To include the effects of a randomly varying rough surface into the simulations, the one-dimensional plane-wave response is first calculated to obtain values for $\Gamma(f)$. Next, a clutter response is calculated from a single interface with a normalized reflection coefficient. This response is dependent on the surface roughness, antenna pattern, and radar height.

$$A\sigma^0 = \frac{\pi R_0 \Delta z \left|\Gamma\right|^2}{\sigma_s{}^2} \exp\left\{-\frac{ct_p}{2R_0\sigma_s{}^2}\right\} \tag{2-32}$$

Remember that (2-32) describes the power of a random variable. For an orbital system where angle of incidence is near zero, the antenna gain can be assumed constant. Since the backscattering coefficient is non-coherent, the voltage (amplitude) response will be a non-stationary exponentially decreasing zero-mean

Gaussian random variable. The total response is determined by convolving this clutter response with the one-dimensional plane-wave response and also accounting for system parameters and spherical spreading loss. The total radar response can now be expressed as a convolution in the time domain as

$$P_r = \frac{P_t \lambda_c^{\,2} G^2 \Delta z}{4(4\pi)^2 R_0^3 \sigma_s^{\,2}} \left[\left|\Gamma(t)\right|^2 \otimes \exp\left\{ -\frac{ct_p}{2R_0 \sigma_s^{\,2}} \right\} \right]. \tag{2-33}$$

Relating (2-33) to (2-14), the signal reduction caused by a rough surface compared to that of a specular response can be obtained as

$$\frac{A\sigma^0}{\left|\Gamma\right|^2 (2\pi R_0)^2} = \frac{2\pi R_0 \Delta z \left|\Gamma\right|^2}{\left|\Gamma\right|^2 (2\pi R_0)^2 2\sigma_s^{\,2}} = \frac{\Delta z}{4\pi R_0 \sigma_s^{\,2}}. \tag{2-34}$$

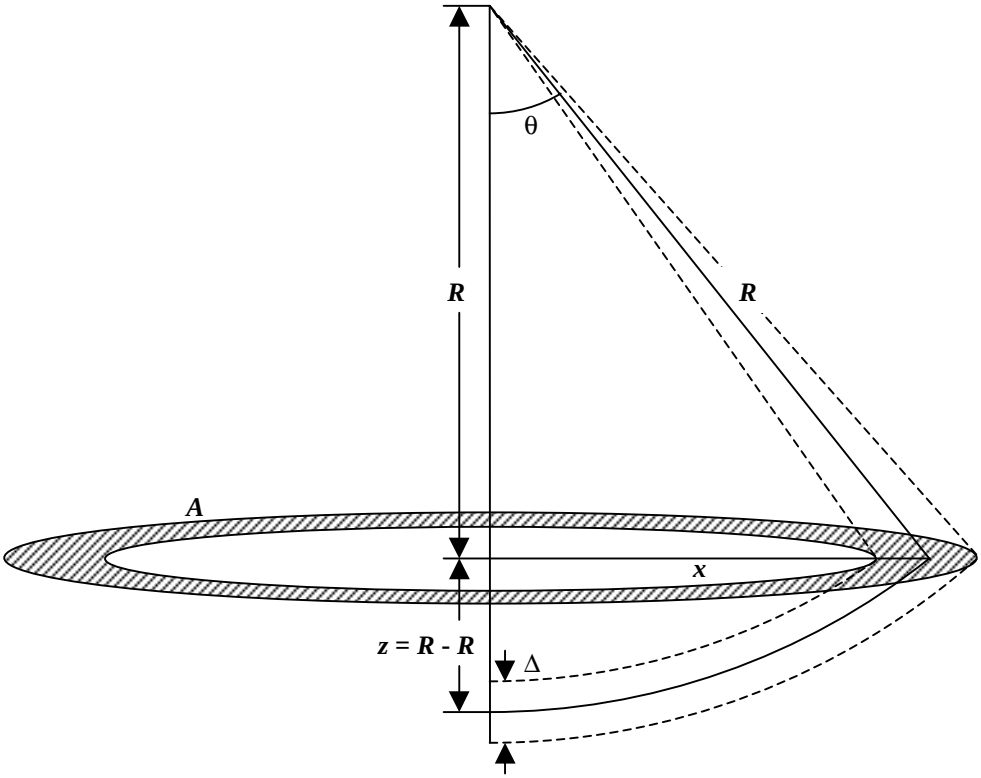

Figure 2-11. Geometry for calculating the illuminated area.

The above equation indicates that for very small surface slopes the reflection from a rough surface is greater than that of a purely specular response. This, however, is not true, because the geometric optics approximation is only valid for surfaces with large scales of roughness. The validity conditions for the geometric optics approximation are as follows [9]:

$$kl > 6, \tag{2-34a}$$

$$l^2 > 2.76\sigma\lambda, \text{ and} \tag{2-34b}$$

$$k\sigma > 2, \tag{2-34c}$$

Using values from Table 2-1 for the larger scale of roughness, the geometric optics approximation should be valid for frequencies greater than about 1.5 MHz.

2-4-2-1 GENERATING THE RESPONSE OVER A SYNTHESIZED APERTURE

Generating the radar response from a rough surface over a lateral traverse becomes more complicated since a portion of the surface area will stay illuminated. The reflected signal from this part of the illuminated area will stay coherent over the traverse, while the remainder will fluctuate. To simulate this response, the response from a normalized point scatterer versus incident angle is calculated first. This response, at normal incidence, is identical to that of the specular response. The response versus incident angle is calculated by time shifting and amplitude scaling the specular response by values corresponding to the antenna pattern and backscatter. Once the response from the point scatterer is generated, the response over the lateral traverse can be obtained by convolving the response with a two-dimensional random variable describing the roughness parameters of the surface. This entire process is shown in Figure 2-12.

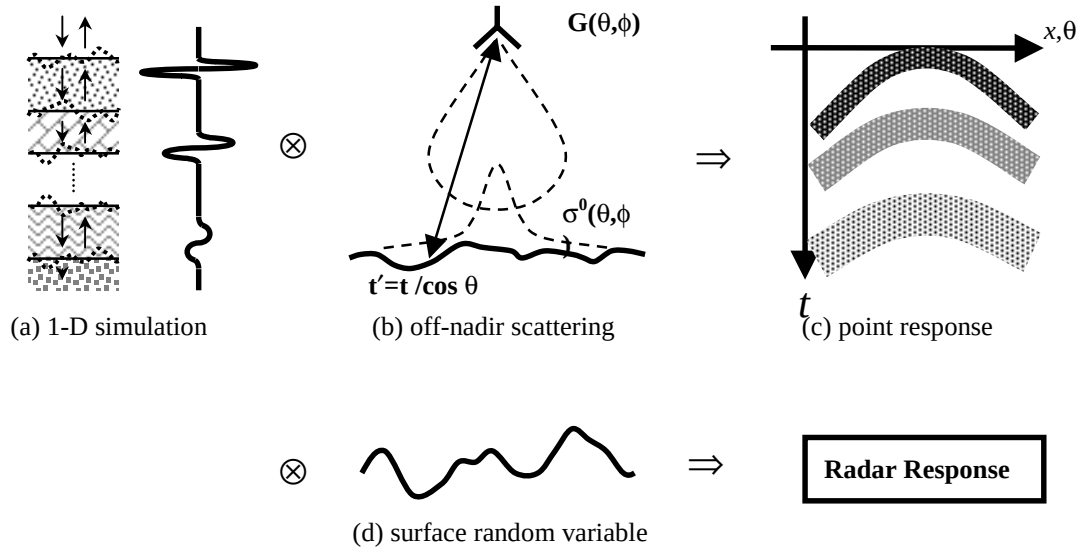

(a) 1-D simulation (b) off-nadir scattering (c) point response

(d) surface random variable

Figure 2-12. Process for calculating the radar response over a traverse. The (a) specular response, (b) off-nadir scattering parameters, (c) point response, (d) surface random variable.

2-4-2-2 ROUGH SURFACE EXAMPLE OF A TWO-LAYER MODEL

The same model that was used in section 2-4-1-1 will be considered as an example for a rough surface simulation. The specific case of the air-filled basalt will be used with a 20 MHz center frequency, 10 MHz bandwidth incident pulse. The layers will have rms slopes of 0.005 rad and 0.01 rad. Figure 2-13 shows the simulated responses for the two cases of surface slopes. For an rms slope of 0.005 rad, shown by the dashed line, the two reflections can be easily distinguished; however, for an rms slope of 0.01, the decay of the surface responses decreases more slowly making it more difficult to resolve the two reflections. Figure 2-14 shows the point response and response over a lateral traverse for the 0.01 rms slope.

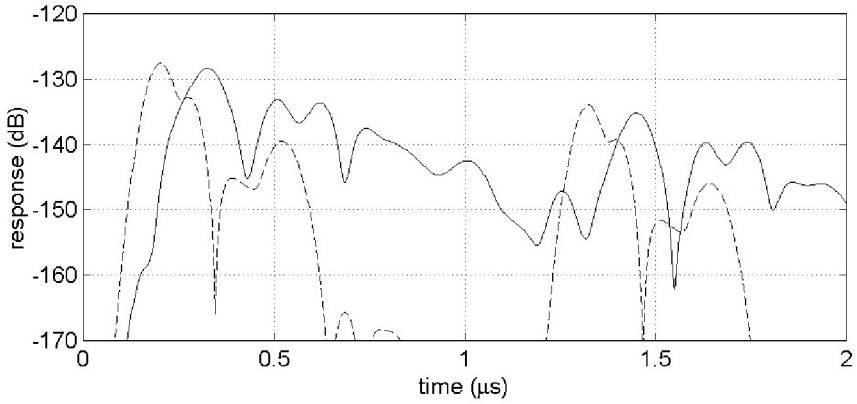

Figure 2-13. Simulated rough surface response of a two-layer model. Responses are for a 20 MHz center frequency, 10 MHz bandwidth incident pulse.

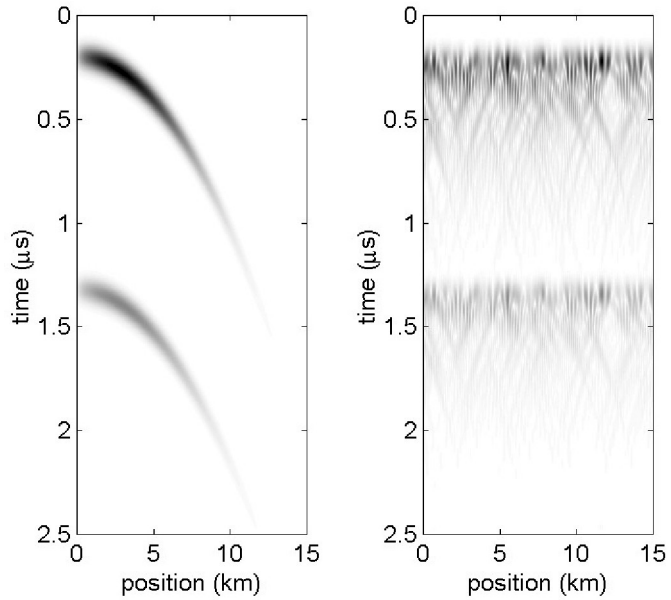

Figure 2-14. (a) Point response, and (b) rough-surface response over a lateral aperture for the two-layer model.

2-4-3 MARS SIMULATION MODELS

Recently, stratigraphy models for different geological locations on Mars were developed [29]. Table 2-6 shows the stratigraphy and lithology of a site containing subsurface ice deposits and a near-surface aquifer. Additional parameters include 5 % iron and 10 cm volume debris with a volume fraction of 5 %. For the first simulation with this model, a 5 MHz modulated Gaussian pulse with an effective 3-dB bandwidth of 3 MHz is used as the transmit signal. Figure 2-15a shows the resulting received waveform for a specular simulation. Next, the frequency of operation and bandwidth are increased by a factor of 10 (50 MHz center frequency, 30 MHz bandwidth), the same simulation is conducted, and the results are shown in Figure 2-15b. Compared to the 5 MHz simulation, the 50 MHz signal was not able to detect the deep layer due to attenuation from the water. Since there was no significant signal return from the deeper interface, only the upper portion of this simulation is shown in the Figure 2-15c. Even though the 50 MHz signal was not able to detect the deeper interface, it was able to resolve the fine-scale layering near the surface. This simulation reinforces the basic frequency, depth-penetration trade-off associated with surface-penetrating radar. Additional simulations are listed in Appendix B.

Table 2-6. Simulation Model: NS-5 Simple Near-Surface Aquifer

depth	Lithology	ϕ%	s%	fill
400km	air	100	-	-
1	eolian sediment	50	0	air
3	indurated sediment	15	0	air
5	sediment-filled basalt	50	100	ice
50	layered basalt	10	100	ice
55	eolian sediment	50	100	ice
205	layered basalt	10	100	water
225	fluvial sediment	20	100	water
1000	layered basalt	10	100	water

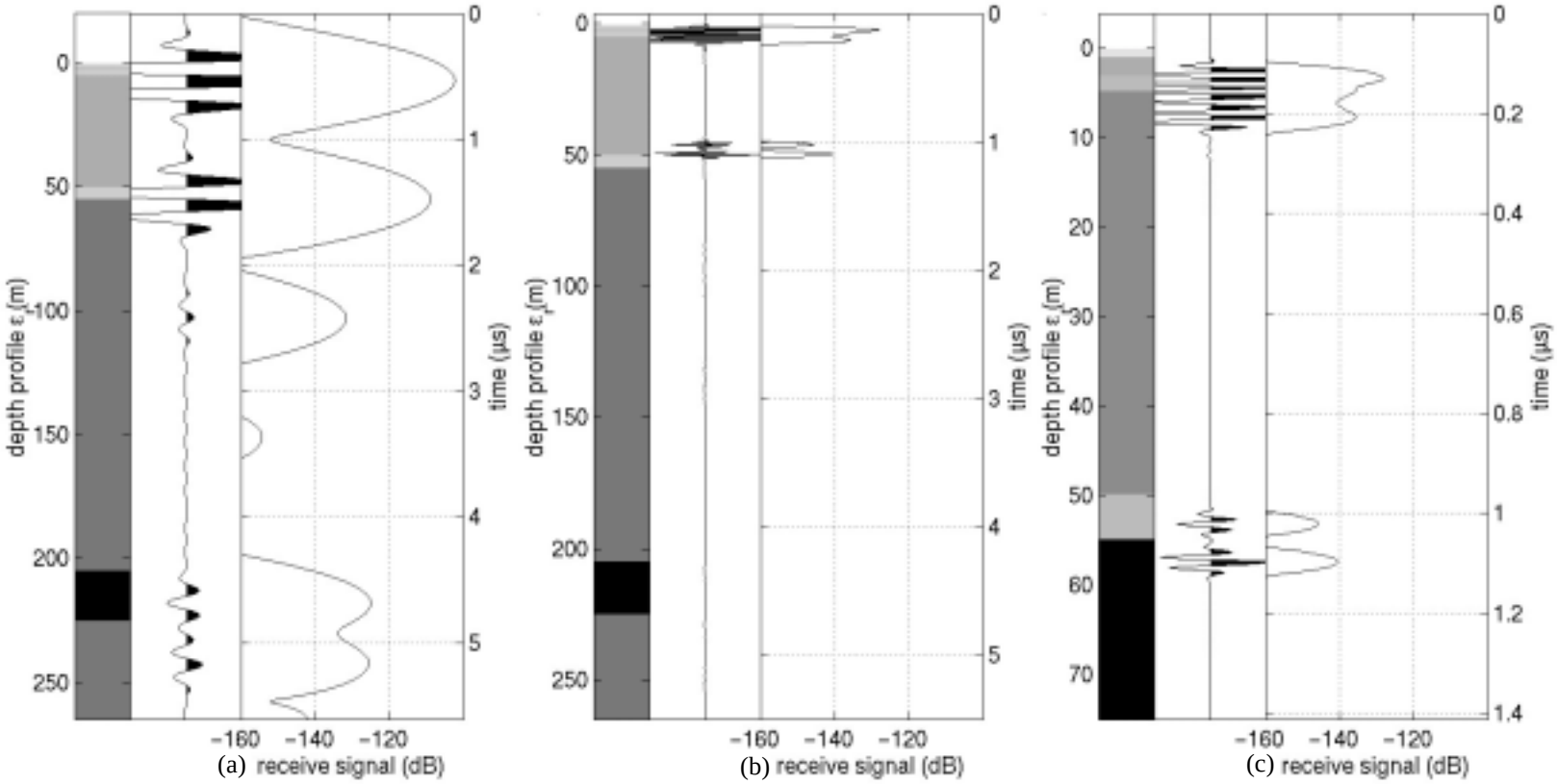

Figure 2-15. Simulation results for model NS-5. (a) Low frequency, deep penetration. (b) High frequency, shallow penetration. (c) Expanded view of the high frequency response.

2-5 SUMMARY OF PARAMETERS

Table 2-7 lists the factors and corresponding equations that influence the return signal for a surface-penetrating radar. The main factor contributing to a reflected signal is the dielectric contrast. Factors that attenuate the signal include ohmic losses, fine-scale layering, and volume debris. Ohmic losses dissipate the energy as heat, while the layering and volume debris scatter the energy at different angles. Furthermore, the scattered energy reflected back toward the radar system is detected as clutter. There is not an equation shown for the losses due to fine-scale resurfacing, but in general, these losses will be dependent on the number of layers, electrical thickness of these layers, and the dielectric contrasts. Surface roughness produces clutter from off-nadir incident angles that will mask deeper interfaces. As the height of the radar increases, the effects of surface roughness become more of a problem.

Table 2-7. List of Geophysical Factor Affecting Radar Performance

Dielectric Contrast	Reflection: Γ	$\frac{\sqrt{\varepsilon_1}-\sqrt{\varepsilon_2}}{\sqrt{\varepsilon_1}+\sqrt{\varepsilon_2}}$
Ohmic Losses	Attenuation: α (Np/m)	$\frac{\pi f}{v}\tan\delta$
Fine Scale Layering	Attenuation/Clutter	-
Volume Scattering	Attenuation: $\tan\delta$ Clutter: σ_{cs}	$\propto (a/\lambda)^3$ eq. (2-11) $\pi a^2 9(2\pi a/\lambda)^4$
Surface Roughness	Reflection/Clutter: $A\sigma^0$	$2\pi Hc\tau\frac{\lvert\Gamma\rvert^2 \exp\left(-ct/2R_0\sigma_s{}^2\right)}{2\sigma_s{}^2}$

2-5-1 TRADE-OFF EXAMPLE

For an orbital-based surface-penetrating radar, the detection problem for a subsurface interface is not as much a signal-to-noise ratio problem as it is a signal-to-clutter ratio problem. The equations for the clutter due to surface roughness and the attenuation due to ohmic losses both show an exponential decay with time. In order to detect a subsurface layer with reflection equal or less than that of the surface, the attenuation due to soil loss must be less that of the surface clutter.

$$\pi f \tan(\delta) t < \frac{c t_p}{2 R_0 \sigma_s^{\,2}} \qquad (2\text{-}36)$$

Equation (2-36) can be rewritten to put an upper bound on the operating frequency that is dependent on rms slope, loss tangent, and height of the system.

$$f < \frac{c}{2\pi \tan(\delta) R_0 \sigma_s^{\,2}} \qquad (2\text{-}37)$$

This shows the maximum frequency that can be used before the surface clutter will be greater that of the reflected signal. Using a loss tangent of 0.01 and radar height of 400km, (2-37) can be used with a map (Figure 2-3) of the surface roughness to show a global view of the maximum operation frequency versus geographical location as shown in Figure 2-16. This figure shows that for the very rough regions, shown in red, a very low frequency radar, in the kilohertz region, would be needed to obtain subsurface information, and, for the smooth regions, shown in blue, a high frequency radar up to a few gigahertz could be used. However, for the majority of the planet a radar operating around 20 MHz would be sufficient to overcome the surface clutter. The above discussion does not include any clutter cancellation scheme such as a second monopole antenna with a null at vertical. It also does not account for additional losses due to volume debris and fine-scale layering.

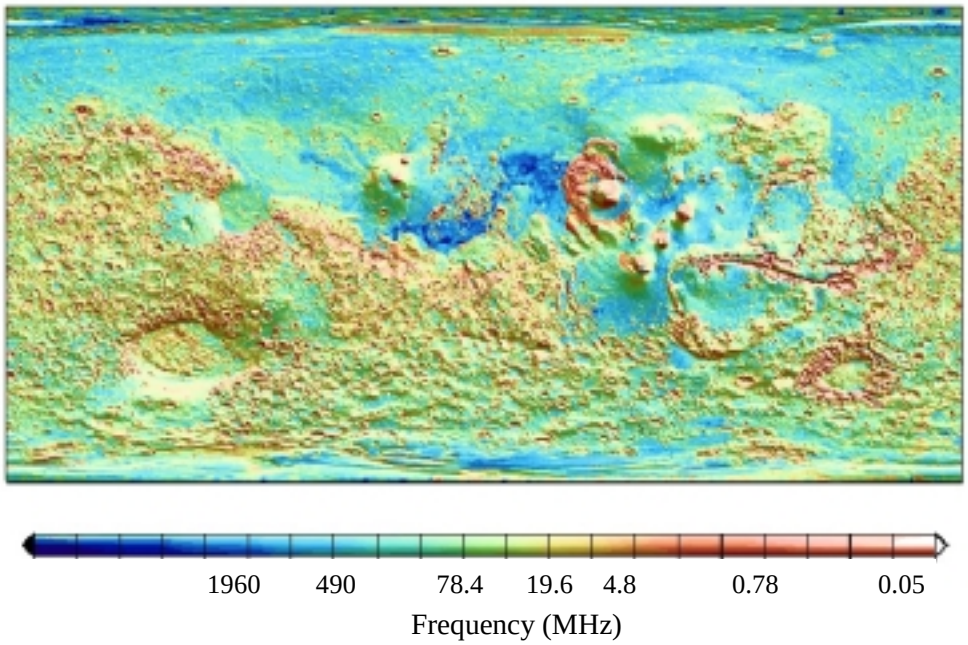

Figure 2-16. Maximum operating frequency to overcome surface clutter.

CHAPTER 3

RADAR SYSTEM

3-1 INTRODUCTION

For the preliminary experiments and testing, a simple surface-penetrating radar system was constructed. The purpose of the radar system is to provide a test-bed to investigate radar performance, system trade-offs, signal processing, and antenna subsystems. The prototype system was built with inexpensive evaluation boards and connectorized components. The system uses a digital synthesizer and can generate a variety of waveforms including a simple pulse, chirped pulse, FM-CW or other modulated signal. For initial testing a chirped pulse waveform is used to achieve low peak power, high average power, and fine resolution. This chapter begins by describing the basic construction and operation of the transmitter and receiver. Next, a few possible configurations for the antenna subsystems are presented.

3-2 TRANSMITTER AND RECEIVER

The transmitter and receiver sections of the radar system generate, amplify, and coherently process all the signals that are used by the system. For the chirped mode of operation, the transmit signal is a linearly frequency-modulated chirp ranging from 5 MHz to 120 MHz,

$$s_t(t) = A\cos\left(2\pi f_0 t + \pi\kappa t^2\right), \tag{3-1}$$

where A is the signal amplitude, f_0 is the start frequency, and k is the sweep rate. Without any weighting this results in a two-way free-space range resolution of about 1.3 m if the entire bandwidth is used. Upon reception, the delayed chirp signal is mixed with a replica of the transmit signal and low-pass filtered. This produces a low-bandwidth beat frequency signal that can be digitized relatively easily using a high-speed high-resolution analog-to-digital converter. The output of the low-pass filter is expressed as

$$s_r(t) = s_t(t)\cdot s_t(t-\tau) \tag{3-2}$$

$$s_r(t) = A^2\cos\left(2\pi\kappa\tau t - \pi\kappa\tau^2\right) \tag{3-3}$$

where $\kappa\tau$ is the beat frequency, f_b. The range profile is represented by inverse Fourier transforming the data where the time delay τ is proportional to f_b/κ:

$$s_r(\tau) = IFFT[s_r(t)] \tag{3-4}$$

The prototype transmitter/receiver subsystem is shown in Figure 3-1 and the block diagram of the system is shown in Figure 3-2. The system specifications are listed in Table 3-1. The transmitter subsystem generates the 5 MHz to 120 MHz chirp signal after receiving a trigger from the system controller. This chirp signal is generated using a 300 MHz Analog Devices direct digital synthesizer (DDS) evaluation board. Higher-order harmonics generated by the DDS are reduced with an

elliptical low-pass filter with a cut-off frequency of 120 MHz corresponding to 40 % of the clock frequency. Next, the signal is amplified with a high-power amplifier. A quality amplifier with a high third-order intercept point should be used, because any harmonics produced by the amplifier will appear as range sidelobes in the compressed data. With a power divider, the amplified signal is split into two parts, one for the transmit antenna subsystem and the other to serve as a local oscillator for the mixer that is used to de-chirp the received signal. Since the DDS chip has both positive and negative, in-phase and quadrature-phase outputs, the local oscillator can also be obtained directly from one of the three remaining analog outputs, thereby increasing the isolation between the transmitter and receiver. Due to the digital-to-analog conversion, the transmit signal will exhibit a sin(x)/x roll off.

The receiver subsystem converts the input RF response into an IF signal and digitizes the resulting signal. The IF signal is obtained by mixing a replica of the transmit signal with the receive signal producing a collection of beat frequency signals, each proportional to the product of the sweep rate and corresponding time delay of each reflector. These signals are low-pass filtered to remove the higher frequency components generated by the mixer. After low-pass filtering, a single-pole high-pass filter provides attenuation of the direct antenna coupling and an increased gain for the weak subsurface returns. The high-pass output is amplified and then digitized by a National Semiconductor 2.5 MSPS 16-bit analog-to-digital converter evaluation board.

All timing and control of the system are accomplished through the parallel port of a laptop computer and with a few low-speed digital integrated circuits. Evaluation software was used to trigger the system and store the data to memory. Unfortunately, the evaluation software did not include any drivers to automate this process, and data collection was relatively slow. This would not be a problem for a rover on Mars since the rover would move slowly to avoid rocks and conduct other

experiments. However, this was a problem for fieldwork since the data collection was slow and awkward. The complete system was constructed for less than a thousand dollars. Excluding batteries and the antenna subsystems, the system weighs about 1.5 kg with dimensions of 7 cm x 20 cm x 30 cm as shown in Figure 3-1. The complete system could be easily miniaturized using a single two-sided printed circuit board and surface mount components to satisfy weight and volume constraints of a rover.

To aid in data collection, a second transmitter/receiver system was constructed using a 16-bit 50 kSPS National Instruments PCMCIA data-acquisition card. This card came with the necessary drivers to develop automated control software using National Instruments LabVIEW graphical programming development software. Using this card, all timing and data acquisition were performed through one of the PCMCIA ports of a laptop computer, and the digital chirp synthesizer was programmed through the parallel port of the computer. The relatively low speed of the data acquisition card significantly reduced the maximum sweep rate of the system. Also, since the analog-to-digital converter was inside the computer (rather than inside the shielded aluminum case for the first system) the analog signal was sent over a ribbon cable from the receiver to the laptop. This non-shielded PCMCIA cable also carried the timing signals for the digital part of the system, and it picked up interference from some of the digital components and power supplies. Compared to the original system, the new system offered an improvement in the rate of data collection at the cost of higher noise interference.

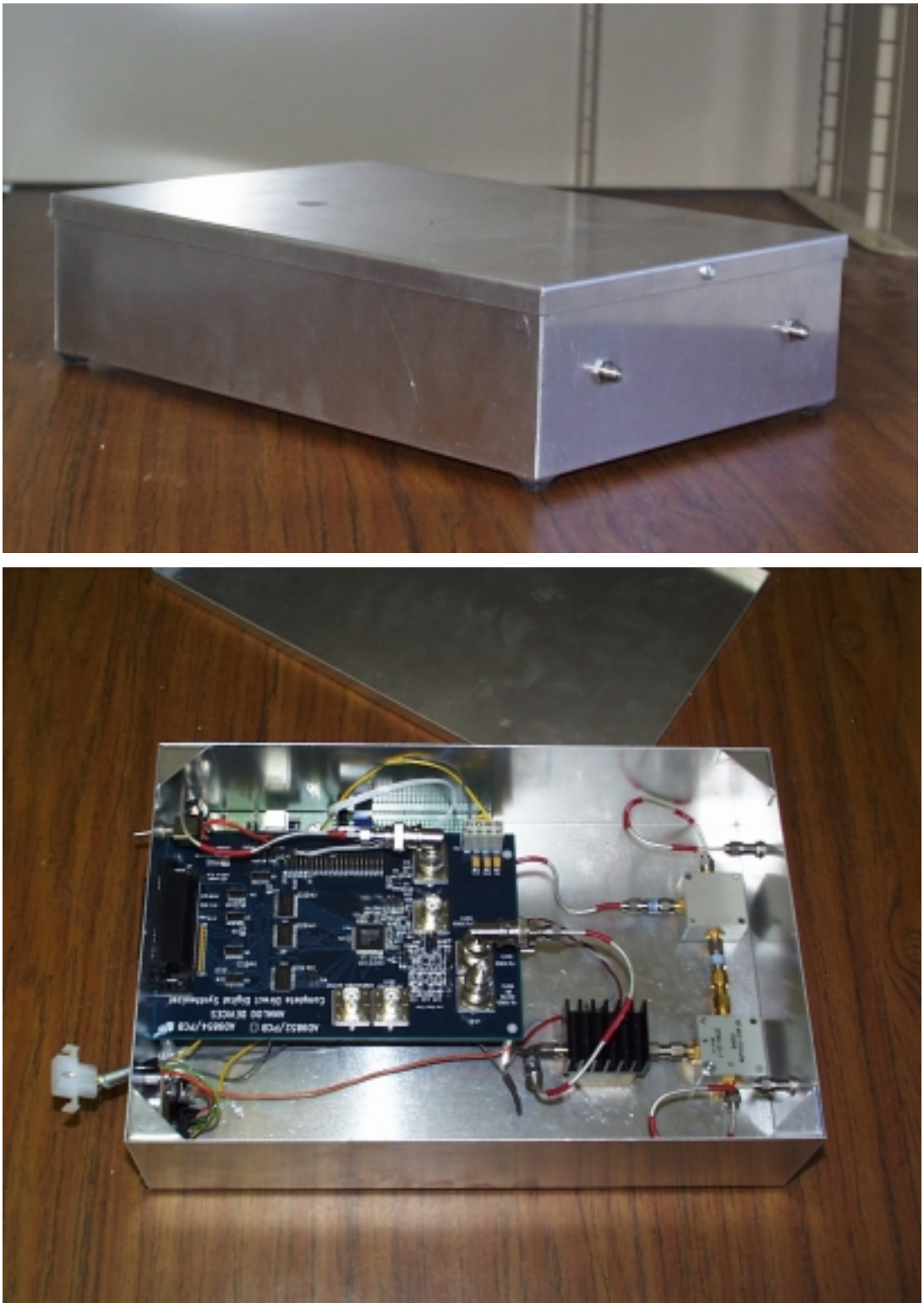

Figure 3-1. Radar system (excluding laptop, batteries, and antennas).

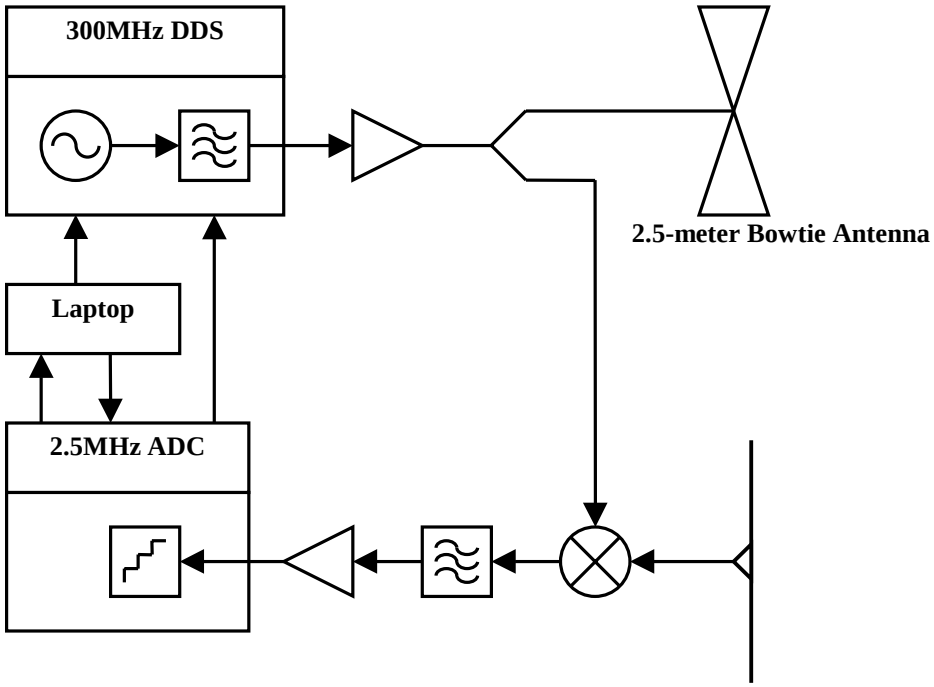

Figure 3-2. Radar system block diagram.

Table 3-1. System Specifications (Excluding Antennas, Batteries, and Laptop).

Modulation	Swept-FM, Stepped-FM, Pulsed
Frequency	1-120 MHz
Sweep Time (Pulse Width)	Adjustable
Compressed Pulse Width	Depends on bandwidth
Power Output	10 dBm
Power Consumption	< 3 Watts
ADC Resolution	16 bits
ADC Dynamic Range	96 dB
ADC Sampling Rate	2.5 MSPS
Size	7cm x 20cm x 30 cm
Weight	1.5 kg

3-2-1 TRANSMISSION LINE TESTS

Prior to testing the radar with the antenna subsystems, the radar system was evaluated using transmission lines and attenuators to determine characteristics such as dynamic range, sidelobe levels, loop sensitivity, and spurious signal contributions. Figure 3-3 shows the response of the first system with a 145 ns delay line and a 40 dB attenuator attached. Figure 3-4 shows the radar response of the second system from the same 145 ns delay line and 40 dB (solid line), 60 dB (dashed), and 80 dB (dotted) of attenuation. The transmission line contributed an extra 5 dB of loss. In all cases, a Hanning window was applied to the data prior to the Fourier transform.

Comparing the results of the two systems, the first system has slightly lower sidelobes and improved noise performance. The sidelobe structure in the first image more closely resembles that associated with a Hanning window. Figure 3-3 also shows a signal-to-noise ratio greater than 60 dB with a total attenuation of 45 dB. These results indicate a dynamic range of more than 60 dB and a loop sensitivity of more than 105 dB. Figure 3-4 shows similar results concerning dynamic range and loop sensitivity for all three levels of attenuation. Spurious signals can be seen in both figures at around 290 ns and 435 ns. These signals are most likely second and third harmonics produced by the system amplifier or possibly multiple reflections through the transmission line. These spurious signals are around 60 dB less than the main pulse and should not be too much of a problem.

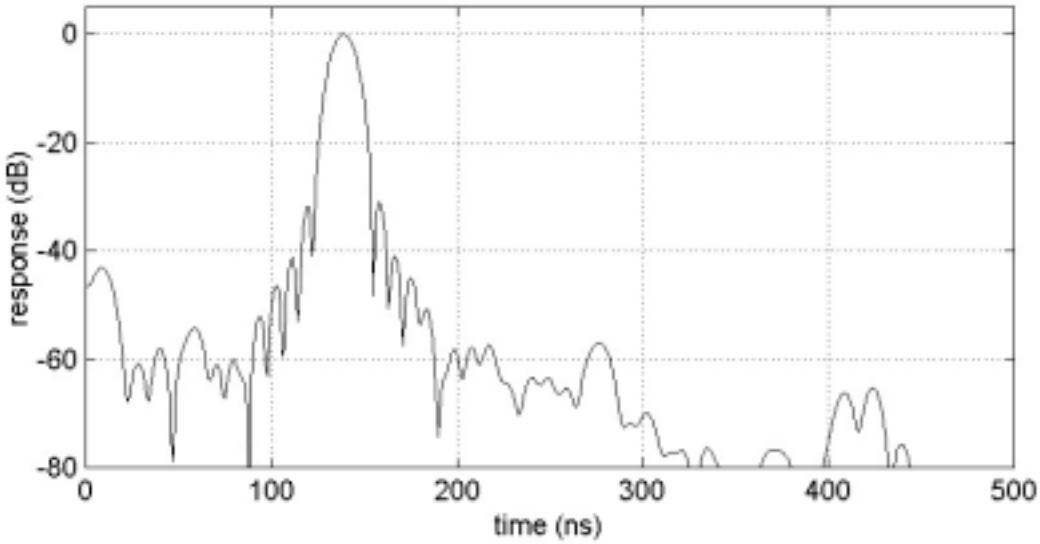

Figure 3-3. Transmission line results for the first system.

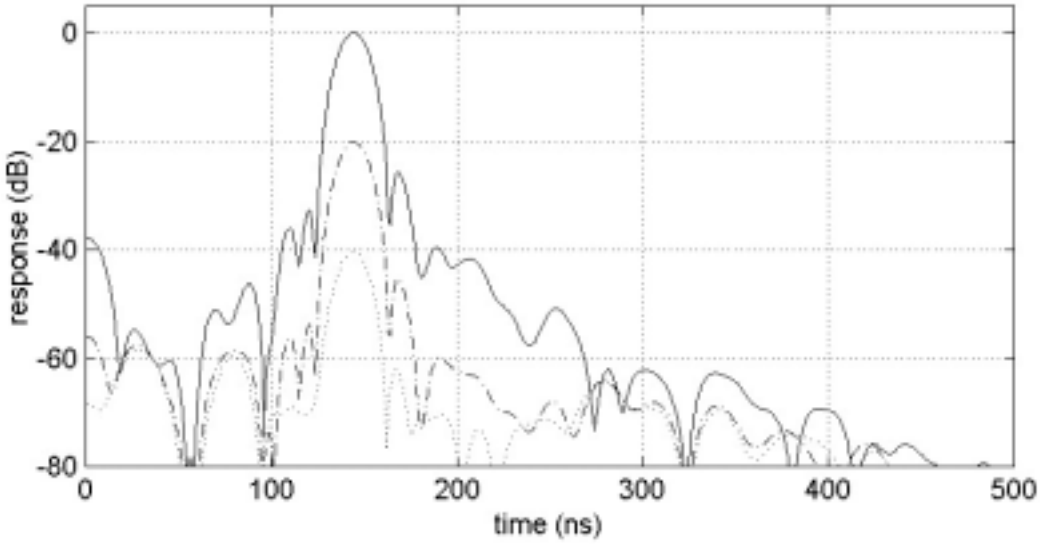

Figure 3-4. Transmission line results for the second system: (solid) 40 dB attenuation, (dashed) 60 dB, and (dotted) 80 dB.

3-3 ANTENNA SUBSYSTEMS

As with most surface-penetrating radars, there is a trade-off between range resolution and penetration depth [30]. This trade-off is largely due to the antenna subsystems and their limited bandwidths. To achieve the large bandwidths necessary for high resolution, proportionally high-frequency antennas are often used to cover the entire bandwidth. The higher frequencies suffer from increased attenuation from the soil and result in poor penetration depth. Alternatively, to get the desired depth penetration, lower frequencies must be used resulting in smaller bandwidths, and therefore, the resolution of the system is sacrificed.

Another problem is antenna size. Even if resolution is not a necessity, there still exists a limitation on the physical size of the antenna for a practical experiment, thus limiting the lower frequency and consequently the penetration depth. Electrically small antennas could be used, but they commonly exhibit a very large reactance, either capacitive or inductive depending on the type of antenna; a low radiation resistance; and a high quality-factor (Q-factor) resulting in a narrow bandwidth. Due to these characteristics, matching a small antenna over a broad frequency range is extremely difficult and resistive components may need to be used, which could drastically reduce the efficiency.

A surface-penetrating radar using resistively loaded dipole antennas typically has a relative bandwidth of about 40 %. To achieve reasonable penetration to detect ice on Mars, a 10 MHz center-frequency system may be needed, resulting in a 4 MHz bandwidth. The antenna size at 10 MHz would need to be around $\lambda/2$ or 15 m. The two-way resolution associated with the 4 MHz bandwidth in free space would be on the order of 40 m. In contrast, in order to achieve a resolution of 2 m, a 190 MHz center-frequency system would be needed. Looking at these numbers and the trade-offs shown in the previous two paragraphs, antenna design may be the most important

aspect of the radar system in order to achieve the depth penetration along with desired resolution. In the next few sections, the antenna design for both the transmitter and receiver of the radar system will be analyzed, starting with the effects of placing an antenna on a lossy ground.

3-3-1 ANTENNA ON A LOSSY GROUND

When an antenna is placed directly on the ground surface, a number of effects can be noticed. First, due to the dielectric loading of the ground, the frequency response of the antenna will be shifted down and the radiation resistance will decrease. This decrease of the resonant frequency will allow proportionally smaller antennas to be used for the same frequency range. Second, if the surface is lossy, the Q-factor of the system will be lowered and there will be an increase in bandwidth [31]. This is similar to resistive loading of an antenna. Finally, the dielectric half-space will alter the far-field radiation characteristics of the antenna, producing nulls along the air-ground interface and peaks at the critical angles within the ground [32]. These nulls along the air-ground interface will result in less coupling between transmit and receive antennas. All of these effects produce positive outcomes in terms of antenna matching, and radiation characteristics.

To show some of the effects described above, moment-method antenna simulations were conducted using dipole antennas. The first simulation considered a 0.5 m-long dipole with a wire radius of 1 mm in free space. The second simulation considered a dipole of the same wire radius/length ratio but with a 40 % size reduction in the presence of a lossy half space, $\varepsilon_r = 4 - j0.05$. Figure 3-5 shows a comparison of the reflection coefficient for both antennas. The dielectric ground effectively loaded the dipole in three ways. First, the real part of the ground permittivity made the antenna electrically longer, allowing for a shorter dipole

resonating at the same frequency. Second, the radiation resistance of the antenna was slightly lowered from 72 Ω producing a better match. Finally, the loss from the imaginary part of the ground permittivity resistively loaded the antenna, increasing the bandwidth.

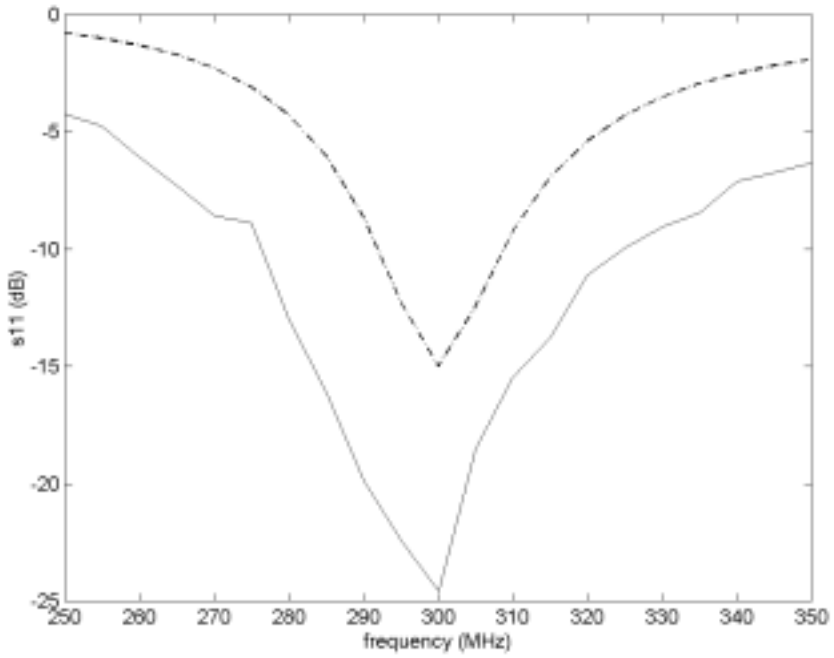

Figure 3-5. Comparison of the reflection coefficient for a .5-m dipole in free-space (dashed) and a .3 m dipole on a lossy dielectric half-space (solid).

3-3-2 BOWTIE ANTENNAS

For initial testing with the radar system, two bowtie antennas were constructed to operate over the frequency range 10 MHz to 120 MHz. Due to the large size required to radiate at the lower frequencies, the antennas needed to be collapsible for storage and transportation. An aluminum insect screen was used since it was lightweight, the fine mesh behaved as a solid conductor over the frequency range of interest, and it could be easily stored for transportation and deployed in the field. In free space, an antenna designed for a center frequency of 10 MHz would need to be 15 m in length. Assuming a 50 % reduction in length due to the dielectric loading of the ground, and a usable frequency range of at least 50 % below the resonant frequency due to ground loss, the required antenna size becomes 3.75 m. Due to the physical size of aluminum mesh that could be purchased, a final design was selected using two 1.3 m equilateral triangles supported by a PVC frame. Preliminary testing of the antennas over dry sand (ε_r=3.2) with a network analyzer and 4:1 transformer balun showed a 3 dB lower cutoff at about 20 MHz with a resistive impedance around 50 Ω at the input of the transformer balun (200 Ω input resistance for the antenna). Figure 3-6 shows the reflection coefficient of the antenna versus frequency with the circle at the 3 dB cutoff.

As a comparison, the same geometry was analyzed in free space using a moment-method simulator. The results for the measured and simulated data are shown in Figure 3-7. Both simulations show a rotating input impedance that seems to be converging toward real value; however, the input impedance for the experiment values is converging to a value close to 200 Ω [33], and the simulated data are converging toward 300 Ω. These discrepancies are likely due to testing the actual antennas over a dielectric half space, thus decreasing the radiation resistance and increasing the electrical length.

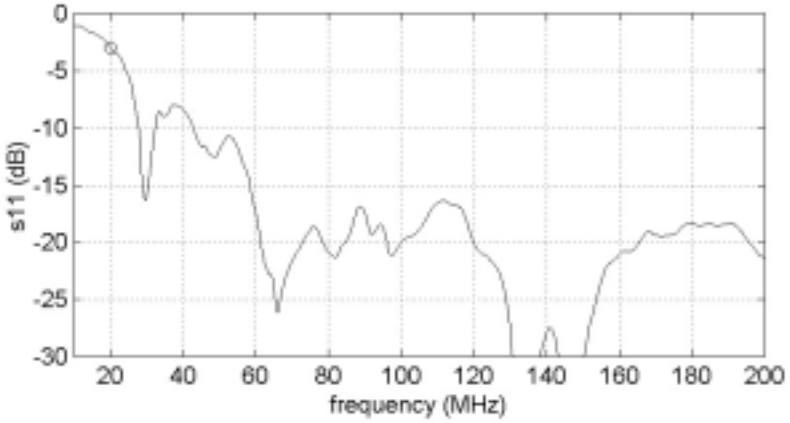

Figure 3-6. Reflection coefficient for 2.6 m bowtie over sand.

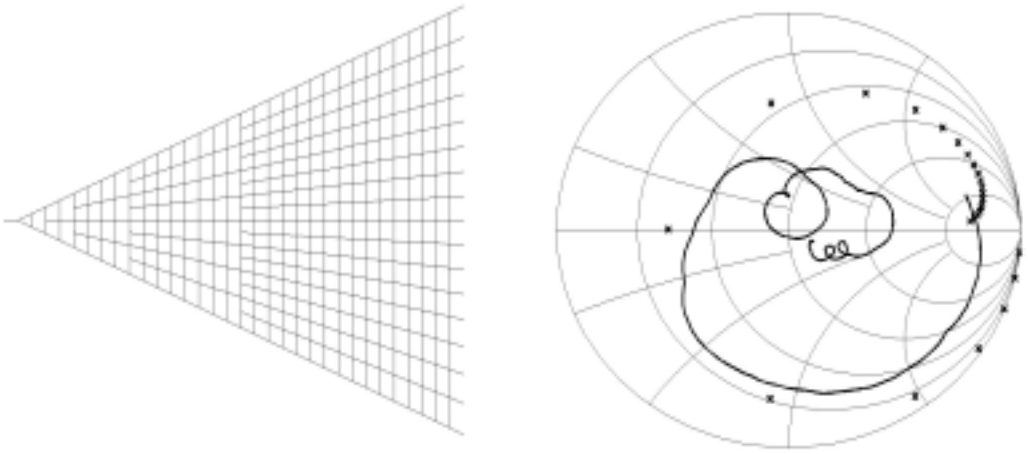

(a) (b)

Figure 3-7. (a) Bowtie antenna geometry (method-of-moments configuration). (b) Comparison of antenna impedance for both (solid) measured on sandy ground and (x) simulated. The impedances are referenced to 100 Ω on the Smith chart.

3-3-3 HIGH-IMPEDANCE RECEIVE ANTENNA

Traditionally, transmit and receive antennas of a surface-penetrating radar system are identical. Though reciprocity, if an antenna is a good radiator, it is also a good receiver. Thus, the same antenna used to transmit power into the subsurface can also be used to collect the reflected power. Also, since the antennas are the bandwidth limiting components of the system, it is beneficial to have them matched to achieve the highest power transfer. There is, however, a slight difference in the specific roles of transmit and receive antennas concerning power transfer. As stated before, the transmit antenna must radiate power efficiently into the ground, whereas the receive antenna should be effective in measuring the incident electric field. Measuring the electric field does not require efficient power transfer. Due to this difference, matching the receive antenna for maximum power transfer is not a concern as long as the electric field is being measured. Therefore, this characteristic is exploited to design a relatively small receive antenna that operates over a large frequency bandwidth.

The effective length is a parameter that is used to describe the radiating and receiving properties of an antenna [34]. For the radiating case, this quantity is equal to the total current-length product on the antenna relative to the current at the antenna feed. For the receiving case, this quantity is equal to the voltage induced upon the terminals when the antenna is open circuited. Furthermore, for the case of an electrically small dipole, the effective length is approximately equal to half of the physical length. More important, if the voltage induced upon the antenna terminals can be measured while the antenna is open circuited, an electrically small antenna could be used as the receive antenna. This can be accomplished using a high input-impedance, high-bandwidth, operational amplifier in the configuration as shown in Figure 3-8.

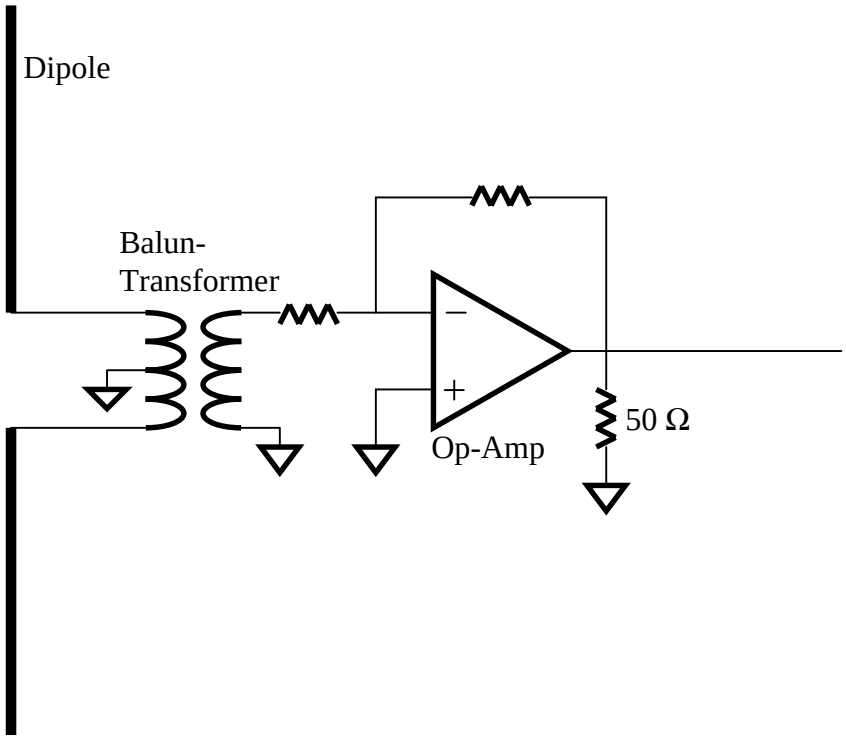

Figure 3-8. Receive antenna subsystem.

3-4 COMPLETED RADAR SYSTEM

Figure 3-9 shows the complete surface-penetrating radar. All the systems, including the transmitter, receiver, antennas, batteries, and laptop, are mounted on a wooden ski/sled that can be dragged as data are being collected. The bowtie antenna is located at the rear of the ski and is supported by a PVC frame. The transmitter is placed very close to the bowtie antenna to reduce any multiple reflections caused by the mismatch of the transmit antenna. The receive antenna is placed as far as possible on the ski from the bowtie to reduce the antenna feed-through signal. The choice of ski length is important when considering the amount of feed through that can be tolerated. A large ski would provide greater separation at the cost of a less mobile

system. For initial testing, an 2.7 m board was used. The transmitter/receiver box, laptop computer, and batteries are located between the antennas on the ski. The entire system is portable and requires no external power or control cables.

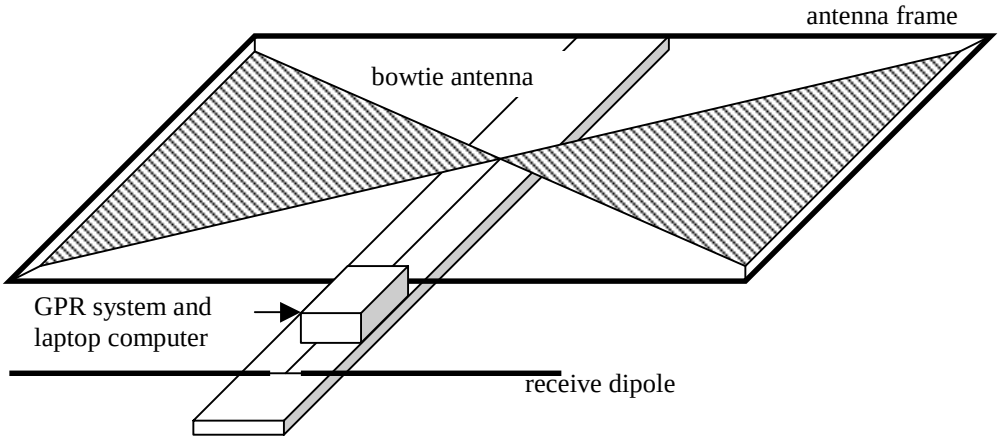

Figure 3-9. Complete surface-penetrating radar system.

CHAPTER 4

SIGNAL PROCESSING

4-1 INTRODUCTION

Using an Inverse Fast Fourier Transform (IFFT) algorithm, the IF beat signal of a Frequency-Modulated Continuous-Wave (FM-CW) radar can be converted into range profile in which range is proportional to the ratio of the beat frequency and sweep rate. A major disadvantage of FM-CW systems when compared to short-pulse "impulse"-type systems is the range sidelobes associated with this Fourier transform. These sidelobes can be theoretically reduced with windowing functions, such as the Hanning or Blackman windows [35], but this requires careful calibration of the system and applying a large amount of attenuation to the lower frequencies. System imperfections often cause sidelobe reduction to be smaller than that predicted by theory. Furthermore, in the case of surface-penetrating radar, the lower frequencies contain most of the information on deeper reflections and should not be deliberately

attenuated. The proposed signal-processing schemes attempt to achieve the improved sidelobe reduction compared to conventional windowing functions without attenuating the information bearing the lower frequencies.

A major requirement for a surface-penetrating radar is that it must detect a weak signal from a subsurface layer in close proximity to the strong signal from the surface. For example, if a weak dielectric interface exists in a lossy soil near the surface, the amplitude of the power reflected by the interface may be 40-60 dB or up to a million times less than that reflected by the surface as shown in Figure 4-1. This weaker reflection is often masked by the sidelobes of the larger reflection, even with windowing. The algorithm presented in this chapter attempts to eliminate the sidelobes associated with the stronger reflection and bring out the smaller reflections so they can be detected.

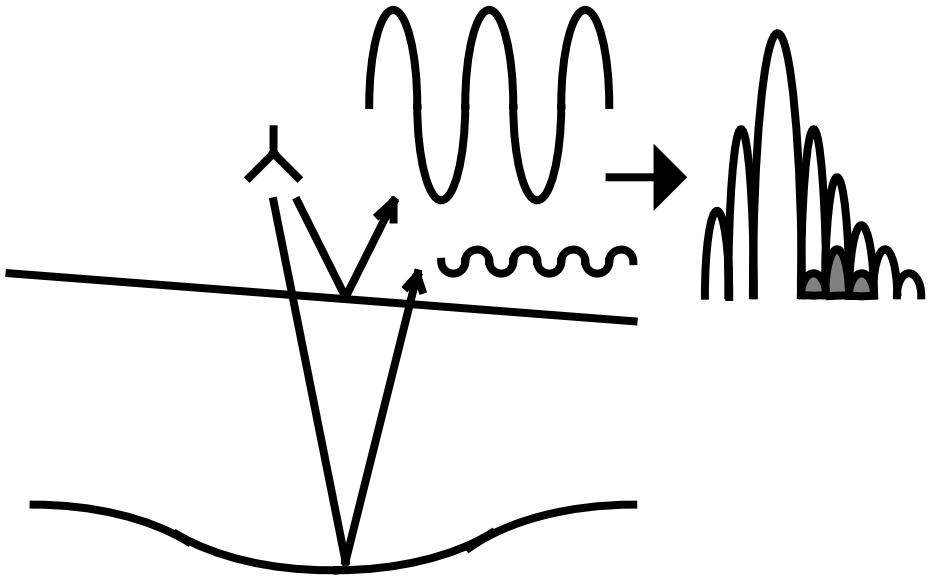

Figure 4-1. Typical configuration for a surface penetrating radar. The weak reflection from the subsurface layer (gray) is masked by the strong reflection.

4-2 SIGNAL DECOMPOSITION

The return signal of a surface-penetrating radar can be represented by the superposition of many reflections generated by electrical contrasts within the subsurface. Neglecting the coupling between the antennas and ground, this radar response can be expressed as the convolution of the reflection profile within the ground, $p(t)$, and the incident waveform, $s_t(t)$.

$$s_r(t) = \int p(\tau) \cdot s_t(t-\tau) d\tau = p(t) \otimes s_t(t) \qquad (4\text{-}1)$$

The goal of radar signal processing is to accurately determine this reflection profile from the measured response. If the incident waveform were an impulse (infinite bandwidth), this would be trivial; however, the incident waveform is bandlimited, and deconvolving it from the measured response to obtain the reflection profile is very difficult. This chapter investigates an iterative method of decomposing the measured response into a set of waveforms that each separately describes a reflection off a single interface, and collectively form the measured response. Furthermore, the characteristics of each component can be combined to obtain an approximation of the refection profile.

Consider a typical surface-penetrating radar response. The strongest reflection will likely be a combination of the surface reflection and antenna coupling. If the waveform of this reflection can be estimated from the total returned signal, an identical signal of opposite phase can be injected into the response and essentially eliminate the surface response including all the sidelobes associated with the waveform. The key to this method is that the sidelobes will be eliminated along with the main pulse. In fact, the degree to which the characteristics of the reflections can be estimated and modeled will indicate the amount of sidelobe reduction that can be achieved. Once the surface response has been eliminated from the total response, or at least significantly reduced, the next largest component can be detected, estimated,

and eliminated in a similar manner. Iteratively repeating this process while recording the amplitude and time delay of each component will both decompose the response and also give an approximation to the reflection profile.

4-2-1 DEVELOPMENT

Consider the signal generated from a single planar interface. The response, *S*, corresponding to a time delay, τ_0, for a chirp radar is represented as a sinusoidal signal with respect to the transmit frequency, f_T.

$$S_r(f_T) = A_0 \cos(2\pi f_T \tau_0 + \varphi_0) \tag{4-2}$$

For this simple case, only the amplitude, delay (or beat frequency), and phase need to be estimated. More specifically, the characteristics of the strongest component are estimated by computing the inverse Fourier transform and locating the maximum value,

$$[A_0, \tau_0, \varphi_0] = \max\left| \int_{f_1}^{f_2} S_r(f_T) \exp(j 2\pi f_T t) df_T \right|, \tag{4-3}$$

where f_1 and f_2 represent the lower and upper transmit frequencies of the system. A more realistic representation for the subsurface consists of the main signal and a summation of many other components from subsurface interfaces,

$$S_r(f_T) = A_0 \cos(2\pi f_T \tau_0 + \varphi_0) + \sum_{n>0} A_n \cos(2\pi f_T \tau_n + \varphi_n), \tag{4-4}$$

where $A_0 > A_n$. After the maximum value has been detected and the properties are recorded, a sinusoid of the same characteristics is subtracted from the signal, leaving only the summation of less significant components.

$$S_1(f_T) = S_r(f_T) - A_0 \cos(2\pi f_T \tau_0 + \varphi_0) = \sum_{n>0} A_n \cos(2\pi f_T \tau_n + \varphi_n) \quad (4\text{-}5)$$

Once this largest signal has been removed, the process can be repeated for the next largest and so on. This process is repeated until the maximum component is on the order of the dynamic range of the system. The original response can be reconstructed by combining all of the components and a leftover error term, S_e.

$$S_r(f_T) = \sum_n A_n \cos(2\pi f_T \tau_n + \varphi_n) + S_e(f_T) \quad (4\text{-}6)$$

The response shown by (4-6) can be rewritten in the time domain in the general form

$$s_r(t) = \sum_n A_n e^{j\varphi_n} s_t(t - \tau_n) + s_e(t) \quad (4\text{-}7)$$

where $u(t)$ is the sin(x)/x function associated with the finite bandwidth of the transmitted signal. Rewriting the time delay as a convolution with an impulse allows (4-7) to be expressed in a form similar to (4-1).

$$s_r(t) = \left[\sum_n A_n e^{j\varphi_n} \delta(t - \tau_n) \right] \otimes s_t(t) + s_e(t) \quad (4\text{-}8)$$

Equating (4-8) to (4-1) provides a means of estimating the reflection profile apart from a small error term, $s_e(t)$.

$$\hat{p}(t) = \sum_n A_n e^{j\varphi_n} \delta(t - \tau_n) \quad (4\text{-}9)$$

The hat is used to denote an estimated reflection profile. Finally, a reconstructed signal without sidelobes can be obtained by convolving the estimated reflection profile with an ideal waveform, such as a Gaussian signal.

4-2-2 EXPERIMENT ON A TRANSMISSION LINE

An initial experiment was conducted from data collected using a 145 ns transmission line. These are the same data used for the initial testing of the system in Chapter 3. Figure 4-2 shows the original data with no windowing and the corresponding time-domain representation. The time response exhibits the classic sin(x)/x waveform containing relatively high sidelobes that are associated with frequency-domain systems. Figure 4-3 shows the results after the first iteration. The top image shows the estimated signal as a dotted line and the decomposed signal in solid. After one iteration, the estimated reflection profile is an impulse with an amplitude and time delay corresponding to the largest component detected from the inverse Fourier transform. The bottom image shows the time responses. The dotted line is a reconstruction of the estimated signal, and the solid line is the inverse Fourier transform of the decomposed signal. Even after one iteration, the sidelobes have been decreased by about 20 dB, and a harmonic that was previously masked by the sidelobes is beginning to appear around 300 ns.

The results after 10 iterations are shown in Figure 4-4. The decomposed signal is shown in the top image and the time responses in the bottom. Again, a reconstruction of the estimated signal is shown by a dotted line and the decomposed signal is shown by a solid line. The sidelobes have been reduced to below 50 dB and the harmonic near 300 ns is more obvious. The results after 80 iterations are shown in Figure 4-5. The top image shows the ratio of the estimated peak versus the maximum value as the iterations progress. The bottom image shows the original spectrum with no windowing function (dashed), the spectrum using a Hanning window (solid), and a reconstruction of the spectrum using the approximated reflection profile (dotted). The reconstruction retains the higher resolution of the non-windowed spectrum and the sidelobe reduction of the Hanning window. Also, a third-order harmonic is detected at 435 ns.

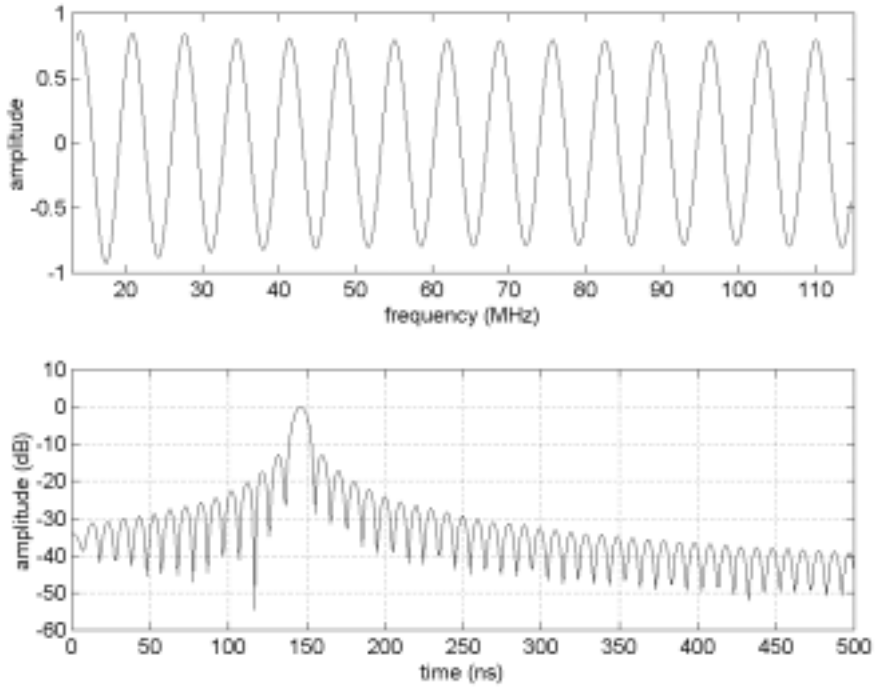

Figure 4-2. 145 ns transmission line (top) data and (bottom) spectrum without a windowing function.

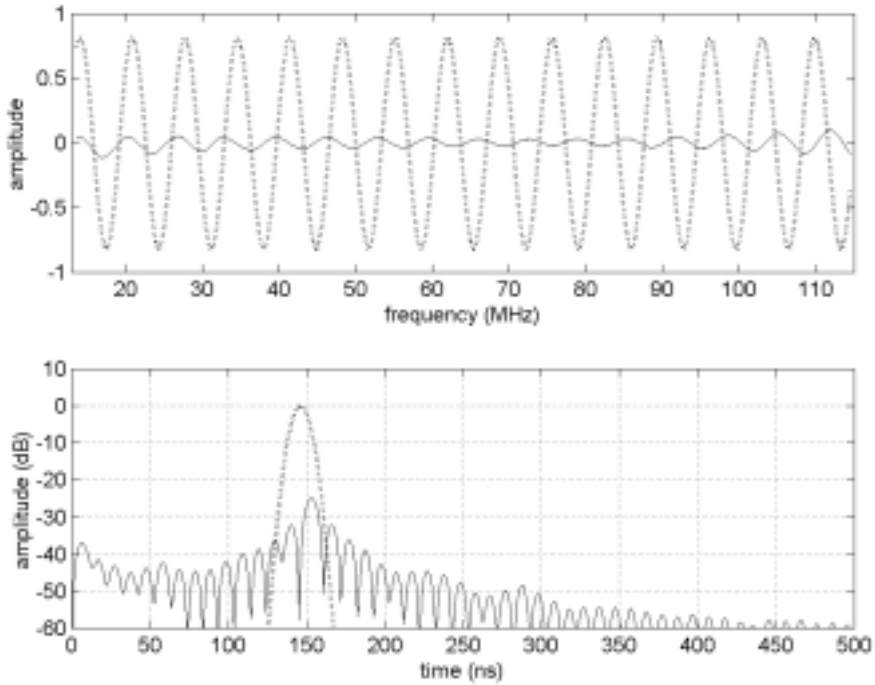

Figure 4-3. Signals after the first iteration: (dashed) estimated signal and (solid) decomposed signal.

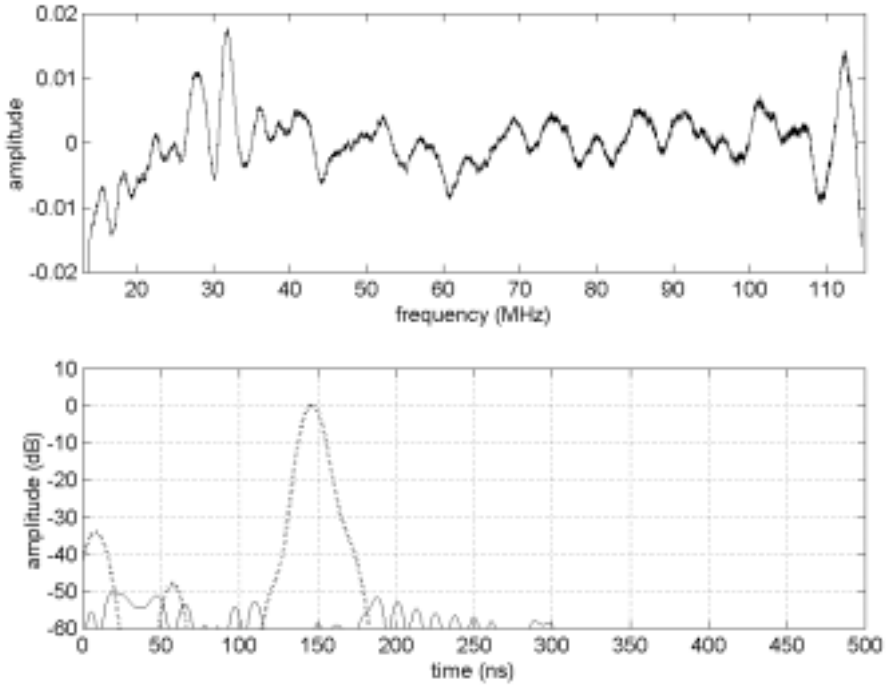

Figure 4-4. Signals after the 10 iterations.

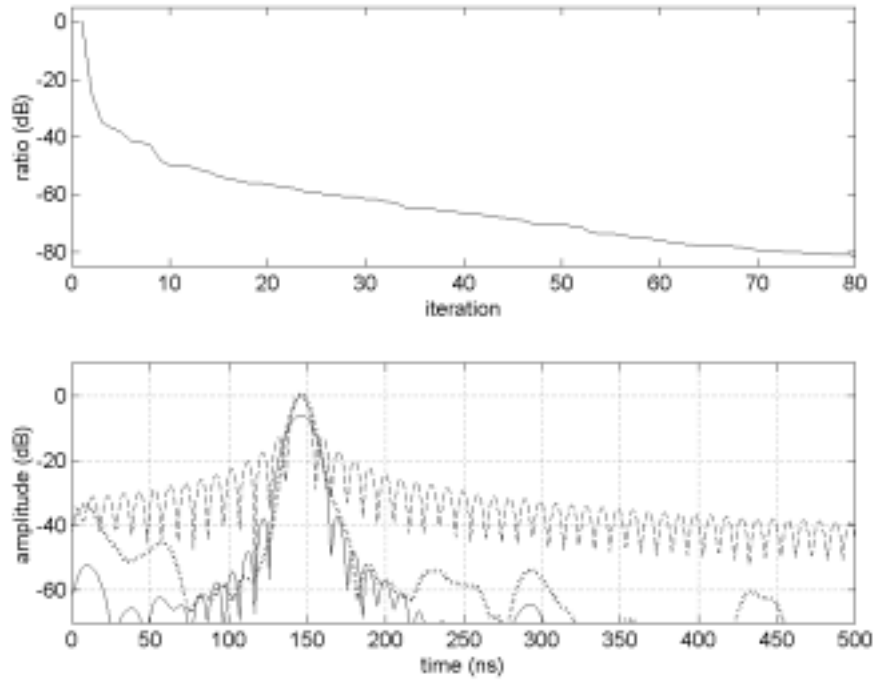

Figure 4-5. (Top) ratio of the magnitude of the decomposed signal after each iteration. (Bottom) 150 ns transmission line experiment. (Dashed) response with no windowing. (Solid) response with a Hanning window. (Dotted) decomposition processing scheme.

The 145 ns transmission line was an adequate model to test the decomposition process, but for the case of a surface-penetrating radar, reflections from deeper objects will not exhibit a constant amplitude over the entire frequency band. For this case, each component of the response is characterized as a function of many variables such as amplitude, frequency, phase, attenuation, and dispersion factors. Unfortunately, the sidelobe structure of the deeper reflections will be more difficult to replicate and cancel. The signal-processing scheme proposed in this chapter is composed of three basic steps: characterizing the response of the most significant reflection, generating a similar waveform, and subtracting it from the entire response. Of these, characterizing the response is the most important, and the extent to which the signal can be estimated will greatly impact the entire process. In general, the characteristics of the largest component are estimated using some type of operator, which in the previous model was simply finding the peak of the IFFT and assuming a constant frequency response. In the next section, the method will be extended to estimate the frequency content of each pulse, as would be needed for surface-penetrating radar data.

4-3 Interpreting Surface-Penetrating Radar Data

Figure 4-6 shows an example of a typical response from a surface-penetrating radar. The response contains a large surface reflection followed by smaller reflections from subsurface layers. The deeper reflections appear to be broad since the higher frequencies have been attenuated, thus reducing the bandwidth and lowering the center frequency. This is a common feature of surface-penetrating radar data and can be used to give an indication of factors such as soil loss and dispersion. In this section, the signal processing method described above will be used to decompose the signal into a collection of waveforms and determine the frequency characteristics of each of these waveforms.

The method is similar to what was described above with the addition of estimating waveform properties in the frequency domain. First, the most significant reflection is detected by finding the maximum in the time domain. A rectangular window is used to mask out all the other reflections, so the frequency characteristic of the individual pulse can be analyzed. In the previous section, this windowing function was essentially an impulse that sampled the peak value and is why the frequency spectrum of the estimated signal extended over the entire bandwidth. The size of the window is important because any interference from sidelobes of neighboring pulses must be minimized. If the window is too large, the estimated response will contain errors from other reflections, and if the window is too small, all the frequency information will not be captured. In general, the window should be large enough to capture a few cycles of the waveform. The windowed pulse is transformed into the frequency domain, and the center frequency and bandwidth are estimated from the mean and standard deviation of the spectrum. The center frequency and bandwidth are expressed as

$$f_c = \frac{\int f|S_w(f)|df}{\int |S_w(f)|df} \tag{4-10}$$

$$BW = \sqrt{\frac{\int f^2|S_w(f)| - df}{\int |S_w(f)|df} - f_c^{\,2}} \tag{4-11}$$

where $S_w(f)$ is the windowed spectrum. Once the center frequency and bandwidth have been evaluated, a replica signal can be generated, transformed back into the time domain, and subtracted from the total response. This process is repeated for the next largest reflection and so on. Figure 4-7 outlines the process.

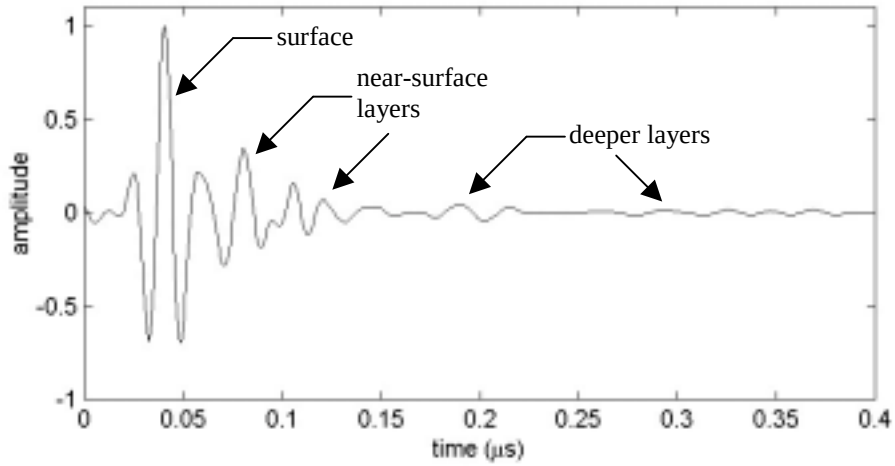

Figure 4-6. Typical surface-penetrating radar data.

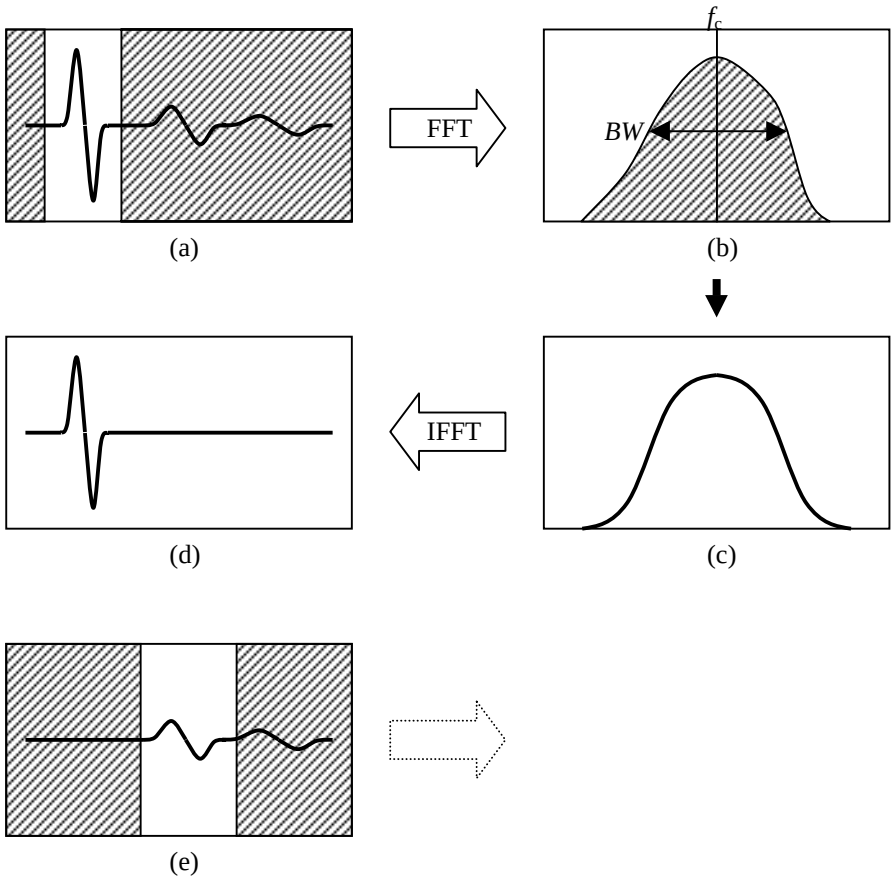

Figure 4-7. Data analysis procedure. (a) The most significant reflection is windowed. (b) Center frequency and bandwidth are estimated in the frequency domain. (c) Signal is generated, and (d) converted into time domain. (e) Signal is subtracted and the process is repeated.

4-3-1 EXAMPLE ON SPR DATA

As an example, the process is applied to the data in Figure 4-6. The first maximum value is detected as the surface response occurring at 40 ns. A 60 ns window, centered at 40 ns, was applied to the response and the FFT was calculated. After transforming to the frequency domain, the reflected pulse is shown to have a center frequency of 58 MHz and a 3 dB bandwidth of 33 MHz. Next, a signal of opposite phase is generated and the surface reflection is canceled. Figure 4-8 shows the original signal (dashed) and the approximation for the surface response (solid). For the next largest reflection at 80 ns, the center frequency is estimated to be 49 MHz with a bandwidth of 24 MHz. There is already a considerable drop in both the center frequency and bandwidth after only an 80 ns time delay. Figure 4-9 shows the decomposed signal (dashed) generated by subtracting the surface response from the original signal and the approximation of the reflected pulse occurring at 80 ns (solid). From the decomposed signal, the approximated waveform has effectively canceled most of the surface response, allowing the signal at 80 ns to be detected and analyzed.

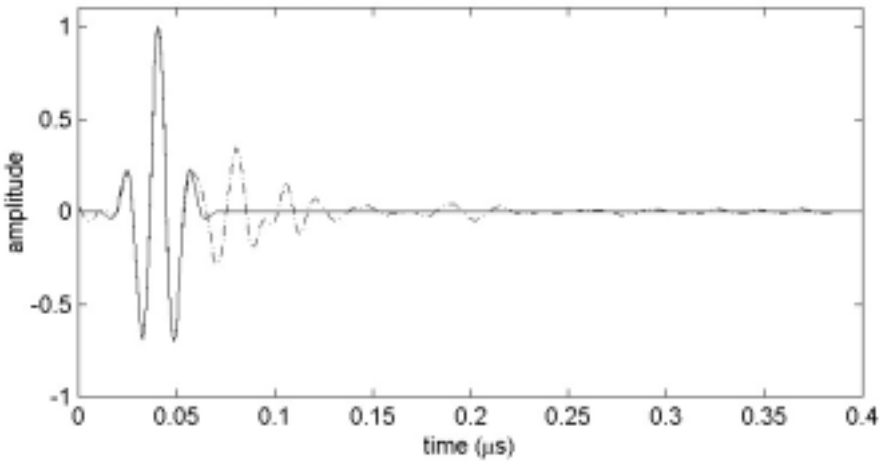

Figure 4-8. Original signal and the approximation of the surface response.

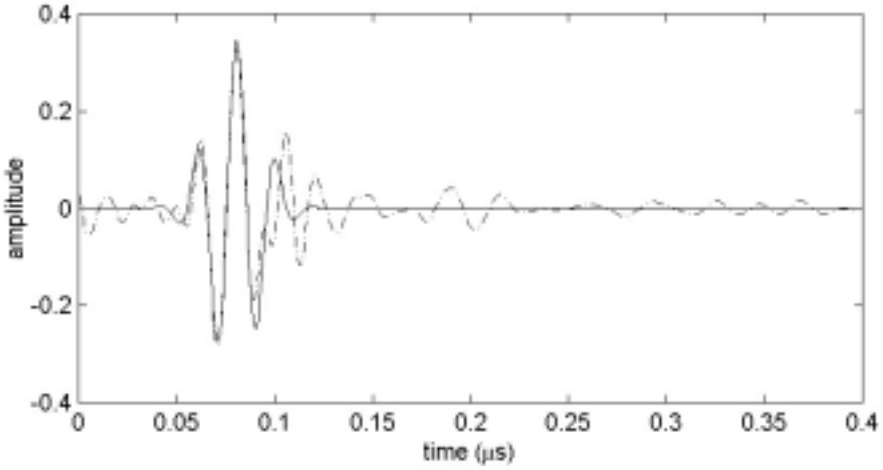

Figure 4-9. Original signal with the surface response removed (dashed), and the approximation for the next largest component (solid).

The third peak occurring at 100 ns has a higher center frequency of 66 MHz. The increased frequency of this reflection indicates that the signal may be due to a surface reflection such as a trees or other surface clutter. After a few more iterations, the maximum value occurs at 200 ns. The center frequency for this pulse is 39 MHz, less than 70 % of the incident pulse. The bandwidth is also reduced to 23 MHz, again much less than that of the surface. As with the reflection at 80 ns, this reflection is thought to be a result of a subsurface interface due to the reduced frequency content.

As mentioned earlier, the effectiveness of this algorithm relies on the degree to which a reflection can be estimated. For the first example, the response of each reflection was assumed to contain the same frequency content, that of the transmit waveform. For the second example, both the center frequency and bandwidth of each reflection was estimated by calculating the mean and standard deviation, or first and second moment, of the spectrum. Figure 4-10 shows a comparison of the two methods when applied to the waveform shown in Figure 4-6. Both results show the reduction of the peak signal versus iteration. The first method is shown by the solid line, and the second method is shown by the dashed line. A greater reduction is

shown for the second method, indicating each reflection has been more accurately estimated. The method could be further improved by estimating higher-order moments that would indicate properties such as any skew in the distribution.

Realizing that subsurface reflections will exhibit lower center frequencies and smaller bandwidths, the reflection profile can be filtered to contain only subsurface events by removing any reflections that contain frequency characteristics larger than that of the surface response. When applied to the reflection profile generated from the data in Figure 4-6, only eight reflections remain. Figure 4-11 shows the original pulse (dashed) along with an approximation of the response generated only with the components believed to occur from the subsurface. Table 4-1 lists these reflections along with their center frequencies and bandwidths.

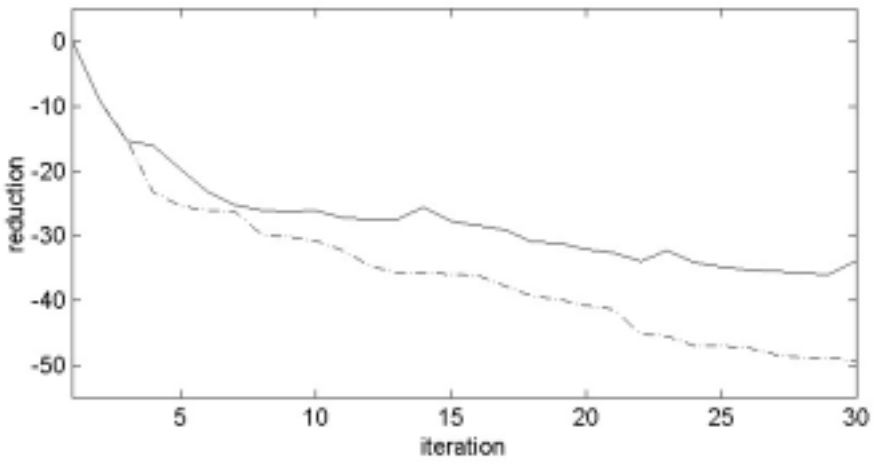

Figure 4-10. Comparison of the amount of signal reduction between the first method (solid) and the second method (dashed).

Table 4-1. Results of the SPR Response

iteration	time (ns)	amplitude	f_c (MHz)	BW (MHz)
1	40	1.000	58	33
2	80	0.345	49	24
3	101	0.174	67	33
6	132	0.050	47	28
7	197	0.049	39	23
13	322	0.016	43	24
14	290	0.016	35	28
16	368	0.016	41	23

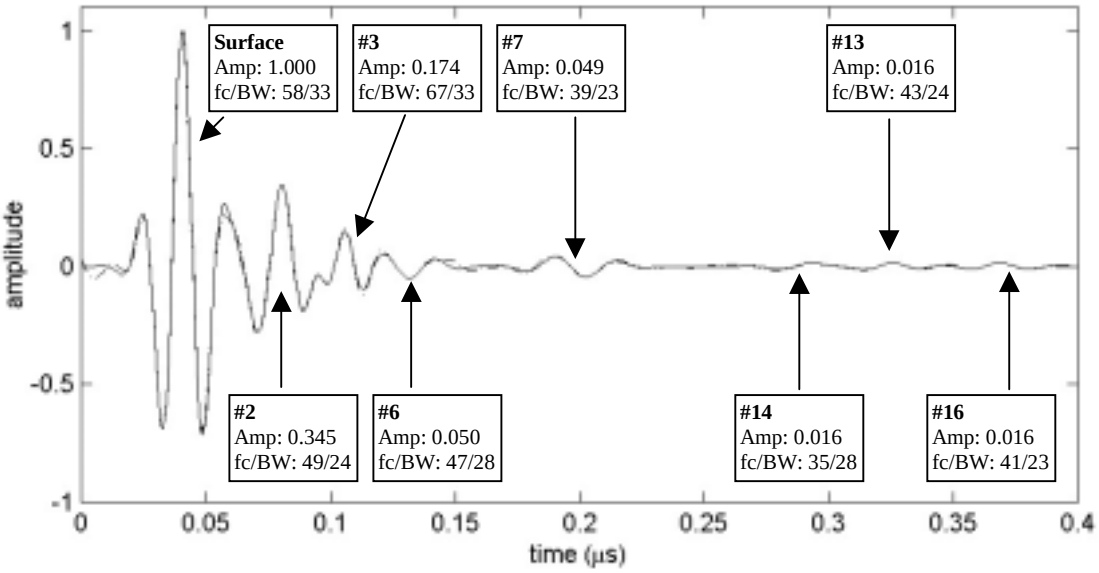

Figure 4-11. Comparison of the original data (dashed) and an approximation using the information in Table 4-1.

From these results a few conclusions can be made. First, from 40 ns to 200 ns there is a decrease in both the center frequency and bandwidth of the return signal. This decrease would imply a high-loss dielectric in the upper region. Second, from 200 ns on, there is little change in the frequency content, implying a relatively low-loss dielectric. As seen by the table, this method allows a means of quantifying the response of a SPR. Furthermore, it provides a means of interpreting the response from a single trace rather than relying on data collected across a lateral traverse. One additional benefit is that it allows the amount of memory required to save a trace to be drastically reduced. For this example, the 1024 data points have been reduced to an 8 x 5 matrix (the size of Table 4-1).

CHAPTER 5

RADAR EXPERIMENTS, SIMULATION COMPARISONS, AND SYSTEM MODIFICATIONS

5-1 INTRODUCTION

To asses the performance of the prototype system, measurements were collected over a few locations including one site in Lawrence, Kansas, and others near Fairbanks, Alaska. For most of these experiments, data were collected over stratigraphy that was, to some extent, already determined through seismic surveys, dilled cores, or other geological surveys. This information was extremely valuable in interpreting the data and, in a few cases, it was used to simulate radar responses for interpreting the measured data. This chapter begins with description of the preliminary experiment in Lawrence, Kansas. This experiment was intended to provide a basic check on the operation of the system. Next, the results from the experiments in Alaska are presented. For two of these experiments, simulated results are generated and compared with the experimental results to interpret the radar responses.

5-2 LAWRENCE, KANSAS

The first experiment was conducted outside Moore Hall (Kansas Geological Survey) in the west campus of The University of Kansas. The main goal of this experiment was to test the basic operation of the system and identify any problems that may be encountered during the future experiments in Alaska. The site was selected because, previous to the radar measurements, a seismic survey was conducted by the Kansas Geological Survey [36]. The corresponding stratigraphy and lithology inferred from these seismic measurements are displayed in Figure 5-1. The depth of each stratigraphical member can be estimated from the 6 m wavelength on the left of the image. This information can be correlated with the radar measurements for interpreting the measured data. The main layer of interest concerning the radar measurements was the limestone at about 5 m depth. This layer provided a target that was sufficiently deep so the reflection could be resolved from the surface response, and shallow enough to provide a strong backscattered signal.

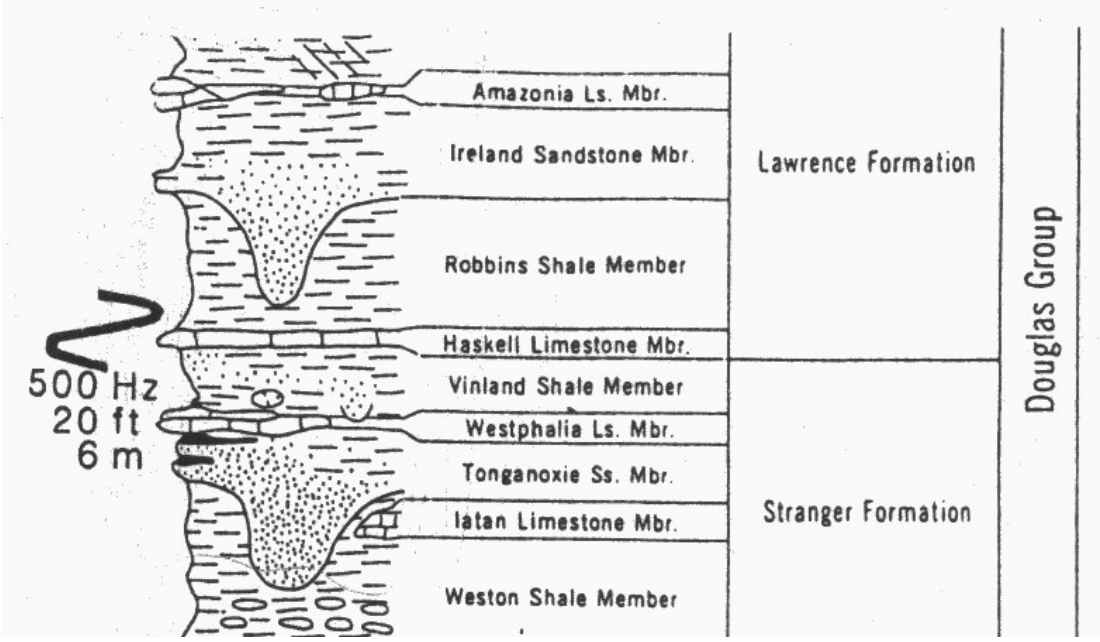

Figure 5-1. Stratigraphy and lithology for the west campus survey. The depth scale can be interpreted from the 6 m wavelength on the left.

The radar measurements were collected over a traverse of approximately 30 m with a sample interval of about 0.35 m between traces. For this experiment, the radar system had not yet been automated, requiring the user to trigger the system manually and save the data to disk for each trace. The raw data are displayed in Figure 5-2. Two important features can be noticed in the unprocessed data. First, there exists significant transmitted and received power over the entire frequency range of 5 MHz to 120 MHz. This indicates that both the bowtie and operation amplifier-dipole antenna subsystems are efficiently transmitting power and measuring the reflected field over more than four octaves of the frequency spectrum. Second, two external noise sources are detected at 91.5 MHz and 30.5 MHz, as shown by the red lines in the amplitude plot on the right of the figure. This external noise is attributed to a local FM radio station, KANU, at 91.5 MHz. The component at 30.5 MHz is a non-linear effect of the receive mixer. As the local oscillator drives the diodes of the mixer, all odd harmonics of the local oscillator are generated as the diodes are turned on and off. Furthermore, if the data are examined more closely, similar interference components will be seen at the other odd harmonics of 91.5 MHz including 18.3 MHz, 13 MHz, and so on.

A radar profile is generated from the raw data through a number of signal processing steps. As mentioned earlier, the time response is obtained by evaluating the beat frequency spectrum of the collected data via an inverse Fourier transform. Prior to transforming the data, the limits of the transform must be determined, and a windowing function is be applied to reduce sidelobe levels. Due to the radio interference, the limits of the transform were selected to range from 30.5 MHz to 91.5 MHz. Next, a Hanning window is applied and an IFFT is performed. A "dewow" filter [37] is used to remove any DC bias and bring out the higher frequency events. To help increase the signal-to-noise ratio a number of traces can be added coherently, but due to the relatively large separation between traces in this experiment, only a few

integrations could be tolerated before some of the more steeply dipping events were deteriorated. Finally, a gain function is applied to the data to amplify the deeper reflection that experienced more attenuation due to spherical spreading and other losses. The processing steps are listed below and the final image is shown in Figure 5-3.

Basic Signal Processing Steps

1. Choose FFT limits
2. Apply windowing function
3. Transform data
4. Differentiate/dewow/high pass filter
5. Average/stack/integrate
6. Apply gain

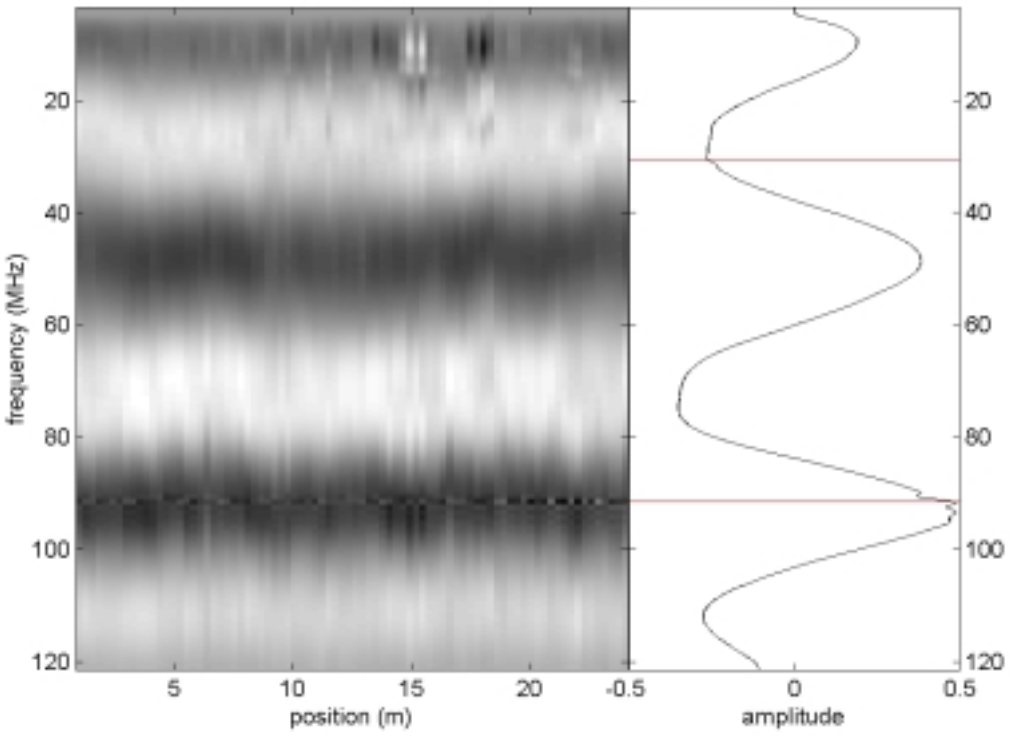

Figure 5-2. Collected data and amplitude plot. The red lines show where the radio interference occurs.

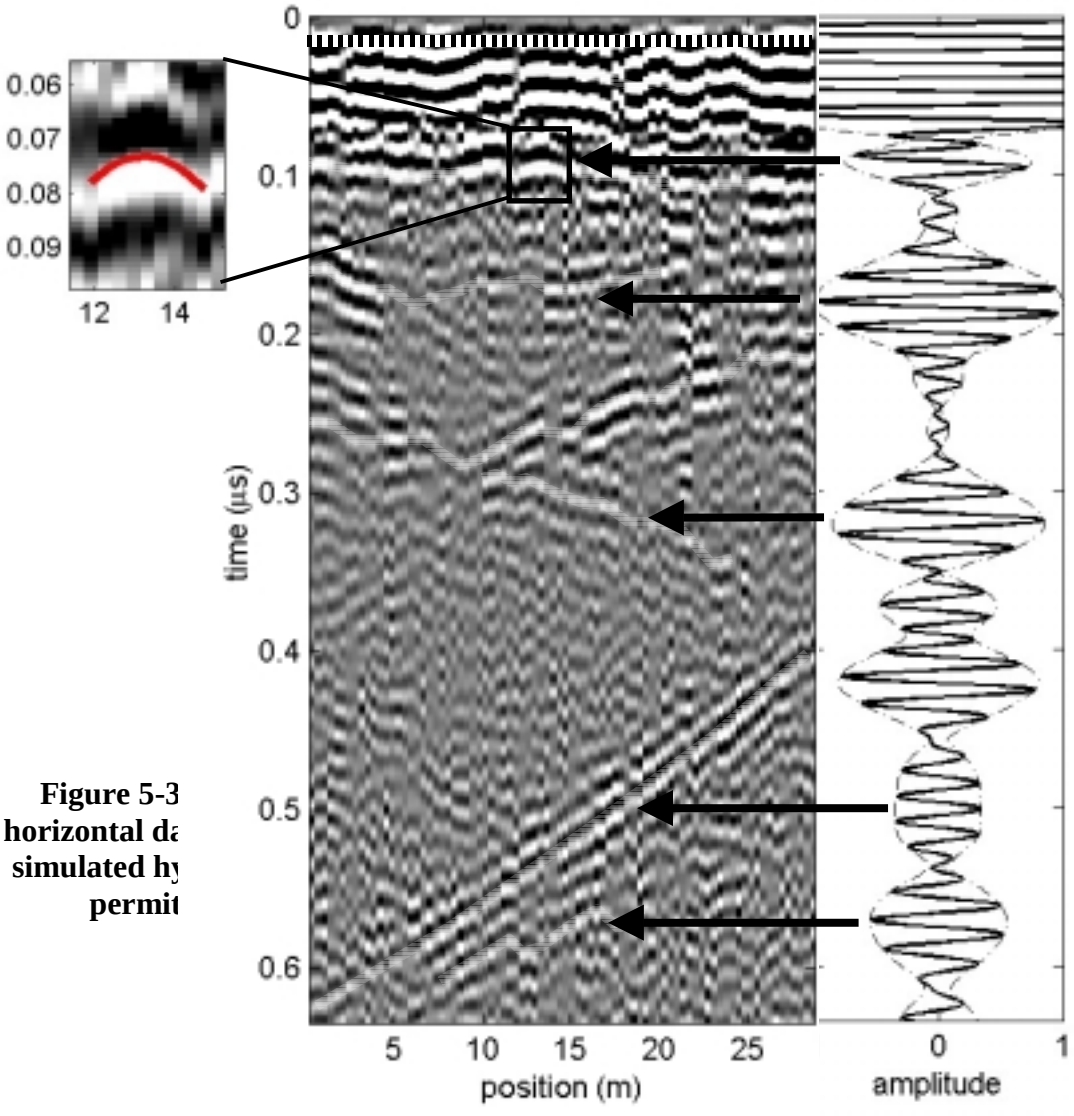

Figure 5-3
horizontal da
simulated hy
permit

From the processed image, a coherent reflection can be detected across the entire image at approximately 100 ns. Looking even closer, a hyperbolic event is located between 10 m and 15 m and is expanded at the far left of the image. Velocity analysis is used to estimate the dielectric constant and depth of this layer by assuming isotropic scattering off of a point target. The analysis places the reflection at a depth of about 5 m with a relative permittivity of around 4.5 to 5. These values agree well with the depth of the first limestone layer in the Figure 5-1 and the expected permittivity of the dry top soil.

5-3 ALASKA EXPERIMENTS

From August 19 to August 31 of 2001, experiments were conducted around Fairbanks, Alaska. The major goals of these experiments were to verify the performance of the system and to investigate the use of surface-penetrating radar to detect permafrost and also the presence of water or ice within permafrost. Unfortunately, due to the time of year, a significant amount of rain fell before and during the experiments. Due to the large amount of precipitation, the upper meter or so of the test sites was saturated with water. This upper saturated layer most likely decreased the backscattered power from deeper objects by a considerable amount due to the increased attenuation. However, this effect is most prominent at higher frequency and is not as significant at the longer wavelengths.

5-3-1 DELTA JUNCTION

Measurements were collected at two test sites in Delta Junction, a city about 100 miles west of Fairbanks. The stratigraphy of the first test site, as shown by Table 5-1, includes a 3 m layer of silt (eolian deposit) above an out-wash layer of gravel.

The layer of silt is broken down into a near-surface thaw layer with a thickness of approximately 0.5 m and a frozen layer of permafrost extending down to the gravel. Due to the high water saturation of the upper thaw layer, a dielectric of about 20 with relatively high loss is assumed, while the frozen silt will have a considerable smaller dielectric of around 6 and less attenuation. The stratigraphy of the second test site, as shown in Table 5-2, has only a thin layer, less than a meter, of silt above the gravel layer. It is also unlikely for the upper layer of silt to contain frozen soil.

The improvements in the data acquisition subsystem described in Chapter 3 had been made since the experiment in Kansas. The triggering and data storage were automated enabling a faster pulse repetition frequency and thus a finer sampling rate in the along-track direction. For the first test site, 1000 traces were collected at a spatial frequency of around 10 traces per m for a total length of 100 m. Looking at a single trace of the raw data, shown in Figure 5-4, a significant band of interference can be noticed between 10 MHz to 35 MHz. As a result, the limits of the Fourier transform were selected to extend from 35 MHz to 120 MHz. The processed images for both test sites are shown in Figure 5-5a and 5-5b.

Table 5-1. Stratigraphy of the First Test Site in Delta Junction

depth	Lithology	ϕ%	s%	fill
0.2	air	100	-	-
0.6	silt (eolian deposit)	30	70	water
1.4	silt (eolian deposit)	20	100	ice
-	gravel (out wash)	30	0	-

Table 5-2. Stratigraphy of the Second Test Site in Delta Junction

depth	Lithology	ϕ%	s%	fill
0.2	air	100	-	-
0.6	silt (eolian deposit)	30	30	water
-	gravel (out wash)	30	0	-

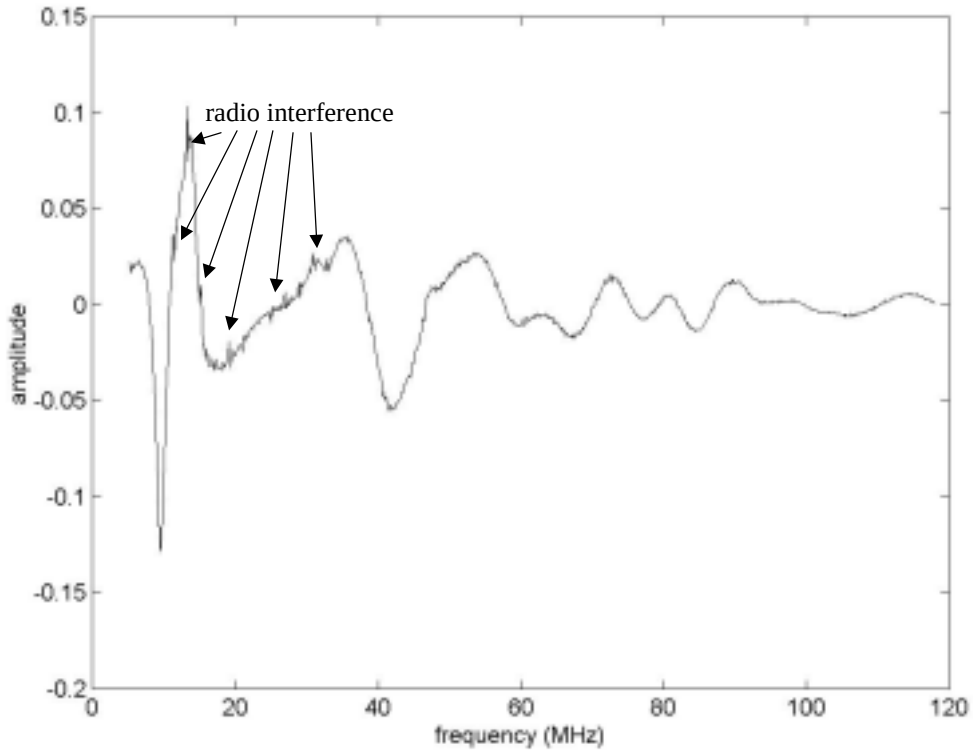

Figure 5-4. Raw data from traces collected at Delta Junction. Significant radio interference is seen ranging from 10 MHz to 35 MHz.

The reflections in Figure 5-5a indicate a somewhat continuous layer occurring along the entire image at 100 ns. Using Table 5-1 as a reference, it is probable that this reflection is a result of the silt-gravel interface occurring at a depth of about 3 m. Above this reflection there is a less continuous reflection that ranges from about 50 ns to 80 ns. Again referring to Table 5-1, this reflection is possibly a result of the transition between the active thaw layer and the more permanent frozen layer of the near-surface eolian silt deposit. The depth fluctuations are probably due to varying degree of sunlight incident upon different areas along the traverse. Other features in the image include a discontinuity of the silt-gravel interface from 40 m to 60 m and hyperbolic events around 90 m along track. Compared to Figure 5-5a, the results from the second test site in Figure 5-5b do not exhibit any noticeable layering. This result is likely due to a relatively thin layer of eolian deposit and the absence of the active thaw, frozen layer interface.

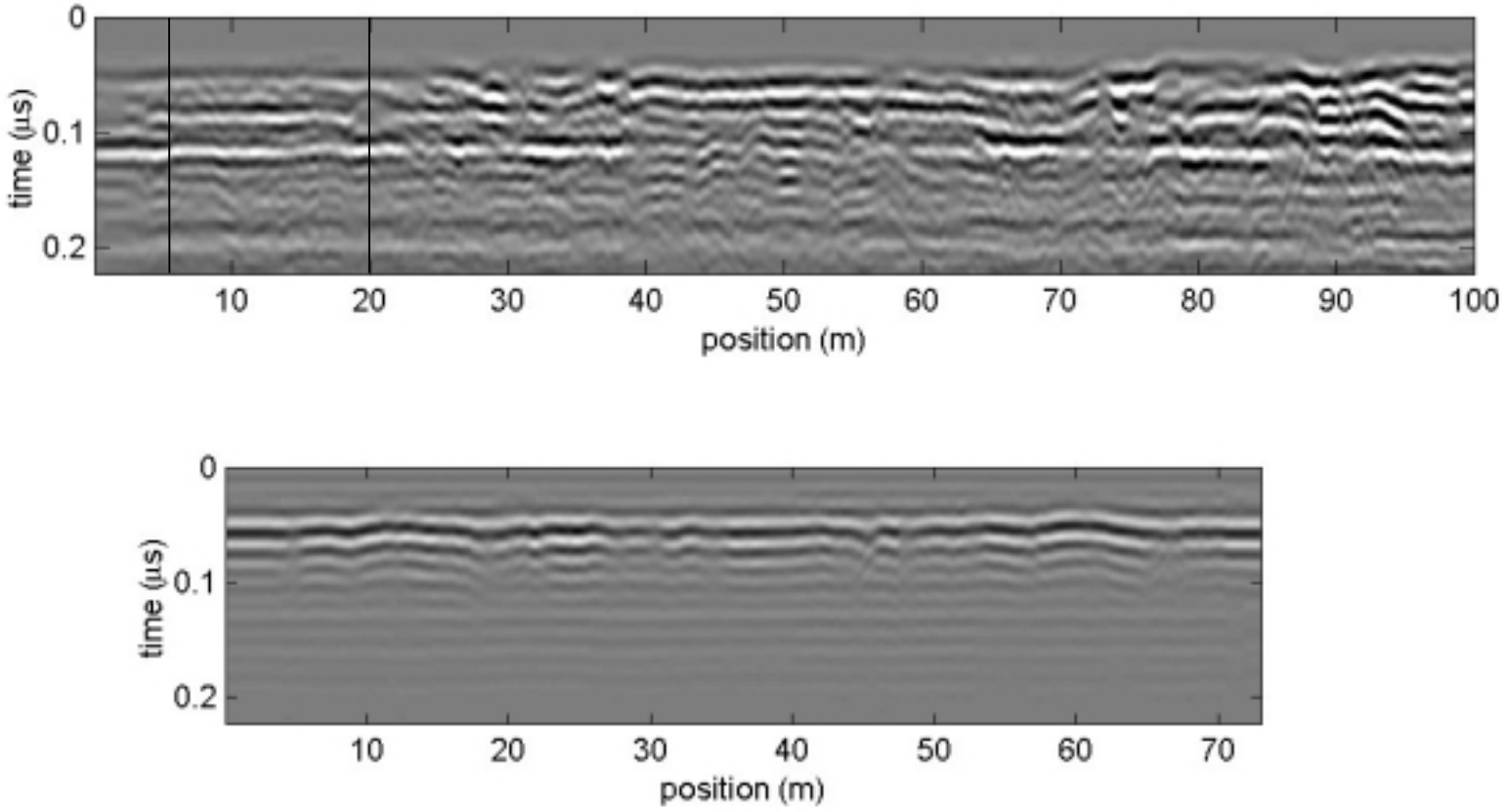

Figure 5-5. Processed images for site 1 (a) and site 2 (b) in Delta Junction.

5-3-1-1 INTERPRETATIONS USING SIMULATED RESPONSES

To help identify the subsurface layering and reinforce the interpretations mentioned above, simulated radar responses were generated using a stratigraphy similar to that described by Table 5-1. The simulated responses are used as a comparison for the collected data. The finite-difference time-domain [38] (FDTD) method was preferred as the simulator for a number of reasons. First, due to the proximity of the radar system to the surface and subsurface layering, spherical propagation will need to be considered, and therefore, a two- or three-dimensional simulator should be used. Second, the FDTD method is able to account for the radiation pattern of an antenna placed over a layered-dielectric half space, more specifically the half-moon-shaped pattern [32] as shown in Figure 5-6.

The amount of computation time required to simulate the radar response of the chirp signal using FDTD would be extremely large, and, therefore, it was more reasonable to simulate the response of an "impulse"-type system. The response of a frequency-modulated system can still be obtained simply by performing the pulse compression prior to the simulation rather that after. This is done by considering the radar response due to an ideal delay line, performing the pulse compression, and using the output as the incident pulse for the simulator. By generating the pulse in this manner, the sidelobes associated with a frequency domain system will be included in the simulation.

The FDTD mesh contains all the spatial information for the simulation such as the physical dimensions, boundary locations, and electrical values. For this simulation, the mesh is a 200-by-200 cell, two-dimensional grid with a cell size of 8 cm by 8 cm. The ground extends from cells 101 to 200 and is divided into three layers with initial permittivities of 20, 8 and 5, corresponding to the thawed eolian deposit, frozen eolian deposit and gravel out-flow layers, respectively. The initial losses of the eolian deposits which are 0.015 for the thaw layer and 0.002 for the frozen layer. The location of the

transmitter and receiver are indicated in the figure by diamonds and are positioned at (99,105) and (99,130).

Two responses were generated for the case of a three-layer model containing an active-thaw silt layer, a frozen silt layer, and an out-flow gravel layer. For both simulations the silt-gravel interface was at a depth of around 3 m, and locations for the thaw-frozen silt interface were varied to match the data. The simulations are intended to represent two possible cases that correspond to the data at the 6 m and 20 m positions indicated by the vertical lines on Figure 5-5a. The depth of the intermediate freeze-thaw interface can easily be detected at the first position of 6 m; however, this layer seems to disappear around 20 m. For each simulation, the values of the electrical properties and depth to the interface are iterated to obtain a better match to the actual data. The results of the first simulation are shown in Figure 5-7 along with the actual data. The resulting permittivities and loss factors are shown in Table 5-3. There is a very close match with the incident pulse reinforcing the likelihood for the freeze-thaw interface. The disagreement of the results at greater time delays is most likely caused by an incorrect assumption that only three layers with discrete permittivity changes are present. The results and values for the second simulation are shown in Figure 5-8 and Table 5-4.

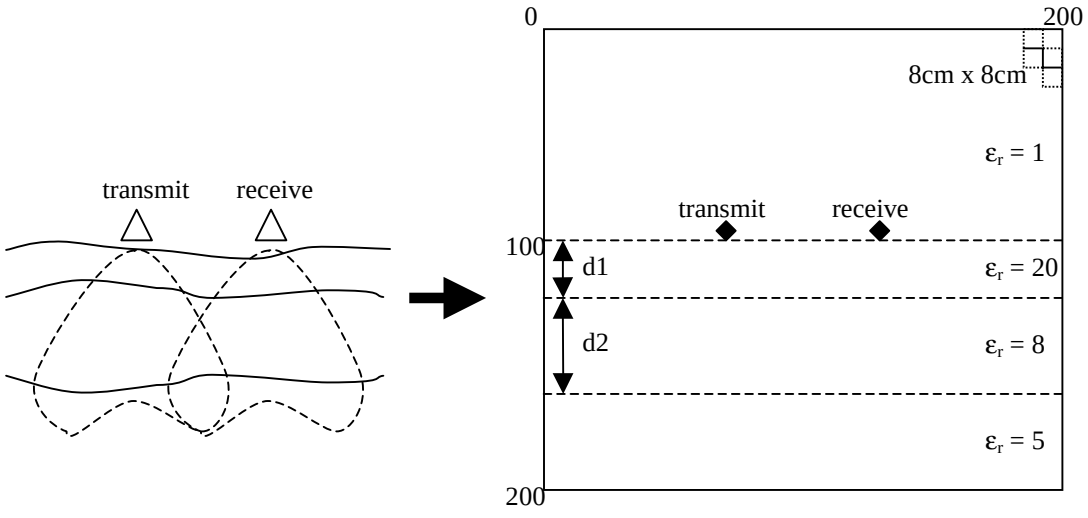

Figure 5-6. Real configuration and FDTD grid. The real configuration shows the expected radiation pattern (dashed line) of a dipole over a dielectric half space.

The simulation results seem to indicate that the freeze-thaw interface is closer to the surface at the 20 m position than at the 6 m position. This information could not be directly concluded from the image alone since this layer could not be adequately resolved from the antenna coupling and surface response. Instead, by replicating the near-surface interference pattern using FDTD, the layering could be identified. Furthermore, this layer is most likely continuous across the entire traverse, but due to varying degrees of depth and permittivity contrast it is not as noticeable as the silt-gravel interface.

Table 5-3. Estimated Depth and Electrical Properties at the 6 m Position

depth	Lithology	ε_r	loss
0.2	air	1	-
1.2	silt (eolian deposit)	18	0.02
2	silt (eolian deposit)	9	0.001
-	gravel (out wash)	3	-

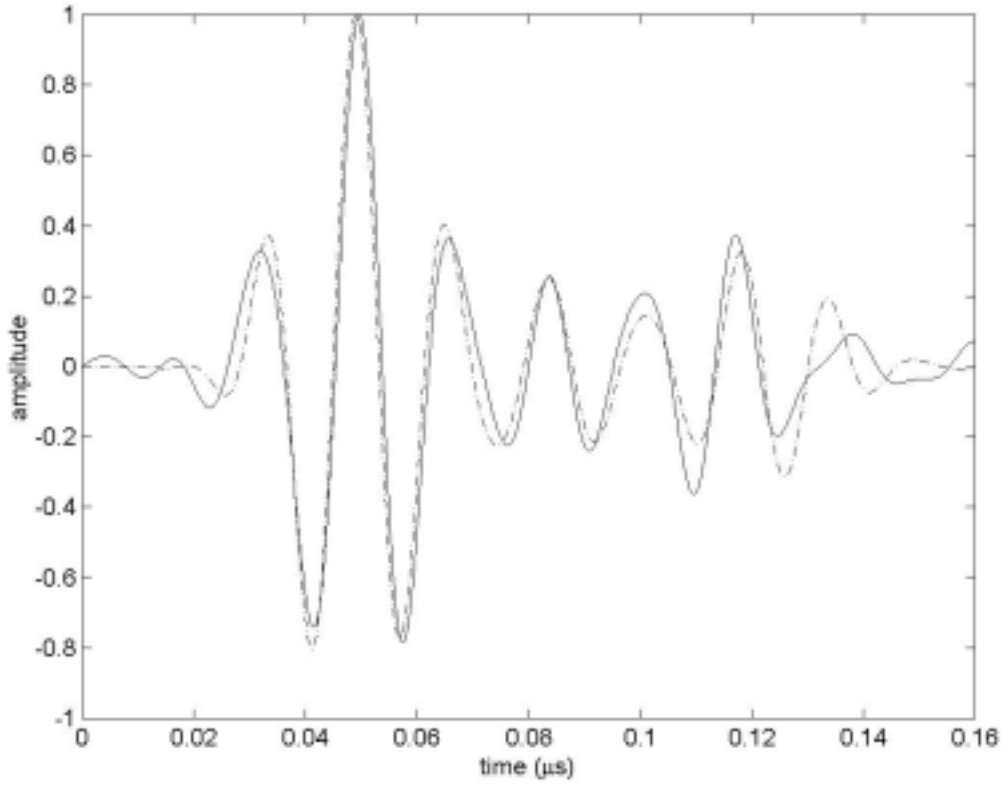

Figure 5-7. Comparison of actual and simulated responses at the 6 m position.

Table 5-4. Estimated Depth and Electrical Properties at the 20 m Position

depth	Lithology	ε_r	loss
0.2	air	1	-
0.5	silt (eolian deposit)	18	0.02
2.4	silt (eolian deposit)	9	0.001
-	gravel (out wash)	3	-

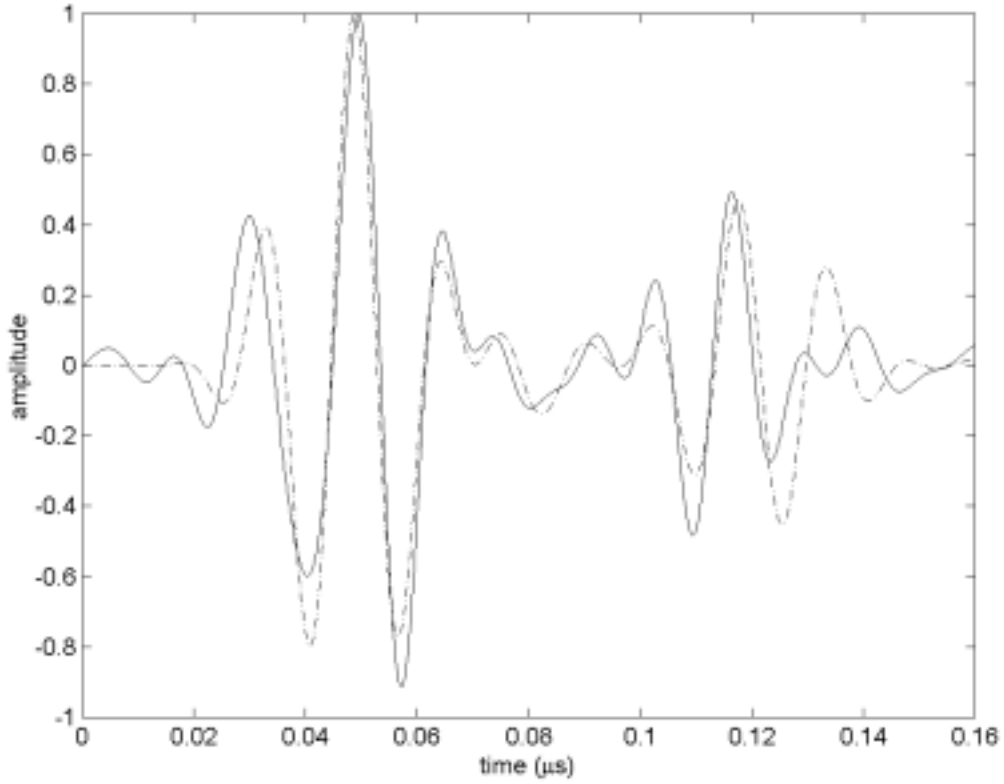

Figure 5-8. Comparison of actual and simulated responses at the 20 m position.

5-3-2 PINGO SITES

To investigate the use of radar to detect subsurface deposits of ice, an experiment was conducted at two pingo sites. As shown in Figure 5-9, a pingo is a subsurface ice lens that has formed through an upward flow of water from an underground source. Before the water can reach the surface it freezes, forming a lens of relatively pure ice.

This upward flow of water and subsequent freezing elevates the surface and produces a small hill. Due to this elevation, it is fairly easy to locate a pingo by looking for a group of trees that appear to be higher than their surroundings.

The area on and surrounding the first pingo site was dense with vegetation and there were many trees. Due to the large amount of trees and plants, access to the location was difficult and collecting data over a traverse was practically impossible. As a result, data collection was restricted to a few discrete locations often separated by a meter or more. In addition to the radar measurements, a core had been drilled at the peak of the site to provide addition information concerning the structure of the subsurface. This information will prove to be valuable in interpreting the responses collected by the radar system. Using data from the core measurements, the stratigraphy and lithology of the first pingo are shown by Figure 5-9 and listed in Table 5-5.

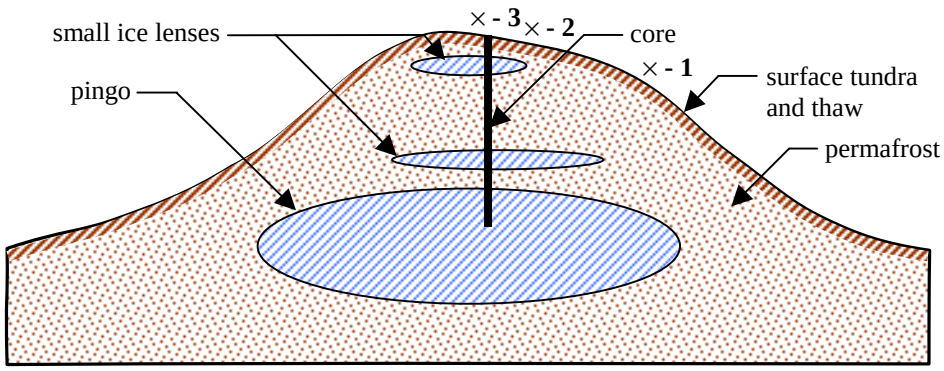

Figure 5-9. Subsurface structure of a pingo. The three Xs indicate the approximate locations where measurements were collected.

Table 5-5. Pingo Stratigraphy and Lithology

depth	Lithology	ϕ%	s%	fill
0.2	air	100	0	-
0.3	tundra	50	70	water
0.5	soil, eolian deposit	40	70	water
1.0	soil	30	90	ice
0.5	ice	100	100	ice
4.0	soil	30	90	ice
0.5	ice	100	100	ice
0.5	soil	25	90	ice
?	ice (main pingo ice)	100	100	ice

With the Delta Junction sites, FDTD simulations were used to find a match for the measurements and aid in data analysis. The thickness and electrical properties of the two upper layers were iterated, and, when a match was found between the simulated and measured responses, an interpretation of the subsurface could be made. For the pingo site, iterating over the 9 or more layers is impractical and time consuming. As an alternative, reflection profiles are calculated directly from the data and the simulated waveforms are generated using the iterative process described in Chapter 4. From the reflection profiles, possible locations of the ice lens are interpreted.

A comparison of the first radar measurement and simulated response is shown in Figure 5-10. The corresponding reflection profile is listed in Table 5-6. The results for the second and third measurements are given by Figure 5-11, Figure 5-12, Table 5-7, and Table 5-8, respectively. Possible internal reflections are chosen from the reflection profiles by evaluating the time, amplitude, and frequency content of each reflection. In general, a reflection from a deeper interface will show increased attenuation and lower frequency content. The far-right column of Table 5-6 illustrates this behavior. The center frequency of the reflected pulse decreases with increasing time delay. Reflections that appear to contain reasonable amplitude, time delay, and center frequency are selected as subsurface reflections. These reflections are listed in bold type in each table. The other waveforms are most likely errors from the decomposition process, multiple reflections, system artifacts, or reflections from trees and other sources of clutter.

Two of the reflections listed in the tables seem to indicate the top and bottom of the pingo. The first is around 150 to 160 ns and has an amplitude of about 0.05 compared to the surface response. The second is around 280 to 290 ns and has an amplitude of about 0.04. With an average dielectric of 8, these reflections would relate to a range of around 8 m and 15 m, respectively, along the same scale as recorded from the core measurements for the top of the pingo. The fact that the amplitude of the second reflection is close to that of the first would indicate a relatively low-loss dielectric for the layer between the reflections. This also agrees well with the dielectric properties of pure ice.

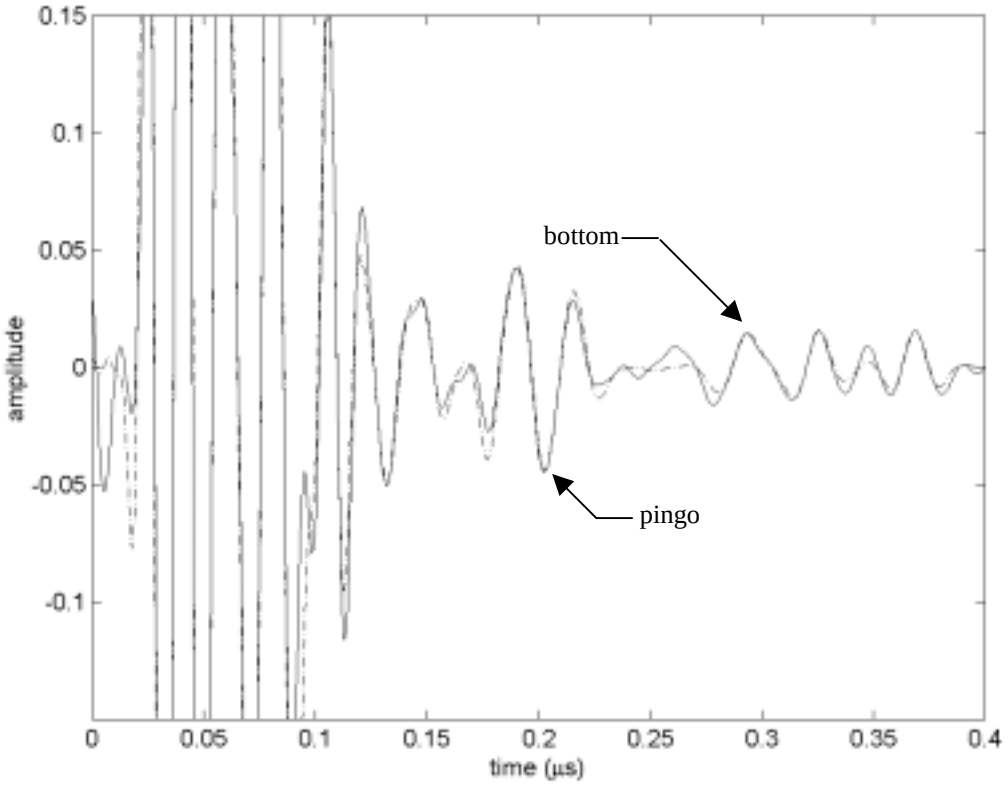

Figure 5-10. Measured and simulated data at the first location.

Table 5-6. Reflection Profile for the First Location

time (μs)	Amplitude	frequency (MHz)
0.0259	0.0563	65
0.0407	**1.0000**	**57**
0.0621	0.0873	42
0.0799	**0.3459**	**47**
0.0910	0.0116	39
0.1053	0.1568	66
0.1317	**0.0505**	**42**
0.1526	0.0267	39
0.1780	0.0163	37
0.1973	**0.0491**	**37**
0.2192	0.0161	36
0.2894	**0.0161**	**31**
0.3225	**0.0163**	**39**
0.3682	0.0157	42

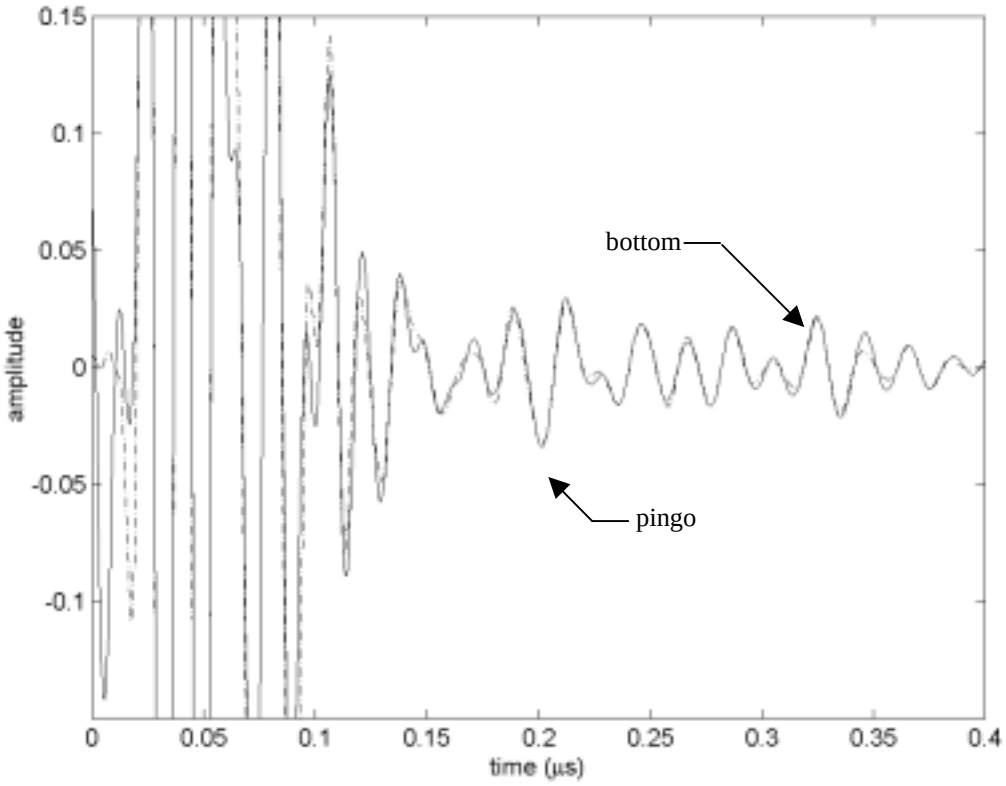

Figure 5-11. Measured and simulated data at the second location.

Table 5-7. Reflection Profile for the Second Location

time (μs)	Amplitude	frequency (MHz)
0.0001	0.0075	6
0.0259	0.1275	62
0.0407	**1.0000**	**59**
0.0549	0.0885	34
0.0631	0.0247	30
0.0788	**0.3334**	**54**
0.0916	0.0238	34
0.1073	0.1277	70
0.1322	**0.0576**	**43**
0.1541	0.0227	34
0.1851	0.0120	56
0.2055	**0.0375**	**41**
0.2411	0.0202	42
0.2823	**0.0187**	**48**
0.3298	**0.0100**	**45**
0.3682	0.0157	42

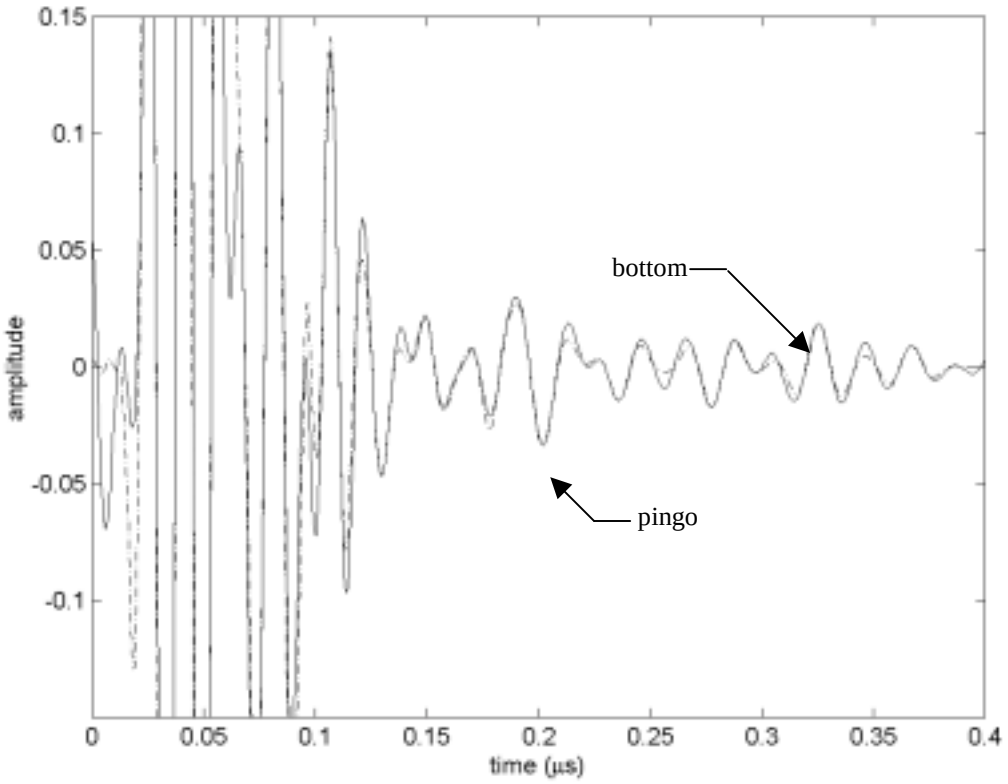

Figure 5-12. Measured and simulated data at the third location.

Table 5-8. Reflection Profile for the Third Location

time (μs)	Amplitude	frequency (MHz)
0.0259	0.0887	64
0.0412	**1.0000**	**61**
0.0549	0.0657	32
0.0631	0.0282	24
0.0793	**0.3061**	**56**
0.0916	0.0117	41
0.1063	0.1358	68
0.1282	**0.0449**	**48**
0.1526	0.0263	45
0.1780	0.0135	55
0.1984	**0.0348**	**40**
0.2380	0.0147	44
0.2599	0.0075	52
0.2787	**0.0173**	**44**
0.3260	**0.0188**	**45**
0.3647	0.0093	46

An experiment was conducted at a second pingo site closer to town. Since there was a gravel road leading to the peak of the site, it was possible to collect data continuously over a traverse from the top of the pingo to well beyond the hill. Although the road provided a path to drag the system, the gravel was rough and the system experienced a large amount of vibration along the traverse. Figure 5-13 shows a radar profile of the site. There are two easily detectable reflections occurring at about 100 ns and 150 ns extending from the top the hill to about 25 m. Shifting time zero to the surface response, assuming an average dielectric constant of about 8, and converting to range places these reflections at about 4-5 m for the top and 7-8 m for the bottom.

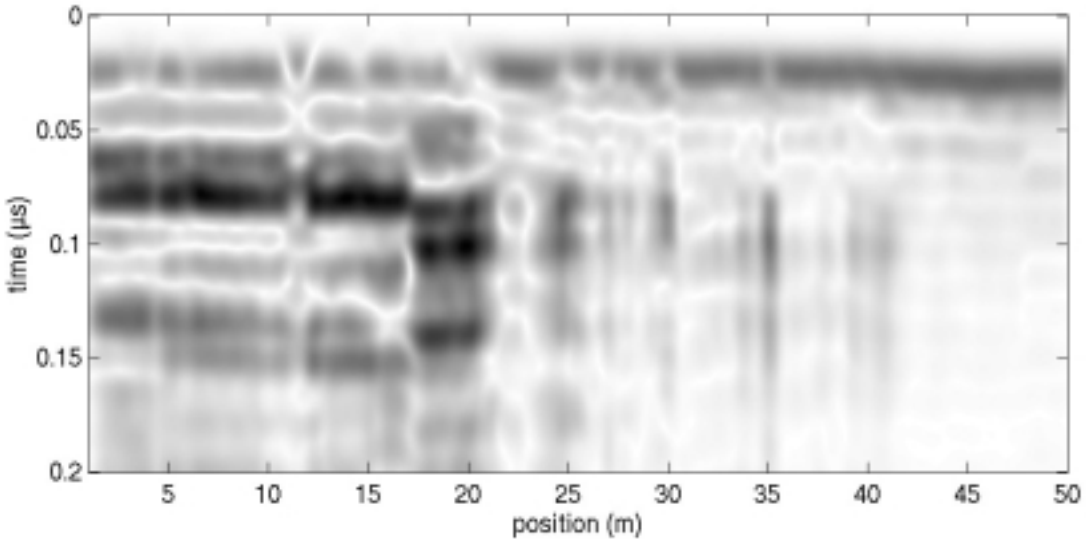

Figure 5-13. Processed image for the second pingo site.

5-3-3 FORT WAINWRIGHT

The final experiment in Alaska was conducted at Fort Wainwright near Fairbanks. Access to the site was made possible using a tracked vehicle, shown in Figure 5-14, which was able to navigate across mud and cross small ponds. At the site, a 4-ft-wide line was cut through a spruce forest and was approximately 300 m in length before it intersected a small pond resulting from recent flooding. From previous radar surveys and drilling, the subsurface is thought to consist of a near-surface saturated thaw layer overlying discontinuous permafrost as shown in Figure 5-15. Beneath the permafrost could lie a small layer of wet soil above the water table and bedrock.

Figure 5-14. Tracked vehicle used to access the site.

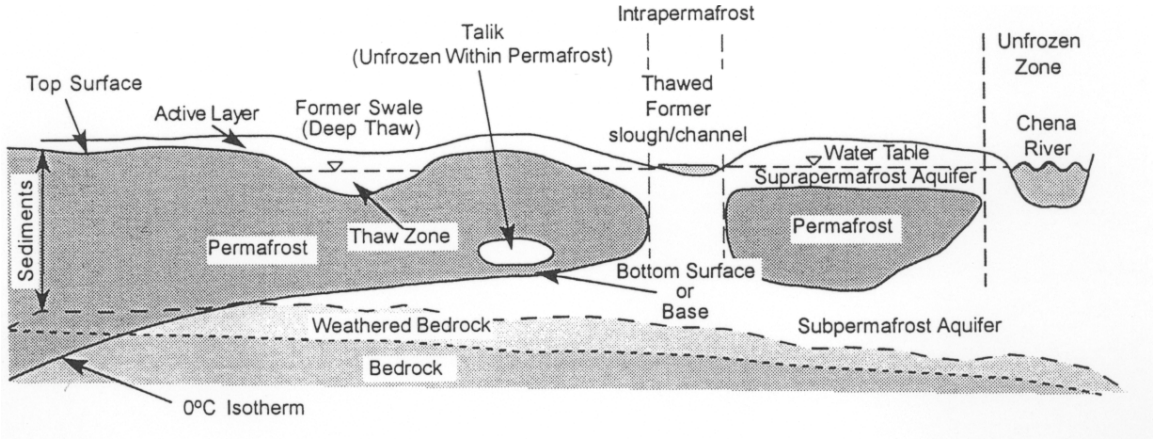

Figure 5-15. Subsurface structure of discontinuous permafrost.

5-3-3-1 SYSTEM MODIFICATIONS

After obtaining poor results the first day at the site, the system was modified to attenuate the antenna feed-through response and reduce the high frequency noise generated by local FM radio stations. Previously, the receiver high-pass filter had been removed to reduce ringing caused by the initial transient of the received signal; however, this also increased the lower beat-frequency IF signal caused by the surface response and antenna coupling. Replacing this filter attenuated the surface/antenna response and increased the usable dynamic range for deeper reflections. An IF amplifier was construction providing an additional 20 dB of gain for the receiver as a result of the attenuated surface/antenna feed-though signal. A 75 MHz low-pass filter was also built and placed in front of the receiver to reduce the interference from the local FM stations. The 3-pole filter was constructed using leaded capacitors and a wire coil inductor. The inductor was constructed by wrapping wire around a small drill bit. Several iterations of the inductor were necessary before the filter was properly tuned. Figure 5-16 shows the measured frequency response of the low-pass filter.

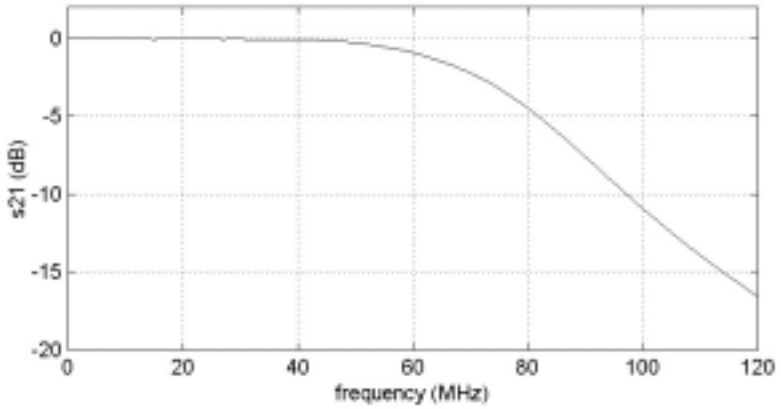

Figure 5-16. Three-pole 75 MHz low-pass filter.

5-3-3-2 RADAR RESULTS

Data were collected continuously along the 300 m traverse. The spacing was approximately 3 cm per trace for a total of 10000 traces. Once again, external noise sources limited the lower frequency band to about 30 MHz prior to the Fourier transform. A few additional signal-processing steps were applied to the data after converting to the time domain. First, any DC bias was removed, and the traces were equalized by normalizing by the standard deviation. Next, the mean across the traverse at each time step was removed to reduce any system effects within the data. Finally, the data were coherently integrated by convolving it with a 16 value Hanning window. The final image is shown in Figure 5-17.

Several events can be detected in the image. A few of particular interest are lightly traced in yellow. The first is the continuous reflection ranging from about 350 ns to 380 ns. This reflection ranges from 0 m to 50 m at 350 ns, it slowly decrease from 50 m to 70 m, and then extends from 70 m to 150 m at about 380 ns. This layer is picked up again at around 190 m and is seen off and on to the end of the traverse. It is possible that this reflection indicates the transition from the frozen permafrost to a wet soil. Beneath this reflection at about 410 ns is a relatively flat layer extending from 0 m to 80 m. There is also a weaker reflection around 400 ns from 100 m to 150 m. Due to the flat characteristics of these layers, they could indicate a water table existing below the permafrost. This layer may disappear as the permafrost becomes deeper and extend into the water table. There seem to be many near-surface events within the image. The most prominent shown across the entire image is the ringing of the near-surface active thaw layer.

The radar results were compared with those collected with an “impulse”-type commercial Geophysical Survey Systems, Inc. (GSSI) System 10B control unit and CD10A video display [39]. The antenna subsystems for this unit were 50 MHz resistively loaded dipoles attached to a standard GSSI 100 MHz transmitter and receiver

as shown in Figure 5-18. To reduce cable noise, the transmitter and receiver were connected with a fiber optical link. With a combined weight of well over 100 kg, the antenna were dragged 5 m behind the tracked vehicle used to access the site. Also, a large antenna separation of 4.6 m (more than twice the distance used with the FM-CW system) was used to avoid saturating the receiver.

The processed image for the commercial system is shown in Figure 5-19. The data were collected along the same line but in the opposite direction. Some of the same features seen in the Figure 5-17 can also be noticed in this image. First, the response just below the antenna coupling is evident in both images and shows a similar trend. In Figure 5-17 this response is level from 0 to 50 m and then begins to rise until about 120 m. Figure 5-19 shows the same response in the opposite direction. It falls from about 170 m to 250 m and is level for the remainder of the traverse. The interface between the permafrost and saturate soil occurring at approximately 350 ns can also be noticed in both images.

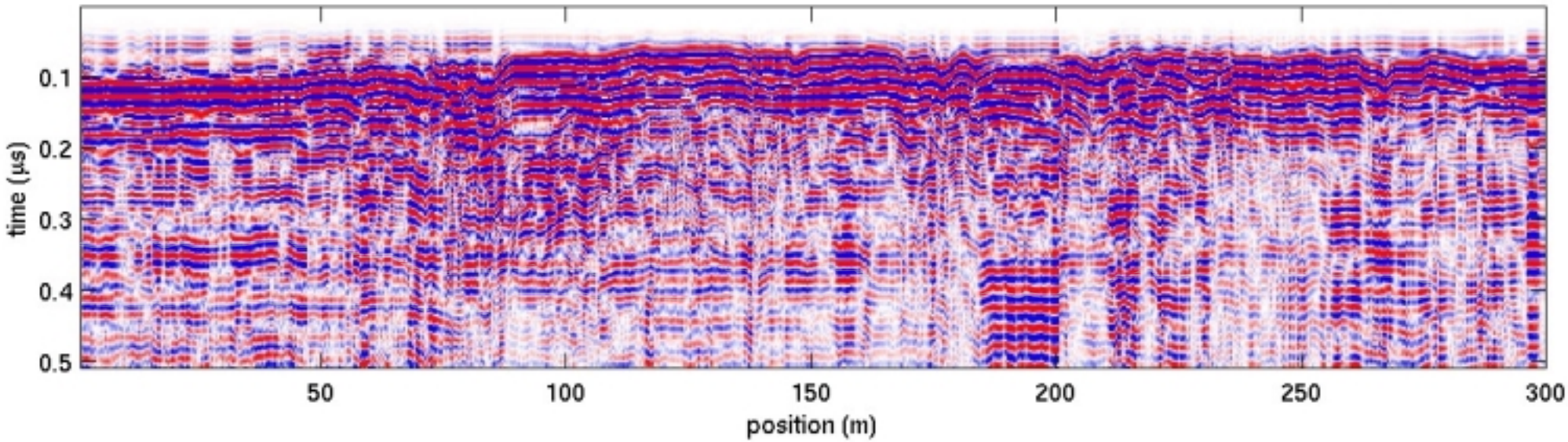

Figure 5-17. Image of data collected over a 300 m traverse at Fort Wainwright

Figure 5-18. GSSI 50 MHz antenna subsystems.

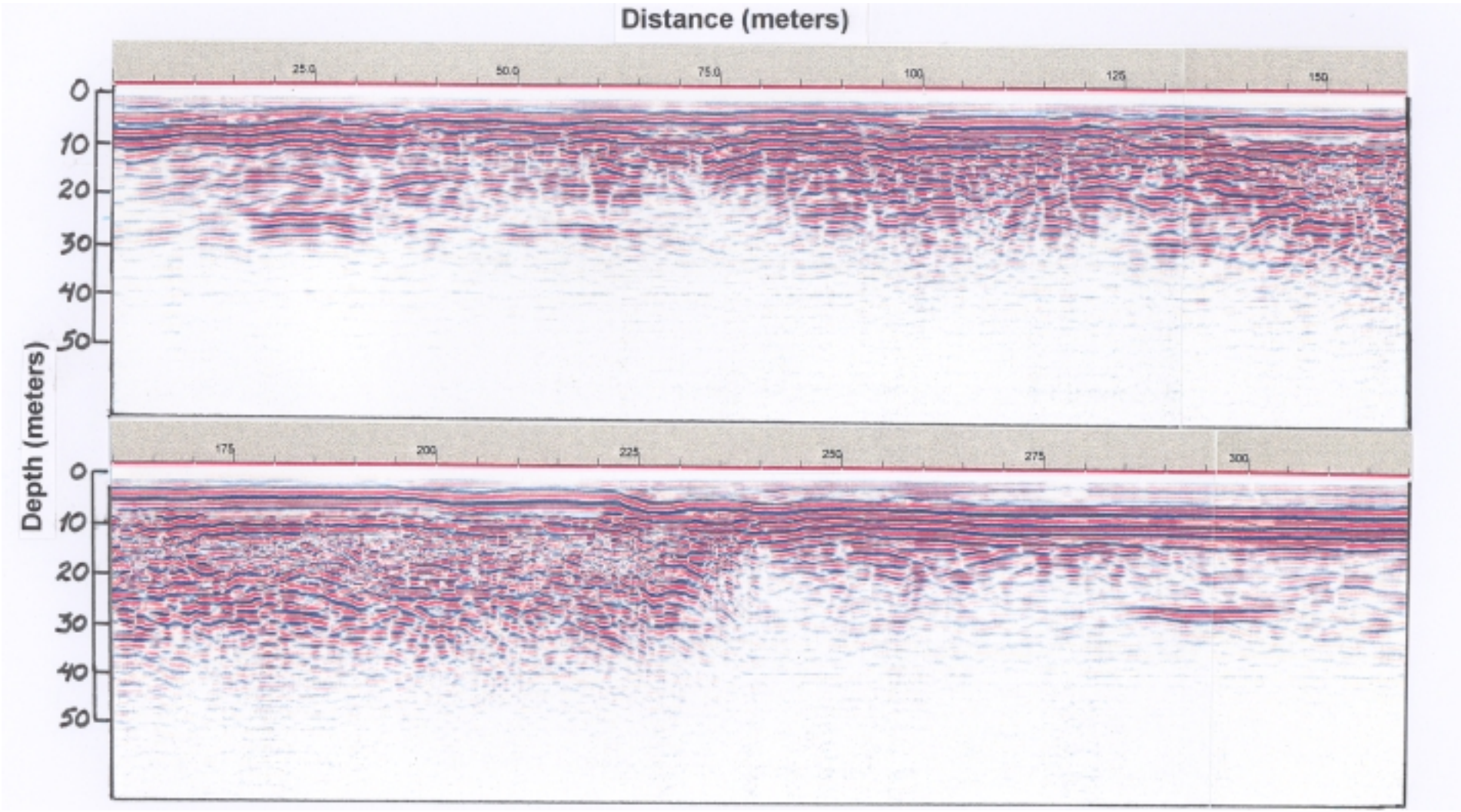

Figure 5-19. Image of data collected with the commercial GPR.

CHAPTER 6

CONCLUSIONS AND FUTURE WORK

6-1 INTRODUCTION

The main goal of this work was to investigate the use of radar to probe the subsurface of Mars. The intent of such a system is to map the subsurface structure for detecting water in any form within the planet. This could include near-surface water and ice lenses, large segregated bodies of ice, or even an underlying global reservoir. This dissertation presents a complete description for the simulation, design, and operation of a radar system for Mars exploration. The work involves extensive simulations over a wide variety of subsurface models, the actual design and construction of a prototype system, tests of the system over permafrost and segregated bodies of ice, and a study of innovative signal processing algorithms to help interpret radar data. Results, conclusions, and future work are summarized below.

6-2 SIMULATION RESULTS

Chapter 2 investigates the ability of a surface-penetrating radar on Mars to accomplish the main goal of detecting water. The response of a surface-penetrating radar is highly dependent on the stratigraphy and lithology of the subsurface layers, and, since the electrical properties of these layers on Mars are unknown, predicting the performance of a radar requires extensive simulations over a wide range of models. The simulation models presented in this dissertation range from simple two- to three-layer configurations to multi-layer configurations of different geological locations. The results of these simulations provide feedback for the radar design and evaluation. The results and conclusions obtained from these simulations are summarized focusing on unambiguous detection and penetration depth.

One main concern that must be reiterated is the ability for a system to detect water or ice unambiguously. The simulations presented in this dissertation suggest that unless there exists a large body that can be distinguished from the local stratigraphy, such as a global subsurface aquifer, unambiguous detection from radar measurement alone will be very difficult if not impossible. Simple mixing formulas show that the electrical properties of soils containing water or ice are difficult to distinguish from the neighboring drier layers, especially for low-porosity soil mixtures.

Another important concern is the expected penetration depth of a radar system. The ability of a radar system to penetrate and detect a subsurface interface will depend on both the reflection coefficient of the interface and the amount of attenuation experienced though the overlying media. Based on the simulation results, the penetration depth for a radar system will range from up to a few tens of meters for a high-frequency system (> 100's MHz) to a few hundreds of meters for an

intermediate-frequency system (10's to 100's MHz) to a kilometer or more for a low-frequency system (< 10's MHz).

6-3 Signal Processing

To help with data interpretation and clutter reduction a signal processing algorithm was proposed in Chapter 4. This iterative method involved detecting the maximum reflection, reproducing the response including the sidelobes, and subtracting them from the actual data. Since the sidelobe structure was reproduced along with the maximum signal, when the signal was subtracted, all the associated sidelobes were also canceled. This method worked very well when applied to transmission line data. In fact, it outperformed the results obtained from applying a commonly used Hanning window in terms of pulse width and sidelobe levels.

Results from actual surface-penetrating radar data indicated the algorithm is also valuable for data interpretation. The process provides a means of quantifying the location, amplitude, and frequency content of each reflection within a radar response. From this information, conclusions can be made concerning the origin of a specific reflection: for example whether it is surface clutter or a subsurface interface. The signal processing algorithm presented in this dissertation will prove to be useful in both clutter reduction and data interpretation.

6-4 Radar System and Experiments

Currently, the state of the art for ground-penetrating radars are high-power, "impulse"-type systems. One of the major technical goals of this work was to develop a lightweight, low-power, frequency-modulated radar system that could detect subsurface deposits of ice and water. For initial testing and experiments, an

inexpensive prototype system was developed using off-the-shelf connectorized components and evaluation boards. Chapter 4 outlined the complete design of the system including the antenna subsystems. To verify the operation of this prototype system, Chapter 5 presented the experiments that were conducted at sites in Lawrence, Kansas, and Fairbanks, Alaska.

The results from the experiments indicate that the prototype system was successful in detecting subsurface deposits of ice and water. These experiments were conducted at a number of different test sites, each unique in the phase and location of the subsurface water. In all cases, the results showed a strong correlation with the prior information obtained through drilling, seismic surveys, and other GPR experiments. The results consistently showed coherent reflections at the locations where the water or ice was thought to exist.

At a test site over discontinuous permafrost, a commercial "impulse"-type system was used as a benchmark for testing the prototype system. The FM-CW system showed similar results even under the extreme conditions that were encountered during the experiment. Both systems were able to detect a permafrost interface at a depth of around 20 to 25 m. Furthermore, considering the size and weight requirements for a mission, the prototype system is substantially smaller and lighter than the commercial system.

6-5 Proposed System for a Lander-Rover

Suggesting a single, optimal design for a surface-penetrating radar on Mars would be practically impossible since the design will be dependent on the specific mission objectives, previous data, and spacecraft requirements. The system presented in this work was a low- to medium-frequency lightweight low-power rover/lander-

based system intended to probe to a depth of hundreds of meters to 1 km. When compared to a commercial system that was not designed with power and weight restrictions, this prototype system shows similar results. Based on the simulation and experiment results, an FM-CW system operating between a few megahertz to a few hundreds of megahertz is proposed for a lander/rover-based mission.

This research has shown that a lightweight, low-power system can be easily built to meet the size and weight requirements, and operate over a wide enough frequency band to ensure reasonable penetration depth without sacrificing resolution. Using a high-speed digital synthesizer and a simple receiver design, the entire system could be incorporated onto a single multi-layer PCB with surface-mount components. Also, the antenna subsystems presented in this dissertation include a relatively small, mobile dipole receive antenna that could be used in conjunction with a mobile/stationary bowtie to perform either monostatic or bistatic measurements.

Bistatic measurements would benefit the radar system for a few reasons. First, moving the receive antenna farther from the transmit signal would reduce the antenna feed-through and surface response along with their sidelobes. Also, with this reduction, a higher gain could be applied to the received signal without saturating the analog to digital converter. This would increase the usable dynamic range for the deeper reflections. Similar to seismic processing, bistatic measurements would allow velocity analysis to be preformed on the collected data. As shown in section 5-2, velocity analysis can be used to obtain dielectric and depth estimates of the subsurface reflections. This type of information would provide valuable information of characterizing subsurface deposits of ice or water.

6-6 CONCLUSION

In this dissertation, a surface-penetrating radar for Mars exploration was simulated, designed, constructed, and tested. To aid in data processing and interpretation, a signal processing scheme was presented and applied to some of the experimental data. Results for both the simulations and experiments were shown, and the comparisons showed strong agreements. Additionally, the experimental results were compared with those obtained from a well-established commercial system. The similarities of these results help to support the idea of using a lightweight, low-power, FM-CW system for Mars exploration and also verify the prototype design. In summary, the research presented here should provide a strong foundation for the continued development of a lander/rover-based system.

REFERENCES

[1] Kieffer, H. H., B. M. Jakosky, and C. W. Snyder, “The planet Mars: from antiquity to the present,” in *Mars*, edited by H. H. Kieffer, B. M. Jakosky, C. W. Snyder, and M. S. Matthews, pp. 1-33. University of Arizona Press, Tucson, 1992.

[2] Baker, V. R., R. G. Strom, V. C. Gulick, J. S. Kargel, G. Komatsu, and V. S. Kale, “Ancient oceans, ice sheets and the hydrological cycle on Mars,” *Nature*, vol. 352, pp. 589-594, 1991.

[3] Carr, M. H., *Water on Mars*, Oxford University Press, New York, 1996.

[4] MEPAG Document

[5] Available at http://mars3.jpl.nasa.gov/mgs/msss/camera/images/index.html

[6] Squyres, S. W., S. M. Clifford, R. O. Kuzmin, J. R. Zimbelman, and F. M. Costard, “Ice in the Martian regolith,” in *Mars*, edited by H. H. Kieffer, B. M. Jakosky, C. W. Snyder, and M. S. Matthews, pp. 557-593. University of Arizona Press, Tucson 1992.

[7] Hoffman, N., "Searching for water on a cold dry Mars," Conference on the Geophyical Detection of Subsurface Water on Mars, Houston, TX, 2001.

[8] Tanaka, K. L., D. H. Scott, and R. Greenley, “Global Stratigraphy,” in *Mars*, edited by H. H. Kieffer, B. M. Jakosky, C. W. Snyder, and M. S. Matthews, pp. 345-382. University of Arizona Press, Tucson, 1992.

[9] Ulaby F. T., R. K. Moore, and A. K. Fung, *Microwave Remote Sensing Active and Passive,* Vol. 2—Radar Remote Sensing and Surface Scattering and Emission Theory, Artech House, Inc, Norwood MA, 1982.

[10] Cheng, K. S., and A. K. Fung, "Comparison of backscattering models for rough surfaces," *IEEE Transactions on Geoscience and Remote Sensing, v*ol. 33, no. 1, pp. 195-200, 1995.

[11] Hsieh, C. Y., A. K. Fung, G. Nesti, A. J. Sieber, and P. Coppo, "Further study of the IEM surface scattering model," *IEEE Transactions on Geoscience and Remote Sensing,* vol. 35, no. 4, pp. 901-909, 1997.

[12] Picardi, G., S. Sorge, R. Seu, J. J. Plaut, W. T. K. Johnson, R. L. Jordan, D. A. Gurnett, R. Orosei, L. Borgarelli, G. Braconi, C. Zelli, and E. Zamplini, "The Mars Advanced Radar for Subsurface and Ionosphere Sounding (MARSIS): concept and performance," IGARSS'99, Hamburg, Germany, pp. 2674-2677, 1999.

[13] Available at http://ltpwww.gsfc.nasa.gov/tharsis/mola.html

[14] Olhoeft, G. R., and D. W. Strangway, "Electrical properties of the surface layers of Mars," *Geophysical Research Letters,* vol. 1, no. 3, pp. 141-143, 1974.

[15] Olhoeft, G. R., and D. W. Strangway, "Dielectric properties of the first 100 meters of the Moon," *Earth and Planetary Science Letters,* vol. 24, pp. 394-404, 1975.

[16] Olhoeft, G. R., “Electrical properties of rocks,” in *Physical Properties of Rocks and Minerals*, edited by Touloukian Y. S., W. R. Judd, and R. F. Roy, Hemisphere Publishing Co., New York, pp. 257-330, 1989.

[17] Hviid, S. F., M. B. Madsen, H. P. Gunnlaugsson, W. Goetz, J. M. Knudsen, R. B. Hargraves, P. Smith, D. Britt, A. R. Dinesen, C. T. Mogensen, M. Olsen, C T. Pedersen, L. Vistisen, “Magnetic properties experiments on the Mars Pathfinder lander: preliminary results,” *Science*, vol. 278, pp. 1768-1770, 1997.

[18] Carmichael, R. S., “Magnetic properties of minerals and rocks,” in *Handbook of Physical Properties of Rocks*, Vol. II, edited by R. S. Carmichael, pp. 229-287, CRC Press, Inc., Florida 1982.

[19] Yang, Y. P., and D. W. Emerson, “Electromagnetic conductivities of rock cores: theory and analog results,” *Geophysics*, vol. 62, no. 6, pp. 1779-1793, 1997.

[20] Christensen, P. R. and H. J. Moore, “The Martian surface layer,” in *Mars*, edited by H. H. Kieffer, B. M. Jakosky, C. W. Snyder, and M. S. Matthews, et al., pp. 696-729. Univ. of Arizona Press, Tucson, 1992.

[21] Allen, C. C., D. M. Jager, R. V. Morris, D. J. Lindstrom, M. M. Lindstrom, and J. P. Lockwood, "Martian soil simulant available for scientific, educational study," *EOS*, vol. 79, pp. 1 and 4, August 1998.

[22] Frasch, L. L., "Electromagnetic properties of dry and water saturated basalt rock, 1-110 GHz," *IEEE Transactions on Geoscience and Remote Sensing*, vol. 36, no. 3, pp. 754-765, May 1998.

[23] Hoekstra, P. and A. Delaney, "Dielectric properties of soils at UHF and microwave frequencies," *Journal of Geophysical Research*, vol. 79, no. 11, pp. 1699-1707, April 1974.

[24] Ulaby, F. T., T. H. Bengal, M. C. Dobson, J. R. East, J. B. Garvin, and D. L. Evans, "Microwave dielectric properties of dry rocks," *IEEE Transactions on Geoscience and Remote Sensing*, vol. 28, no. 3, pp.325-336, 1990.

[25] Leuschen, C. J., "Analysis of the complex permittivity and permeability of a Martian soil simulant from 10 MHz to 1 GHz," IGARSS'99, Hamburg, Germany, 1999.

[26] Christensen, P. R., "The spatial distribution of rocks on Mars," in *Mars*, edited by H. H. Kieffer, B. M. Jakosky, C. W. Snyder, and M. S. Matthews, pp. 217-238, Univ. of Arizona Press, Tucson, 1992.

[27] Smith, P. H., et al., "Results from the Mars Pathfinder camera," *Science*, vol. 278, pp. 1758-1764, 1997.

[28] Kong, J. A., *Electromagnetic Wave Theory*, John Wiley and Sons, New York, 1986.

[29] Simulation models

[30] Davis, J. L., and A. P. Annan, "Ground-penetrating radar for high-resolution mapping of soil and rock stratigraphy," *Geophysical Prospecting*, vol. 37, pp. 531-551, 1989.

[31] Fujimoto, K., A. Henderson, K. Hirasawa, and J. R. James, *Small Antennas*, Research Studies Press LTD, England, 1987.

[32] Annan, A. P., W. M. Waller, D. W. Strangway, J. R. Rossiter, J. D. Redman, and R. D. Watts, "The electromagnetic response of a low-loss, 2-layer, dielectric earth for horizontal electric dipole excitation," *Geophysics*, vol. 40, no. 8, pp. 285-298, 1975.

[33] Compton, R. C., R. C. McPhedran, Z. Popovic, G. M. Gebeiz, P. P. Tong, and D. B. Rutledge, "Bow-tie antennas on a dielectric half-space: theory and experiment," *IEEE Transactions on Antennas and Propagation*, vol. AP-35, no. 6, pp. 622-631, 1987.

[34] Stutzman, W. L., and G. A. Thiele, *Antenna Theory and Design*, John Wiley and Sons, Inc., New York, 1981.

[35] Harris, F. J., "On the use of windows for harmonic analysis with the discrete Fourier Transform," *Proceedings of the IEEE*, vol. 66, no. 1, pp. 51-83, 1978.

[36] Knapp, R.W., "Vertical resolution of thick beds, thin beds, and thin bed cyclotherms," *Geophysics*, vol. 55, no. 9, pp. 1183-1190, 1990.

[37] Sensors and Software pulse ekko 1000 users manual, Mississauga, Ontario, Canada.

[38] Yee, K. S., "Numerical solution of initial boundary-value problems involving Maxwell's equations in isotropic media," *IEEE Transactions on Antennas and Propagation*, vol. AP-14, pp. 302-307, 1966.

[39] Arcone, S., C. Leuschen, and S. P. Gogineni, “Comparative permafrost radar tests: Fairbanks, Alaska,” CRREL report, Cold Regions Research and Engineering Laboratory, Hanover NH, 2001.

APPENDIX A

MATLAB FILES

LIST OF FILES

tmplt.txt – simulation model template, ASCII file.

proc1.m – Main simulation procedure.

getmodel.m – loads the simulation model from an ASCII file.

mpulse.m – generates a frequency modulated pulse.

pulse.m – generates a Gaussian pulse.

er_ice.m – calculates the complex permittivity of ice versus frequency and temperature.

er_water.m – calculates the complex permittivity of water versus frequency and temperature

er_saltwater.m – calculates the complex permittivity of water versus frequency, temperature, and salinity.

geoptics_t.m – calculates the geometric optics backscattering coefficient versus time for a given height and surface roughness.

geoptics_x.m – calculates the geometric optics backscattering coefficient versus surface location for a given height and surface roughness.

g1f.m – calculates the one-dimensional reflection coefficient for a n-layered medium.

plane1d.m – calculates the one-dimensional reflection coefficient for a n-layered medium.

```
%                                                       surface
%fc     BW3dB   Nt      dt      Nx      dx      slope


%       Soil            Fill            Rocks
%depth  pore(%) Fe(%)   sat(%)  phase   size    vol(%)


%phases
%1: air
%2: ice
%3: water-pure
                        %4: water-salt
```

Proc1d.m

```
clear;                              %clear workspace
getmodel;                           %read the geophysical model from
file

Ae = 4*pi*(3e8/fc)^2;               %scalar for receiving antenna
bs_t = geoptics_t( d(1), tt, slp ); %rough surface backscatter
area = 2*pi*d(1)*3e8/BW;            %radial disc/ring area

R1 = g1f(k,d);                      %plane wave response

%check frequency ranges
if ff(1) == 0,
   R1(1) = 0;
end;
if ff(1) < 0,
   fprintf('error: frequency less than zero.\n');
end;

%ideal plane-wave response
r1 = ifft((R1.*P.*exp(j*2*pi*ff*2*d(1)/3e8)));

%rough surface response
r3a = sqrt(Ae*area)* ...
   conv(abs(r1),sqrt(bs_t).*(1)/(sum(abs(p)))) ...
   /(4*pi*d(1))^2; %3D tdomain

r3 = sqrt(Ae*area)* ...
   conv(r1,sqrt(bs_t).*(randn(Nt,1)+j*randn(Nt,1))/sqrt(2*sum(abs(p))))
...
   /(4*pi*d(1))^2; %3D tdomain

%specular response
r3b = sqrt(Ae)*r1/(8*pi*d(1));
```

getmodel.m

```
%load model
load model.txt
mdl = model;

%%%%%%%%%%%%%%%%%%
%RADAR PARAMETERS%
%%%%%%%%%%%%%%%%%%
in = mdl(1,:);
fc = in(1); %center frequency
BW = in(2); %bandwidth
Nt = in(3); %number of time points
dt = in(4); %sample time
Nx = in(5);
dx = in(6);
slp = in(7); %surface and subsurface rms slopes

xx = 0:dx:Nx*dx;

tt = (0:dt/2:(Nt-0.5)*dt)'; %time vector
p = mpulse(tt,BW,2/BW,fc); %pulse (time domain)
P = fft(p); %pulse (frequency domain)
P = P(1:Nt); %(only positive frequencies)
p = ifft(P);
tt = (0:dt:(Nt-1)*dt)';

df = 1/(dt*Nt); %frequency step
ff = (df:df:df*Nt)'; %frequency vector (only positive frequencies)

%%%%%%%%%%%%%%%%%%%
%GEOPHYSICAL MODEL%
%%%%%%%%%%%%%%%%%%%
e0 = 1e-9/(36*pi);
u0 = (4e-7)*pi;

Nl = size(mdl,1)-1; %number of layers
m = mdl(2:Nl+1,:); %model
d = m(1:Nl,1)'; %depth profile
pore = m(1:Nl,2)'; %porosity profile
fe = m(1:Nl,3)'; %percent iron oxide
sat = m(1:Nl,4)'; %percent saturation
phase = m(1:Nl,5)'; %phase profile: 0-air, 1-ice, 2-water, 3-salt
water, 4-?
vola = m(1:Nl,6)'; %volume debris radius
fvol = m(1:Nl,7)'; %volume debris fraction volume

%%%%%%%%%%%%%%%%%%%%%%%
%ELECTRICAL PROPERTIES%
%%%%%%%%%%%%%%%%%%%%%%%
eb_dry = 8.*(1-j*(0.00175+0.000825*fe));
for i1 = 1:Nl,
   switch phase(i1)
   case 0 %air
      eb_fill(1:Nt,i1) = ones(Nt,1);
   case 1 %pure ice
```

```
      eb_fill(1:Nt,i1) = er_ice(ff,250);
   case 2 %pure water
      eb_fill(1:Nt,i1) = er_water(ff,250);
   case 3 %salt water
      eb_fill(1:Nt,i1) = er_salt_water(ff,250,.02);
   end;
end;

%%%%%%%%%%%%%%%
%MIXING FORMULA%
%%%%%%%%%%%%%%%
for i1 = 1:Nl,
   ebg(1:Nt,i1) =
eb_fill(1:Nt,i1).^(pore(i1)/100*sat(i1)/100).*eb_dry(i1).^(1-
pore(i1)/100);
end;

%%%%%%%%%%%%%%%
%VOLUME DEBRIS%
%%%%%%%%%%%%%%%
for i1 = 1:Nl,
   er(1:Nt,i1) = vol(ff,ebg(1:Nt,i1),eb_dry(i1),vola(i1),fvol(i1)/100);
end;

%%%%%%%%%%%%
%gpr profile%
%%%%%%%%%%%%
k = 2*pi*(ff*ones(1,Nl)).*sqrt(er*e0*u0);
```

mpluse.m

```
function[ p ] = mpulse( t , BW , t0 , fc )
%generates a Gaussian pulse of bandwidth BW
%BW is given by integral(abs(P(f)))/max(abs(P(f)))
%pulse width is inversely proportional to BW
%pulse maximum value is 1.0
%inputs:  t: time vector
%         BW: bandwidth
%         t0: pulse shift
%output:  p: pulse waveform
```

pulse.m

```
p = cos(2*pi*fc*(t-t0)).*exp(-(sqrt(pi)*BW*(t - t0)).^2);
function[ p ] = mpulse( t , BW , t0 , fc )
%generates a Gaussian pulse of bandwidth BW
%BW is given by integral(abs(P(f)))/max(abs(P(f)))
%pulse width is inversely proportional to BW
%pulse maximum value is 1.0
%inputs:  t: time vector
%         BW: bandwidth
%         t0: pulse shift
%output:  p: pulse waveform

p = (t - t0).*exp(-(sqrt(pi)*BW*(t - t0)).^2);
p = p/max(abs(p));
```

er_ice.m

```
function[ er ] = er_ice( f, T );
%calculate the complex permittivity for ice
%inputs:  f = frequency vector
%         T = Temperature
%outputs: er = complex permittivity vector versus frequency

k = 8.6176e-5;
er_s = 3.2+20715/(T-38);
er_inf = 3.2;
tau = 4.76e-16*exp(0.577/(k*T));
er = er_inf + (er_s - er_inf)./(1+j*2*pi*f*tau);
```

er_water.m

```
function[ er ] = er_water( freq, Temp )
%calculate the complex permittivity for pure water
%inputs:  freq = frequency vector
%         Temp = Temperature
%outputs: er = complex permittivity vector versus frequency

w = 2*pi*freq;
k = 8.6176e-5;
es = 295.68 - 1.2283*Temp + (2.094e-3)*Temp.^2 - (1.41e-6)*Temp.^3;
einf = 4.2;
tau1 = (5.62e-15)*exp(0.188./(k*Temp));
er = einf + (es-einf)./(1+j*w*tau1);
```

er_saltwater.m

```
function[ er ] = er_saltwater( freq, Temp, salt )
%calculate the complex permittivity for salt water
%inputs:  freq = frequency vector
%         Temp = Temperature
%         salt = salinity, molar concentration
%outputs: er = complex permittivity vector versus frequency

w = 2*pi*freq;
k = 8.6176e-5;
n2 = 1.8;
es = 295.68 - 1.2283*Temp + (2.094e-3)*Temp.^2 - (1.41e-6)*Temp.^3 ...
   - 13*salt + 1.065*salt.^2 - 0.03006*salt.^3;
einf = 4.2;
alpha = 0.012;
tau1 = (5.62e-15)*exp(0.188./(k*Temp));

er = einf + (es-einf)./(1+(j*w*tau1).^(1-alpha));

T = Temp-273.15;
B = [ [3.47 -59.21 0.4551 -9.346e-5 -1.766e-6]; ...
      [-6.65 198.1 -0.2058 7.368e-5 8.768e-7]; ...
      [2.633 -64.8 0.005799 6.741e-5 -2.136e-7] ];
T = [ 1; 1./Temp; Temp; Temp.^2; Temp.^3 ];
c = [ salt salt.^(3/2) (salt.^2).*log(salt) ];
sigma = c*B*T;

er = er - j*sigma./(2*pi*freq*(1e-9/(36*pi)));
```

geoptics_t.m

```
function[ sigma0 ] = geoptics_t( H , t , s );
%geometric optics rough surface backscattering
%assuming small angle H>>x
%inputs:  H: height of radar
%         x: x offset vector
%         s: rms slope of surface
%output:  s0: backscattering coefficient vs. time

sigma0 = exp(-1.5e8*t/(H*s^2))/(2*s^2);
```

geoptics_x.m

```
function[ sigma0 ] = geoptics_x( H , x , s );
%geometric optics rough surface backscattering
%assuming small angle H>>x
%inputs:  H: height of radar
%         x: x offset vector
%         s: rms slope of surface
%output:  s0: backscattering coefficient

sigma0 = exp(-0.5*(x/(s*H)).^2)/(2*s^2);
```

g1f.m

```
function[ ref ] = g1f( k , l )
%calculate the plane wave response for a layered media
%inputs:  k = gpr profile, wavenumber of each layer, size(Nf,Nl)
%         l = gpr profile, thickness of each layer
%outputs: ref = reflection coefficient, size(Nf)

nk = size(k); %nk(1) number of freq points, nk(2) number of layers

for i1 = 1:nk(1),i1/nk(1)
%wave(1:2,i) = [ -x direction ; +x direction ]
%-x directed wave
wave(1:2,i1) = [ 1; 0 ];

%advance wave keeping the function and the 1st derivative continuous
%advance wave keeping E and H continuous
for i2 = nk(2)-1:-1:1,
   a = (k(i1,i2)+k(i1,i2+1));
   b = (k(i1,i2)-k(i1,i2+1));
   c = exp(j*k(i1,i2)*l(1,i2));
   matrix = (.5/k(i1,i2))*[ a*c b*c ; b/c a/c ];
   wave(1:2,i1) = matrix*wave(1:2,i1);
end;

%normalize the wave

ref(i1,1) = wave(2,i1)/wave(1,i1);
end;
```

Plane1d.m

```
function[ R ] = plane1d( k , d );
%calculate the plane-wave response (frequency domain) for a layered
medium
%does not account for multiple reflections
%inputs:  k: alpha + j*beta,          dimensions::(freq,layer)
%         d: thickness of each layer, dimensions::(1,layer)
%output:  R: response for each layer, dimensions::(freq,layer-1)

N = size(k);
for i1 = 1:N(2)-1,
   R(:,i1) = (k(:,i1)-k(:,i1+1))./(k(:,i1)+k(:,i1+1)) ...   %reflection
      .*prod((2*k(:,1:i1-1)./(k(:,1:i1-1)+k(:,2:i1))) ...
%transmission down
      .*(2*k(:,2:i1)./(k(:,1:i1-1)+k(:,2:i1))),2) ...
%transmission up
      .*exp(-j*2*sum(k(:,1:i1).*(ones(N(1),1)*d(1:i1)),2));
%propagation
end;
```

APPENDIX B

SIMULATION MODELS

Plane wave simulations were calculated for each of the models listed below. Rather than determining the response from multiple frequency pulses, a single wideband simulation was conducted for each model. From the wideband simulation, a plot of the spectrum versus time delay is generated by calculating the Fourier transform of a sliding window. This appendix shows the results for each simulation model. Each figure contains (from left to right): the permittivity profile, an amplitude plot, a dB plot, and the image of the spectrum versus time delay. Additionally, nominal values of 10 % iron concentration and 10 cm inclusions with a 5 % volume fraction.

List of Simulation Models

NS-1 **Equatorial Site**
NS-2 **"Shallow Seep" Site**
NS-3 **Northern Plains Site**
NS-4 **Simple Massive Ice Lens**
NS-5 **Simple Near Surface Aquifer**
NS-6 **Simple Deep Aquifer**
DS-1 **"Shallow " Global Aquifer**
DS-2 **"Perched and Deep" Global Aquifer**
P-1 **Polar Basil Melting**
P-2 **Deep Polar Aquifer**

Table B-1. Simulation Model: NS-1 Equatorial Site

depth	lithology	ϕ%	s%	fill
400km	air	100	-	-
1	eolian sediment	50	0	air
3	indurated sediment	15	0	air
5	sediment-filled basalt	50	0	air
10	dense basalt	5	0	air
100	layered basalt	10	0	air
110	eolian sediment	50	100	ice
150	layered basalt	10	50	ice
152	fluvial sediment	20	0	air
160	volcanic ash	50	0	air
200	layered basalt	10	0	air
220	crater ejecta	20	100	ice
250	layered basalt	10	100	ice
255	eolian sediment	50	0	air
350	layered basalt	10	0	air
355	fluvial sediment	20	0	air
500	layered basalt	10	0	air
750	layered basalt	10	100	ice
760	volcanic ash	50	100	ice
900	layered basalt	10	100	ice
1000	layered basalt	10	100	ice

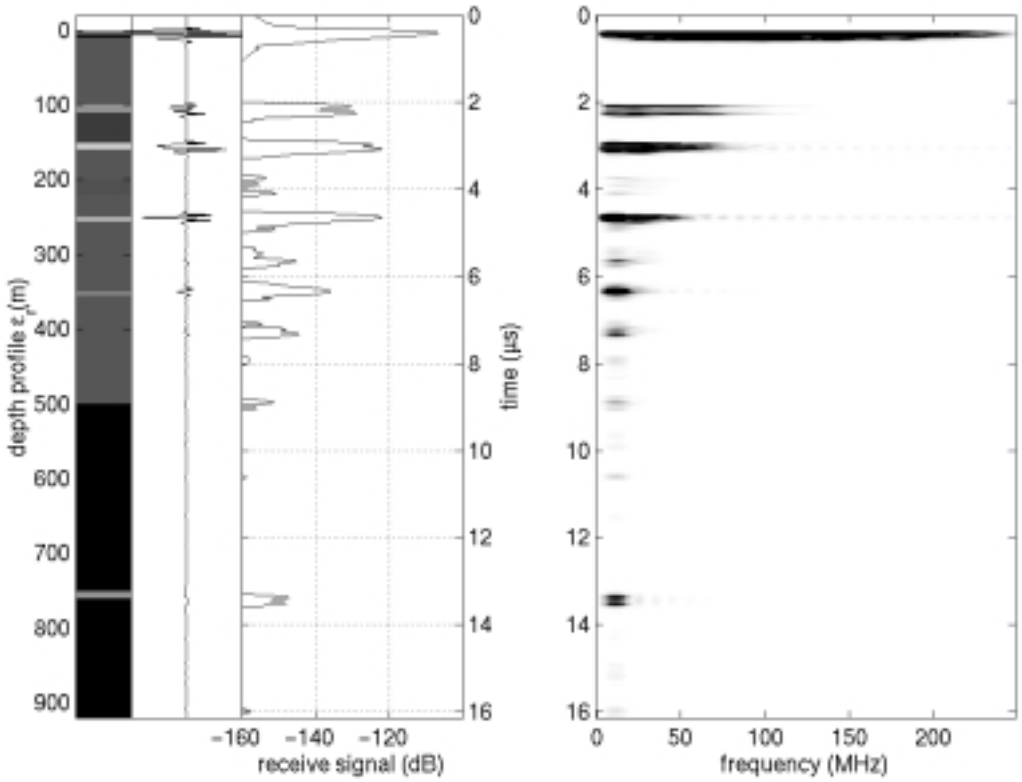

Figure B-1. Simulation Model: NS-1 Equatorial Site.

Table B-2. Simulation Model: NS-2 "Shallow Seep" Site

depth	lithology	ϕ%	s%	fill
400km	air	100	-	-
1	eolian sediment	50	0	air
3	indurated sediment	15	0	air
5	sediment-filled basalt	50	100	ice
10	dense basalt	5	100	ice
100	layered basalt	10	100	gas hydrate
110	eolian sediment	50	100	ice
150	layered basalt	10	100	ice
152	fluvial sediment	20	100	ice
160	volcanic ash	50	90/10	ice/thin films of super-cooled water
200	layered basalt	10	100	brine
220	crater ejecta	20	100	brine
250	layered basalt	10	50	brine
255	eolian sediment	50	20	brine
350	layered basalt	10	20	brine
355	fluvial sediment	20	20	brine
500	layered basalt	10	20	brine
750	layered basalt	10	20	brine
760	volcanic ash	50	20	brine
900	layered basalt	10	20	brine
1000	layered basalt	10	20	brine

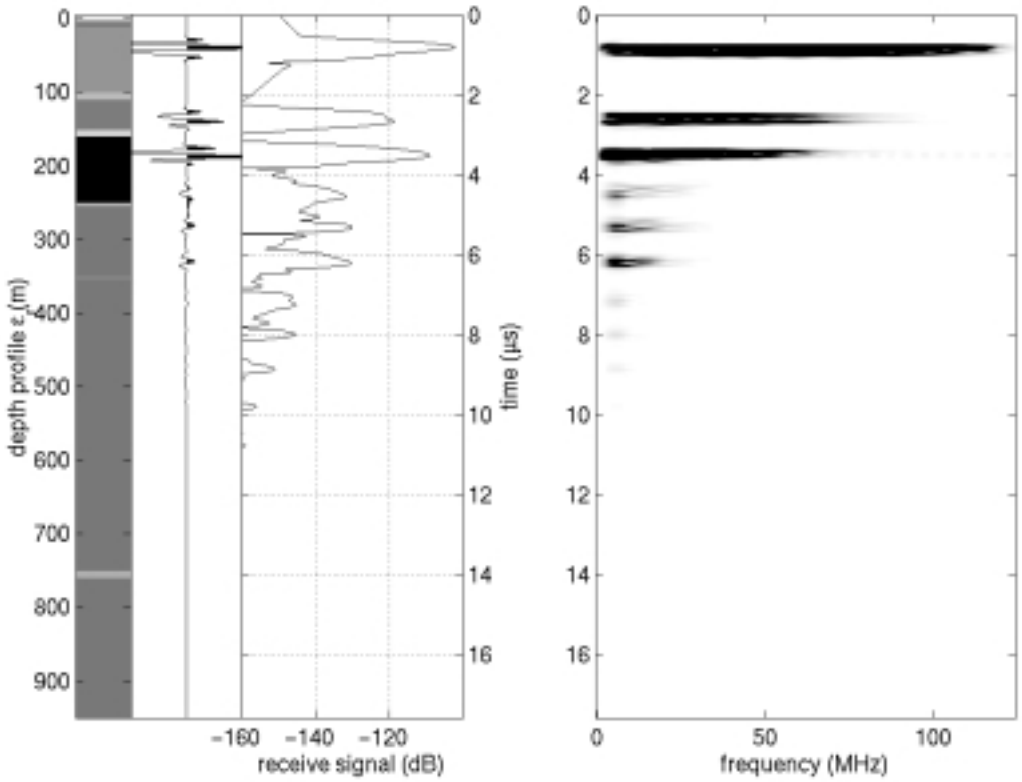

Figure B-2. Simulation Model: NS-2 "Shallow Seep" Site.

Table B-3. Simulation Model: NS-3 Northern Plains Site

depth	lithology	ϕ%	s%	fill
400km	air	100	-	-
1	eolian sediment	50	0	air
3	indurated sediment	15	0	air
5	sediment-filled basalt	50	0	air
10	dense basalt	5	0	air
100	segregated ice	95	100	ice
110	eolian sediment	50	100	ice
150	layered basalt	10	100	ice
152	fluvial sediment	20	100	ice
200	segregated ice	95	100	ice
220	crater ejecta	20	100	ice
250	layered basalt	10	100	ice
255	eolian sediment	50	100	ice
350	segregated ice	95	100	ice
355	volcanic ash	20	100	ice
900	segregated ice	95	100	ice
910	carbonate	5	100	ice
1000	layered basalt	10	100	ice

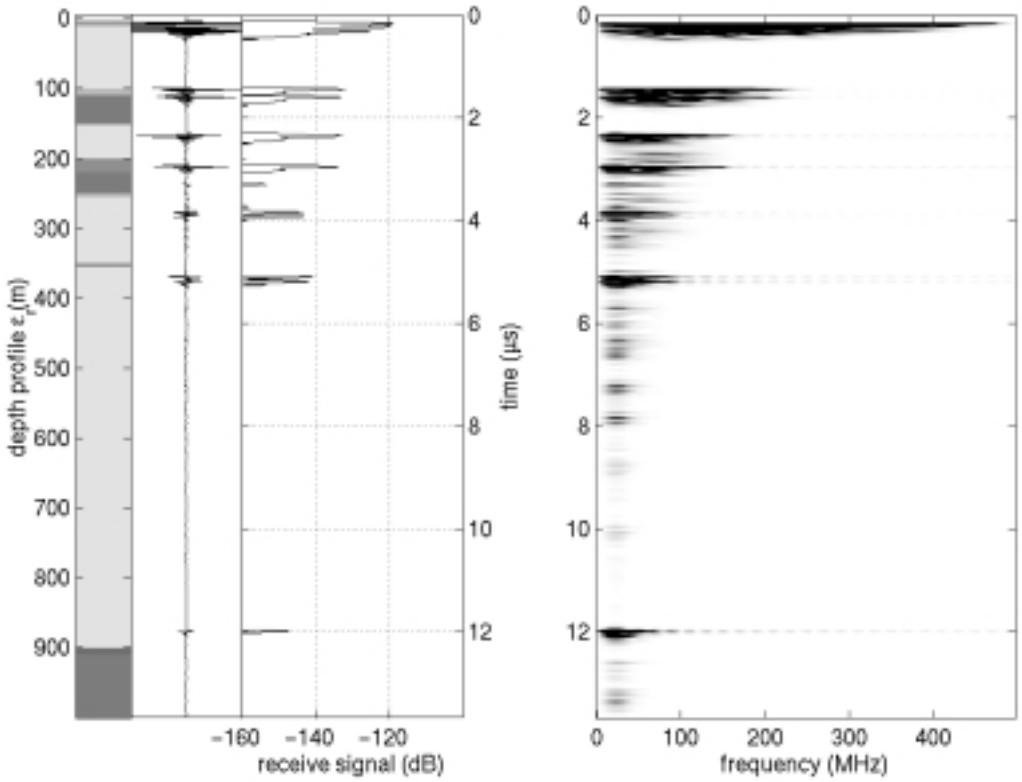

Figure B-3. Simulation Model: NS-3 Northern Plains Site.

Table B-4. Simulation Model: NS-4 Simple Massive Ice Lens

depth	lithology	ϕ%	s%	fill
400km	air	100	-	-
1	eolian sediment	50	0	air
3	indurated sediment	15	0	air
5	sediment-filled basalt	50	100	ice
50	layered basalt	10	100	ice
55	eolian sediment	50	100	ice
205	massive ice lens	100	100	ice
225	fluvial sediment	20	100	ice
1000	layered basalt	10	100	ice

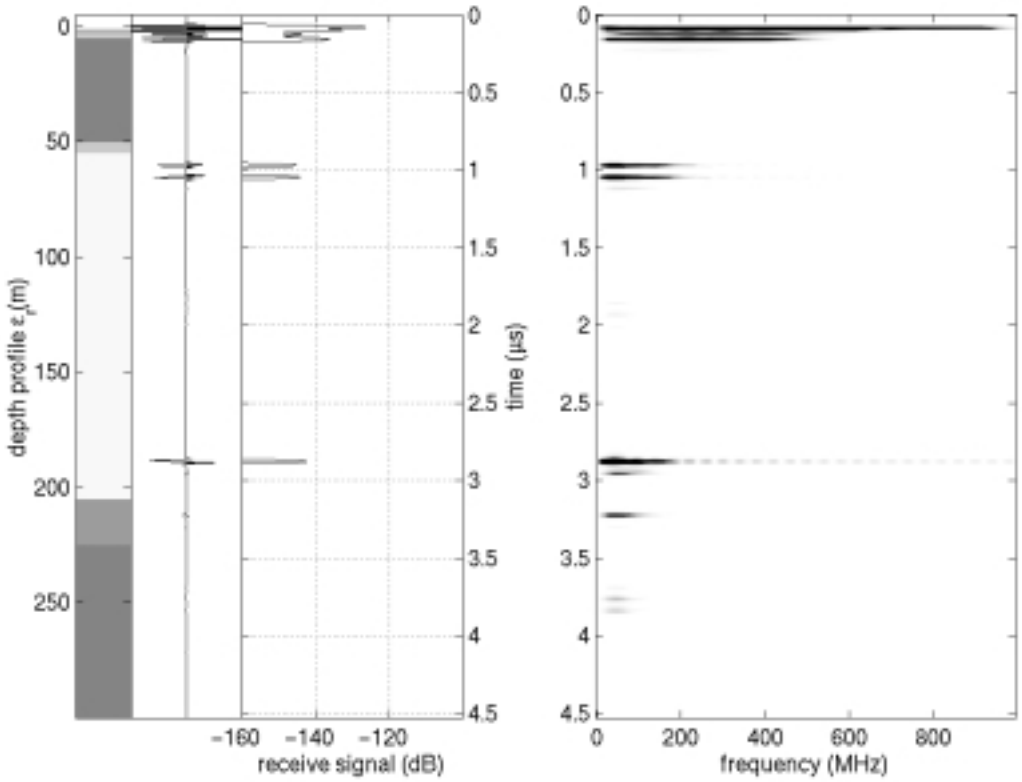

Figure B-4. Simulation Model: NS-4 Simple Massive Ice Lens.

Table B-5. Simulation Model: NS-5 Simple Near Surface Aquifer

depth	lithology	ϕ%	s%	fill
400km	air	100	-	-
1	eolian sediment	50	0	air
3	indurated sediment	15	0	air
5	sediment-filled basalt	50	100	ice
50	layered basalt	10	100	ice
55	eolian sediment	50	100	ice
205	layered basalt	10	100	water
225	fluvial sediment	20	100	water
1000	layered basalt	10	100	water

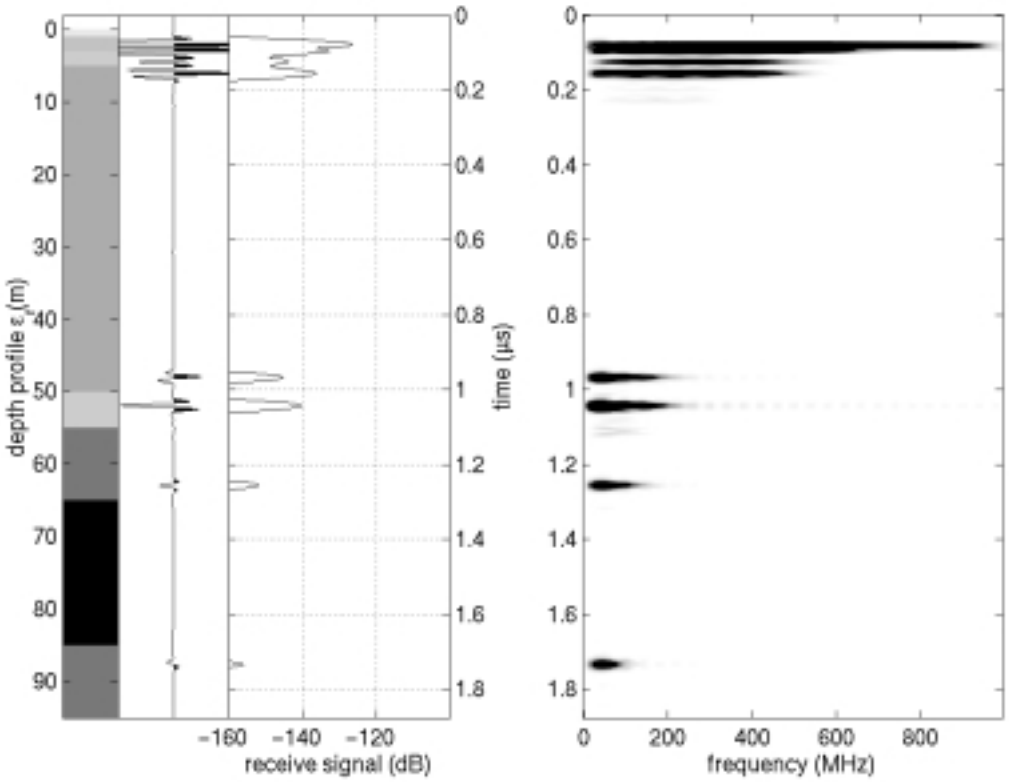

Figure B-5. Simulation Model: NS-5 Simple Near Surface Aquifer.

Table B-6. Simulation Model: NS-6 Simple Deep Aquifer

depth	lithology	ϕ%	s%	fill
400km	air	100	-	-
1	eolian sediment	50	0	air
3	indurated sediment	15	0	air
5	sediment-filled basalt	50	100	ice
50	layered basalt	10	100	ice
55	eolian sediment	50	100	ice
205	layered basalt	10	100	ice
225	fluvial sediment	20	100	ice
3000	layered basalt	10	100	ice
8000	layered basalt	10	100	water

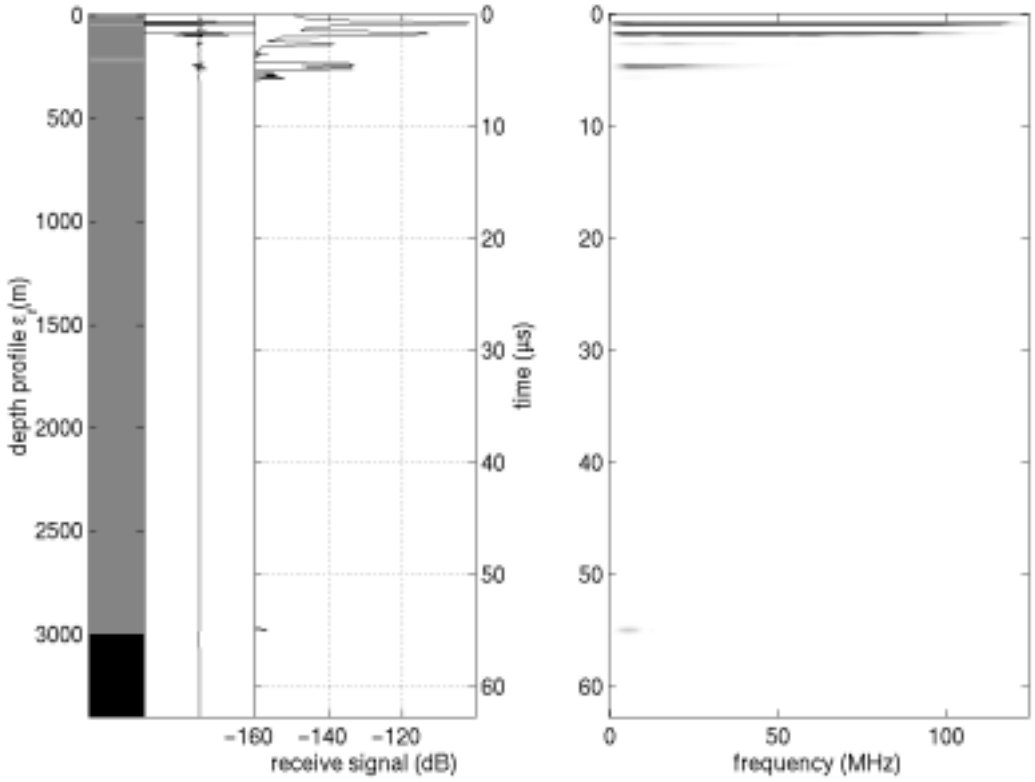

Figure B-6. Simulation Model: NS-6 Simple Deep Aquifer.

Table B-7. Simulation Model: DS-1 "Shallow " Global Aquifer

depth	lithology	ϕ%	s%	fill
400km	air	100	-	-
1000	layered basalt	10	100	ice
2500	layered basalt	10	100	ice
2550	fluvial sediment	20	100	ice
3000	layered basalt	10	100	ice
3600	layered basalt	10	90/10	ice/thin films
4000	layered basalt	10	100	water
4010	layered basalt	10	100	water
5000	layered basalt	10	100	water
6000	layered basalt	10	100	water
7000	layered basalt	10	100	water
8000	layered basalt	10	100	water

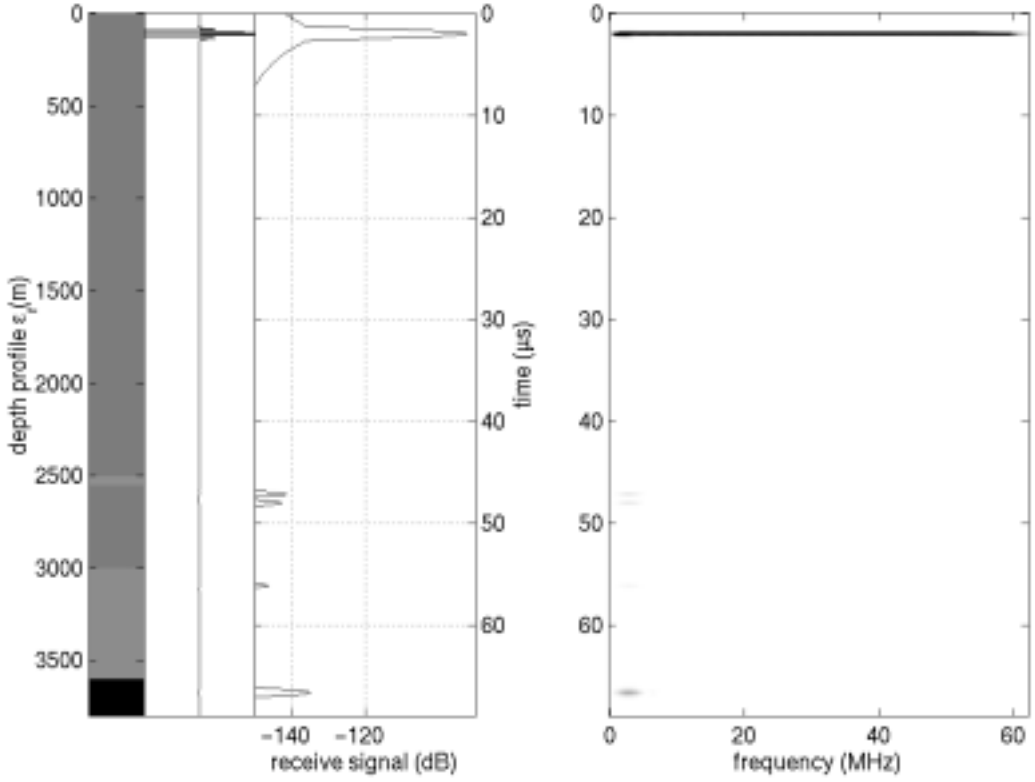

Figure B-7. Simulation Model: DS-1 "Shallow " Global Aquifer.

Table B-8. Simulation Model: DS-2 "Perched and Deep" Global Aquifer

depth	lithology	ϕ%	s%	fill
400km	air	100	-	-
1000	layered basalt	10	100	ice
2500	layered basalt	10	100	ice
2550	fluvial sediment	20	100	ice
3000	layered basalt	10	90/10	ice/thin films
3600	layered basalt	10	5	thin films
4000	layered basalt	10	5	thin films
4010	layered basalt	10	100	water
5000	layered basalt	10	5	thin films
6000	layered basalt	10	5	thin films
7000	layered basalt	10	5	thin films
8000	layered basalt	10	100	water

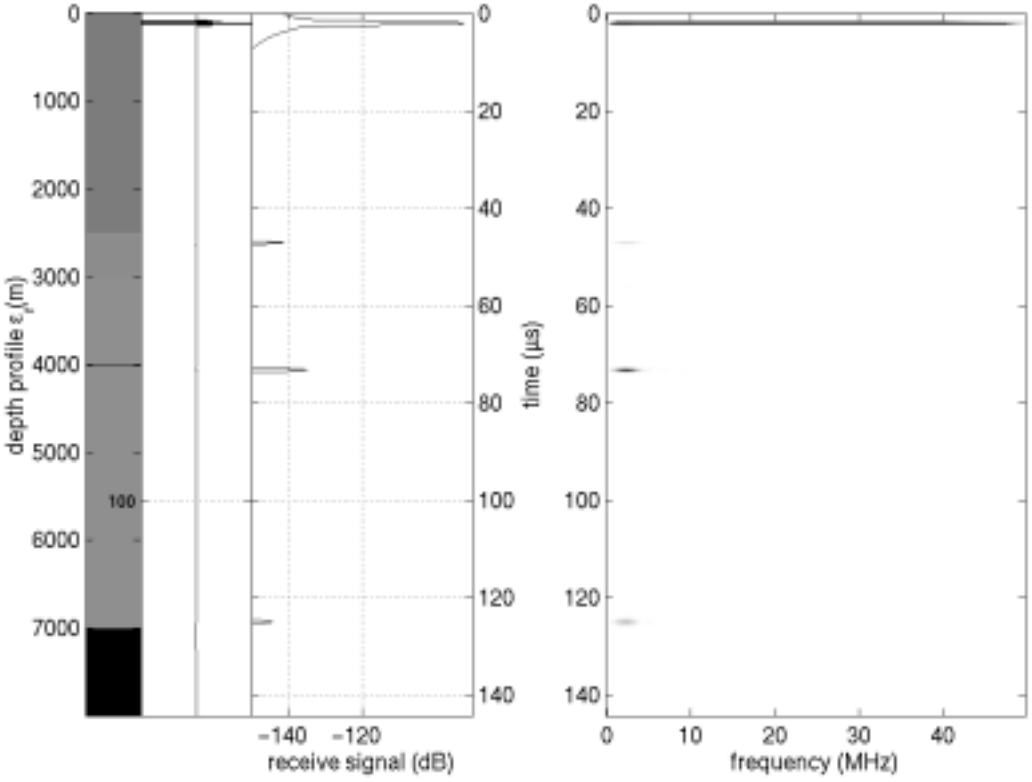

Figure B-8. Simulation Model: DS-2 "Perched and Deep" Global Aquifer.

Table B-9. Simulation Model: P-1 Polar Basil Melting

depth	lithology	ϕ%	s%	fill
400km	air	100	-	-
1000	layered ice & dust	90	100	ice
2500	layered ice & dust	80	100	ice
2501	fluvial sediment	80	100	ice
2550	layered ice & dust	70	100	ice
3000	layered ice & dust	60	100	ice
3600	layered ice & dust	50	100	ice
4000	layered basalt	10	100	water
4010	fluvial sediment	20	100	water
10000	layered basalt	10	100	water
15000	layered basalt	10	100	water

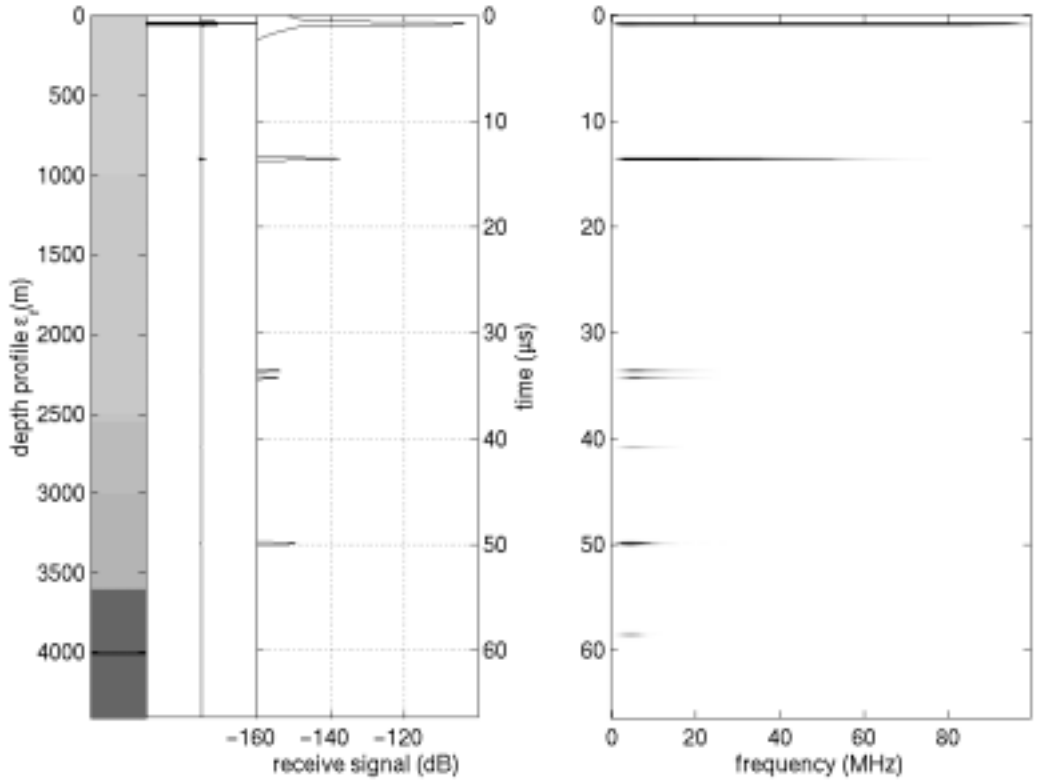

Figure B-9. Simulation Model: P-1 Polar Basil Melting.

Table B-10. Simulation Model: P-2 Deep Polar Aquifer

depth	lithology	ϕ%	s%	fill
400km	air	100	-	-
1000	layered ice & dust	90	100	ice
2500	layered ice & dust	80	100	ice
2501	fluvial sediment	80	100	ice
2550	layered ice & dust	70	100	ice
3000	layered ice & dust	60	100	ice
3600	layered ice & dust	50	100	ice
4000	layered basalt	10	100	ice
4010	fluvial sediment	20	100	ice
10000	layered basalt	10	100	ice
15000	layered basalt	10	100	water

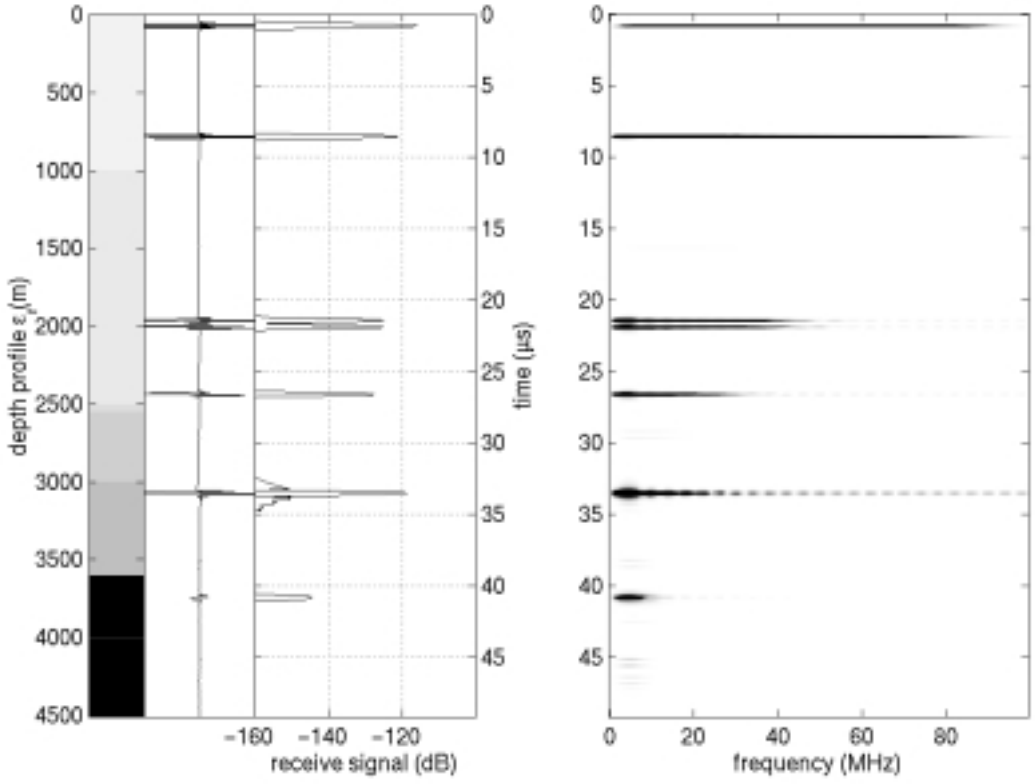

Figure B-10. Simulation Model: P-2 Deep Polar Aquifer.

APPENDIX C

PROPOSED RADAR SYSTEM

Chapter six suggested a proposed system based on the results obtain from both the simulations and also the experiments conducted in Alaska. The proposed system is a FM-CW radar operating from a few megahertz to a few hundred megahertz. For the prototype system, the 5 to 120 MHz operating frequency was constrained by the antennas at the lower frequency and the chirp synthesizer at the higher frequencies. At the cost of a bit more complexity to the transmitter, the system could be modified to operate up to a few hundreds of megahertz. The second recommendation for the proposed radar system is to separate the transmitter and receiver using a high-frequency wireless RF link. Letting the transmitter and receiver communicate using radio waves would allow them to be separated by a larger distance and conduct bistatic measurement. The main components of the proposed transmitter, receiver, and antenna subsystems are shown in Figure A3-1. The main difference in the modified block diagram is the addition of a digital transceiver in both the radar transmitter and receiver subsystems.

The receiver consists of a synthesize that is capable of generating the chirp signal for the transmit antenna. Depending on the frequency requirements, the synthesizer could be a single DDS with possibly some frequency multipliers or up-converters to increase the system bandwidth. An identical chirp signal and necessary timing signals, such as the clock and trigger, are input to a digital transceiver and sent over a wireless link to the transmitter. Ensuring that the wireless link does not experience any fading and does not interfere with the transmitted radar signal is important for both coherency and noise considerations. On the opposite side of the wireless link the receiver reproduces the timing signals and the replica of the transmitted chirp signal. The chirp is mixed with the receive signal and the resulting IF waveform is sent to the on-board data acquisition (DAQ) subsystem. With the necessary timing signals, the DAQ subsystem digitizes and integrates the IF signal. Finally, the digitized data are sent back across the wireless link to be stored on disk.

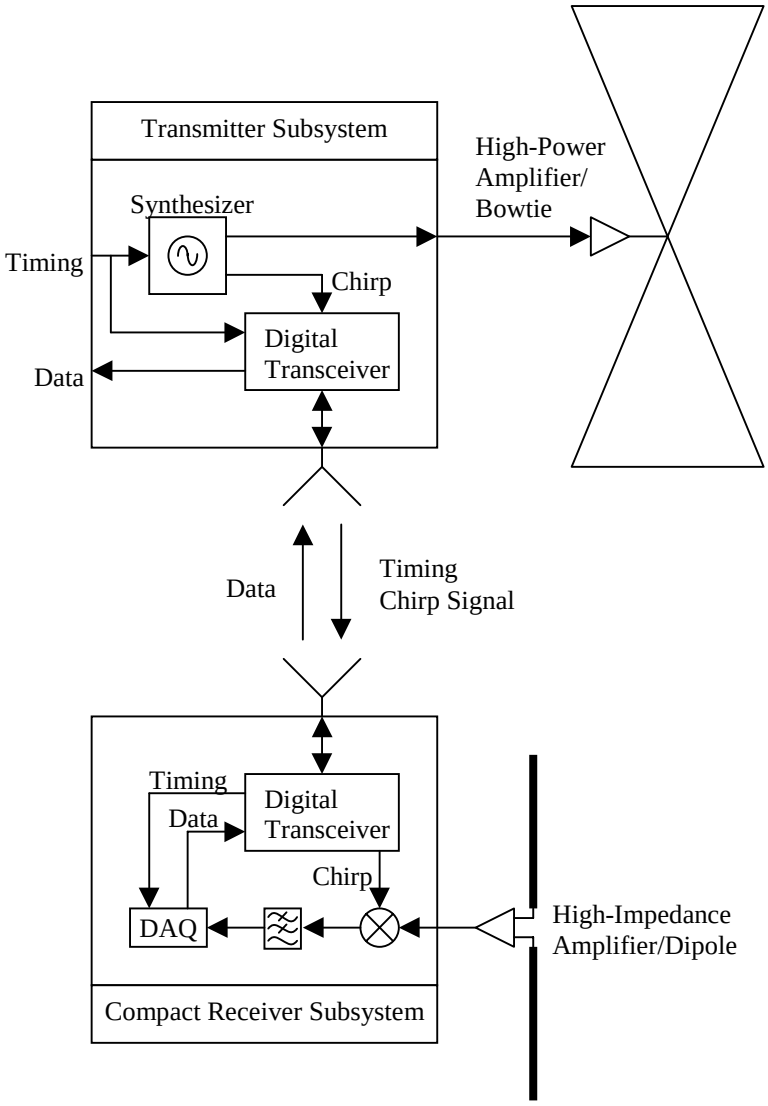

Figure C-1. Proposed Radar System.